

N O T I C E

THIS DOCUMENT HAS BEEN REPRODUCED FROM
MICROFICHE. ALTHOUGH IT IS RECOGNIZED THAT
CERTAIN PORTIONS ARE ILLEGIBLE, IT IS BEING RELEASED
IN THE INTEREST OF MAKING AVAILABLE AS MUCH
INFORMATION AS POSSIBLE

(NASA-TM-80735) SMMR SIMULATOR RADIATIVE
TRANSFER CALIBRATION MODEL. 2: ALGORITHM
DEVELOPMENT (NASA) 120 P HC A06/MF A01

CSCI 14B

N81-24498

Unclass

G3/43 25770



Technical Memorandum 80735

SMMR Simulator Radiative Transfer Calibration Model

II. Algorithm Development

S. Link, C. Calhoun and B. Krupp

DECEMBER 1980

National Aeronautics and
Space Administration

Goddard Space Flight Center
Greenbelt, Maryland 20771



SMMR SIMULATOR RADIATIVE TRANSFER CALIBRATION MODEL

II: ALGORITHM DEVELOPMENT

Susan Link

Charles D. Calhoon

Goddard Space Flight Center

Greenbelt, Maryland

Brian Krupp

Systems & Applied Sciences Corp.

Riverdale, Maryland

December 1980

GODDARD SPACE FLIGHT CENTER

Greenbelt, Maryland

SMMR SIMULATOR RADIATIVE TRANSFER CALIBRATION MODEL

II: ALGORITHM DEVELOPMENT

S. Link, C. D. Calhoon, and B. Krupp

Microwave Sensors Branch

ABSTRACT

Passive microwave measurements performed from earth orbit can be used to provide global data on a wide range of geophysical and meteorological phenomena. A Scanning Multichannel Microwave Radiometer (SMMR) is being flown on the Nimbus-G satellite. (A second SMMR was flown on the now inoperative Seasat-A satellite.) The SMMR Simulator duplicates the frequency bands utilized in the spacecraft instruments through an amalgamate of radiometer systems. Data taken using the SMMR simulator is being used by the scientific community for improving interpretation of the spacecraft data.

This document presents a calibration model developed for the SMMR Simulator Radiometer systems. The algorithm in this document utilizes data from the fall 1978 NASA CV-990 Nimbus-G underflight test series and subsequent laboratory testing.

Portions of the material for this document were compiled and revised from the reports given in the Reference list. NASA Technical Memorandum 80244 is included in its entirety.

PRECEDING PAGE BLANK NOT FILMED

CONTENTS

	<u>Page</u>
1.0 INTRODUCTION	1
1.1 General Background	1
1.2 Instrument Heritage	2
1.3 Scientific Background	4
1.3.1 Physics of Microwave Radiative Transfer	4
1.3.2 SMMR Parameters to be Measured-Frequency Selection	16
2.0 SMMR SIMULATOR RADIOMETER SYSTEMS DESCRIPTION	19
2.1 Basic Radiometer Operation	19
2.2 Subsystem Description	20
2.2.1 Antenna and Radome	20
2.2.2 Electronics Package	20
2.2.2.1 Switching and Calibration Network	20
2.2.2.1.1 Switching Block	23
2.2.2.1.2 Liquid Nitron Load	23
2.2.2.2 Receiver Electronics	23
2.2.2.3 Post Detection Processor	23
2.2.3 Power System	23
2.2.4 Timing and Control System	23
2.2.5 Data Buffer and Distribution System	23
2.3 CV-990 Aircraft Installation	24
2.3.1 Basic Capabilities of the CV-990	24
2.3.2 SMMR Simulator CV-990 Installation	26
3.0 BASIC RADIOMETRIC EQUATION-DERIVATION	27
4.0 SMMR SIMULATOR SYSTEM LOSSES-RADIATIVE TRANSFER ANALYSIS	35

CONTENTS (Continued)

	<u>Page</u>
4.1 Radiative Transfer Theory	35
4.1.1 Radiative Transfer Theory Applied to a Cascade of Lossy Elements	35
4.1.2 Application to Cascade of Ferrite Circulator Junctions	37
4.2 Losses External to the Switch Block	42
4.2.1 6.6 and 10.7GHz Radiometers	43
4.2.2 18GHz Radiometer	44
4.2.3 21GHz Radiometer	45
4.2.4 21GHz Uplook Radiometer	45
4.2.5 37GHz Radiometer	46
4.3 Losses Internal to the Switch Block	47
4.3.1 Switch Block 6.6, 10.7, 21, Uplook	48
4.3.2 Switch Block 18 and 37GHz	49
4.4 SMMR Simulator Radiometer Equations	51
4.4.1 Derivation Method	51
4.4.2 Radiometric Equations	52
4.4.2.1 6.6 and 10.7GHz Radiometers	52
4.4.2.2 18GHz Radiometer	53
4.4.2.3 21GHz Radiometer	54
4.4.2.4 21GHz Uplook Radiometer	55
4.4.2.5 37GHz Radiometer	56
4.4.3 Radiometer Equations—SMMR Simulator—General Form	58
5.0 SMMR SIMULATOR ALGORITHM DEVELOPMENT	59
5.1 Development Technique	59
5.2 SMMR Simulator System Algorithms	62
5.2.1 10.7GHz Radiometer System	63

CONTENTS (Continued)

	<u>Page</u>
5.2.2 21GHz Radiometer System	64
5.2.3 21GHz Uplooking Radiometer System	64
5.2.4 37GHz and 37GHz Uplook Radiometer Systems	65
5.3 SMMR Simulator Algorithm Coefficient Values	66
6.0 EFFECTS OF COMPONENT MISMATCH ON THE OPERATION CHARACTERISTICS OF A RADIOMETER SYSTEM	67
6.1 First Order VSWR Effects	67
6.2 Second Order VSWR Effects	69
7.0 SMMR SIMULATOR CALIBRATION TESTING	75
7.1 Component Physical Temperature Monitoring	75
7.2 Component Calibration Tests	76
7.2.1 Component Level ("Piece Part") Testing	76
7.2.1.1 Waveguide, Antenna, Radome Transmissivities	76
7.2.1.2 Ferrite Switch Block Leakage Ratios	77
7.2.2 System Level Testing	81
7.2.2.1 Ground ("Hangar") Tests	81
7.2.2.2 Airborne	83
8.0 ALGORITHM COEFFICIENT DETERMINATIONS	83
8.1 Determination Technique	83
8.1.1 Determination of α_R	84
8.1.2 Leakage Coefficients Determination (\mathcal{L}_{mn})	85
8.1.3 External Loss Coefficients	85
8.1.4 "Fine Tuning" the Coefficient Determination(s)	90
8.2 System Coefficient Determination	92
8.2.1 10.7GHz Radiometer System	92

CONTENTS (Continued)

	<u>Page</u>
8.2.2 21GHz Radiometer System	92
8.2.3 21GHz Uplook Radiometer System	93
8.2.4 27GHz and 37GHz Uplook Radiometer System	93
8.3 Algorithm Coefficients Summary	94
9.0 ALGORITHM VERIFICATION	96
9.1 Calibration Data Anomalies	96
9.1.1 Cold Calibration Target	96
9.1.2 Ambient Calibration Target	97
9.1.3 Component Level ("Piece Part") Testing VSWR Effects	97
9.1.4 Waveguide Heater, 21GHz Vertical Channel	98
9.2 Algorithm Verification	98
10.0 REFERENCES	105

LIST OF ILLUSTRATIONS

<u>Figure</u>	<u>Page</u>
1-1 The Effect on Microwave Radiation at an Angle, θ , on an Absorbing Slab of Uniform Temperature Absorptivity and Thickness	7
1-2 Microwave Attenuation Due to Atmospheric Water Vapor	7
1-3 Microwave Attenuation Due to Liquid Water (Approximate)	8
1-4 Microwave Absorption By Atmospheric Oxygen	8
1-5 Typical Microwave Earth-Viewing Geometry	9
1-6 Dielectric Constant of Water $k = (k' + ik'')$ at 20°C	10
1-7 Emissivity of Water at 20°C	11
1-8 Radiometric Temperature Sensitivity for Calm Seawater, Vertically Polarized Component	12
1-9 Dependence of Brightness Temperature on Sea State	14

LIST OF ILLUSTRATIONS (Continued)

<u>Figure</u>		<u>Page</u>
1-10	Brightness Temperature Results of Bare Fields with Clay Loam Soils, 1.55cm Radiometer, Phoenix, Arizona	15
1-11	Microwave Emissivity Contrasts of Old and New Ice	17
2-1	Radiometer System Block Diagram	21
2-2	Switching and Calibration Network	22
2-3	Cabin Installation	28
2-4	Aft Cargo Installation	28
2-5	Microwave Antenna Housing	29
2-6	Radome Closures	29
2-7	Window Mount Antennas	30
2-8	Antenna Installations	30
2-9	6.6GHz Antenna (Vertical Polarization)	31
2-10	6.6GHz Radome	31
2-11	Waveguide Feedthroughs	32
2-12	10.7 and 18GHz Waveguide Runs-Aft Cargo	33
2-13	6.6GHz Feedthrough Installed	33
4-1	Radiative Transfer Across a Plane-Parallel Slab	35
4-2	Radiative Transfer Across Two Plane-Parallel Slabs	36
4-3	Radiative Transfer Across Three Plane-Parallel Slabs	36
4-4	Typical Ferrite Junction-Circulator	37
4-5	Schematic Representation-Two Junction Ferrite Switch Configuration- Case 1	39
4-6	Schematic Representation-Two Junction Ferrite Switch Configuration- Case 2	40
4-7	Schematic Representation-Two Junction Ferrite Switch Configuration- Case 3	40

LIST OF ILLUSTRATIONS (Continued)

<u>Figure</u>		<u>Page</u>
4-8	Schematic Representation-Two Junction Ferrite Switch Configuration- Case 4	41
4-9	Schematic Representation-External Losses for 6.6 and 10.7GHz Radiometer	43
4-10	Schematic Representation-External Losses for 18GHz Radiometer	44
4-11	Schematic Representation-External Losses for 21GHz Radiometer	45
4-12	Schematic Representation-External Losses for 21GHz Uplook Radiometer	45
4-13	Schematic Representation-External Losses for 37GHz Radiometer	46
4-14	Schematic Representation Switch Block 6.6, 10.7, 21, and 21GHz Uplook	48
4-15	Schematic Representation Switch Block for 18 and 37GHz	49
5-1	Schematic Representation-Typical SMMR Simulator Radiometer	59
5-2	Schematic Representation-10.7GHz Radiometer	63
5-3	Schematic Representation-21GHz Radiometer	64
5-4	Schematic Representation-21GHz Uplooking Radiometer	64
5-5	Schematic Representation-37GHz Radiometer	65
6-1	Typical Radiometer System	70
6-2	Typical Ferrite Junction Circulator	71
7-1	Schematic Representation-SMMR Simulator Ferrite Switch Blocks	79
8-1	α_R : 10.7GHz Radiometer (Piece Part Warm Up)	86
8-2	α_R : 21GHz Radiometers (Piece Part Warm Up)	87
8-3	α_R : 37GHz Radiometer (Piece Part Warm Up)	87
8-4	α_{RV} : 37GHz Vertical Polarization	88
8-5	Iterative Coefficient Determination-37GHz Vertical	91
9-1	Systems Data Consistency Check	99

LIST OF TABLES

<u>Table</u>		<u>Page</u>
1-1	Parameters to be Determined by SMMR	5
2-1	Radiometer Subsystem Installation Locations CV-990	27
4-1	Radiometer Subsystem Installation Locations CV-990	42
4-2	External Component Identification	43
5-1	External Component Coefficient Values	66
5-2	Leakage Ratio x 100	67
6-1	Ferrite Junction VSWR - Isolation (Approximate)	72
6-2	VSWR - Coefficient of Reflectivity	74
7-1	Component Physical Temperature Monitoring	75
7-2	Waveguide Transmissivities	78
7-3	Antenna Transmissivities	78
7-4	Antenna/Waveguide System VSWR	78
7-5	Ferrite Switch Block Transmissivities	80
7-6	Ferrite Leakage Ratio x 100	81
8-1	Coefficient Determination Test	92
8-2	System Transmissivity - Piece Part vs. Calculated	94
8-3	Leakage Ratio x 100	95
8-4	External Loss Coefficients	95
9-1	Calculated Brightness Temperatures - 45° Bank Turns	100
9-2	Calculated Brightness Temperatures - 21GHz Uplook - High Altitude	101
9-3	Calculated Brightness Temperatures - 37GHz Uplook - High Altitude	102
9-4	Calculated Brightness Temperatures - 10.7GHz - Wingover	102
9-5	Calculated Brightness Temperatures - 21GHz - Wingover	103
9-6	Calculated Brightness Temperatures - 37GHz - Wingover	104

SMMR SIMULATOR RADIATIVE TRANSFER CALIBRATION MODEL

II: ALGORITHM DEVELOPMENT

1.0 INTRODUCTION

1.1 General Background

The SMMR Simulator is an aircraft instrument which has been built to simulate the physics of the scanning multichannel microwave radiometer (SMMR) flown on the Nimbus-7 and Seasat satellites. This is an earth oriented microwave radiometer system which measures important oceanographic and meteorological characteristics needed to increase man's understanding of the ocean/atmosphere interface and its influence on world weather and climate.

The instrument provides data for the measurement of the ocean energy transfer parameters such as sea surface temperature, sea surface roughness (including foam, from which sea surface winds can be inferred), precipitation, and the sea/air heat exchange. Another objective is the mapping of polar ice coverages and the determination of the local age of the ice canopy.

The SMMR can also provide large scale data on land surfaces. Typical land surface data would include average soil moisture, extent of snowpack cover, and an indication of melting of snow on land areas having sufficient homogeneity (e.g., Great Plains of the United States).

The water present in the atmosphere, whether it is in the form of vapor, non-raining cloud water droplets, or rain, will affect the measured surface radiometric temperatures. These quantities must also be measured, therefore, in order that corrections to the surface data can be made.

The SMMR simulator duplicates the frequency bands utilized on the spacecraft instrument through an amalgamate of radiometer systems. These systems operate at center frequencies of 6.6, 10.7, 18.0, 21.0, and 37 GHz. Each system operates in a receiver "time-share" mode such that readings are taken of both the vertically and horizontally polarized components of the received power. The antennas, mounted so as to provide a 45° view angle from nadir, all have 6° beam-widths making the system incident field-of-view approximately 1/10 of the aircraft altitude.

The SMMR simulator was flown on the NASA CV-990 during 1976, 1977 and 1978. Aircraft observations made with the SMMR simulator are useful in algorithm development, cross-calibration of the satellite data via underflight observations, high-resolution studies of the sea surface, and determinations of atmospheric water vapor and liquid water profiles.

The raw data obtained in a SMMR simulator observation are in the form of radiometer output voltages. These data must be calibrated before they can be analyzed in terms of the physical process producing the emission; that is, the radiometer output voltage must be related quantitatively to the intensity of the microwave radiation incident on the SMMR collection system.

This study is concerned with the development of an algorithm for calibration of the SMMR simulator.

This study derives the "exact" calibration equation by applying microwave radiative transfer theory to the SMMR simulator collection system. The system calibration algorithm is developed from this calibration equation using physically measureable parameters. For purposes of system calibration, it is assumed the power received by the radiometer system at the radome interface represents the absolute or true temperature of the scene being viewed. Any atmospheric phenomena or cross coupling aberrations are treated as part of the true temperature.

1.2 Instrument Heritage

Passive microwave measurements performed from earth orbit can be used to provide global data on a wide range of geophysical and meteorological phenomena. The use of such measurement techniques for remotely sensing earth's atmosphere and surface has been reviewed by Staelin and by Tomiyasu.^{1, 2}

The use of passive microwave imagers for remote sensing of earth surface parameters was started in earnest in 1967 with the installation of the electrically scanned microwave radiometer (ESMR) on-board the NASA CV-990 airborne laboratory.

The ESMR was used to study a variety of phenomena involving the surface of the earth and its atmosphere.³⁻¹⁰ This imaging radiometer operates at a wavelength of 1.55 cm. It became

evident that the ESMR could be used to infer the extent, the concentration, and the age of sea ice; the extent, concentration and thickness of lake ice; rainfall rates over oceans; surface wind speeds over open water; particle size distribution in the deep snow cover of continental ice sheets; and soil moisture content in unvegetated fields.

The first experiments to use microwave techniques from earth orbit for remote sensing of geophysical phenomena were performed from the Soviet COSMOS-253 and COSMOS-384 satellite in 1968 and 1970, respectively.^{11,12} The COSMOS experiments performed measurements at wavelengths of 8.5, 3.4, 1.35 and 0.8 cm for observing surface features such as ice in polar regions, and for observing atmospheric water vapor and liquid water over oceanic areas.

An ESMR has been operational, also at a wavelength of 1.55 cm, on the Nimbus-5 satellite since its launch in December 1972 and has been obtaining information on rainfall rates and sea ice cover on a global basis since that time.¹³

The other microwave experiment on Nimbus-5, the Nimbus-E Microwave Spectrometer (NEMS) performed nadir observations with five channels operating at wavelengths between 1.35 and 0.5 cm to obtain measurements, principally, of the atmospheric temperature profile, and of atmospheric water vapor and liquid water over oceanic areas.¹⁴

Several additional microwave experiments from earth orbit have been performed by the United States since Nimbus-5. The Skylab missions in 1973 and 1974 carried a radiometer operating at 21 cm wavelength.¹⁵ Nimbus-6 launched in June 1975, carries an Electrically Scanned Microwave Radiometer (ESMR) operating at 0.8 cm wavelength, which is more sensitive to atmospheric water than the Nimbus-5 ESMR and scans the earth in a conical manner, keeping the angle of incidence of the observation constant to ease interpretation.¹⁶ Nimbus-6 also carried a Scanning Microwave Spectrometer (SCAMS) which is similar to the Nimbus-5 NEMS, but has a scanning antenna for producing images.¹⁷

The radiation received by the ESMR imaging radiometers on-board a satellite is a combination of the contributions from both the atmosphere and the surface of the earth. In general it is not possible to separate these phenomena with the information in a single radiometer channel, thus requiring multi-spectral imaging techniques to unscramble the combined contributions of the atmosphere and the surface. An early effort in this direction has been accomplished on Nimbus 5 & 6 using NEMS and SCAMS.

A scanning multichannel microwave radiometer (SMMR) is being flown on the Nimbus-7 and Seasat satellites.¹⁸ This is a ten-channel instrument in which the wavelengths to be observed are 0.8, 1.4, 1.7, 2.8, and 4.5 cm, and with both polarizations to be observed at each wavelength.

A summary of the properties of the surface of the earth and its atmosphere thought to be extractable from SMMR data are listed in Table 1-1.

The advent of the Space Transportation System (Space Shuttle) in 1980 will make feasible a new generation of microwave earth observations experiments. The increased volume and weight payload accommodations of the Shuttle will allow larger antenna structures to be used for earth observations experiments than previously possible. These larger antenna structures will provide substantially improved spatial resolution at wavelengths which have been used on prior experiments, and will make feasible the use of longer wavelengths not previously used for earth observations. Because of advancement in microwave radiometer technology at the shorter wavelengths, it will also be feasible to use shorter wavelengths for observation than previously possible.

1.3 Scientific Background

1.3.1 Physics of Microwave Radiative Transfer

At microwave frequencies (1-500GHz) and at temperatures typical of the earth and its atmosphere (200-300°K), the Rayleigh Jeans approximation for the intensity of thermal radiation from a blackbody is valid, thus the equation of radiative transfer for an isotropic, nonscattering medium can be written as

$$dT_B(\theta, \phi) = \gamma [T(X) - T_B(\theta, \phi)]$$

Table 1-1
Parameters to be Determined by SMMR

Parameter	Discipline/User Area	Remarks
Surface Winds (Ocean) Foam Cover Capillary Waves Large Scale Roughness	Oceanography, Meteorology Shipping	First System to Monitor Surface Winds Remotely.
Precipitation Rain Rate Rain/Snow Line	Meteorology, Shipping	Hurricane Classification Looks Promising
Water Vapor	Meteorology	Air Mass Discrimination Initial State Parameter for Forecast Models
Sea Ice Coverage Age Dynamics	Polar Studies, Meteorology, Military, Oceanography	Currently Operational Need for Continuity.
Soil Moisture	Meteorology, Hydrology, Military	Sampling Depth CA. 1/15 of a Wavelength.
Snow Cover (Over Land) Extent Ripeness	Meteorology, Hydrology	Strong Day/Night Differences Due to Varying Liquid Water Content
Cloud Physics Liquid Water Content Drop Size Parameters	Meteorology	Forecasting

where $T_B(\theta, \phi)$ is the radiance in the direction (θ, ϕ) expressed as equivalent blackbody temperature, $T(X)$ is the thermodynamic temperature of the absorbing medium and γ is the absorption coefficient in units of X^{-1} . The derivative on the left side is along a ray path. The physical meaning of this equation can be understood by examining the effect on microwave radiation incident at an angle θ , on an absorbing slab of uniform temperature T_0 , absorptivity γ_0 , and of thickness δ as shown in Figure 1-1. The radiation from the other side consists of the incident radiation as attenuated by the slab $T_B e^{-\gamma_0 \delta \sec \theta}$ plus re-radiation component $(1 - T_B e^{-\gamma_0 \delta \sec \theta}) T_0$. If the slab is opaque ($\gamma_0 \delta \sec \theta = \infty$), the radiation emerging is characterized by the thermodynamic temperature of the slab independent of the intensity of the incident radiation.

There are three major contributions to γ in the atmosphere: water vapor, liquid water, and molecular oxygen. Figures 1-2, 1-3, and 1-4 show the approximate magnitude of each of these contributions. Detailed discussions of each of these can be found in Gunn and East (1954),²¹ Meeks and Lilley (1963),²² and Staelin (1966).²³ Figure 1-5 shows the typical microwave earth viewing geometry. The observed brightness temperature is

$$T_B = \int_0^H T(h) \frac{dt(h)}{dh} dh + t(H) [\epsilon T_0 + (1 - \epsilon) T_S],$$

$$\text{where } t(h) = e^{-\int_0^h \gamma(x) \sec \theta dx},$$

$T(h)$ is the atmospheric temperature profile, H is the altitude of the observation, ϵ is the emissivity of the surface, T_0 is the thermodynamic temperature of the surface, and T_S is the reflected sky brightness. At frequencies of about 50 GHz the variations in ϵ dominate the variations in T_B over the earth's surface. The major contribution to variations in ϵ is liquid water with its extremely large dielectric constant at microwave frequencies. Figure 1-6 shows the real part k' and the k'' of the dielectric constant of both fresh and sea water at 20°C as calculated from the data of Lane and Saxton (1952).²⁴ Conductivity data from the International Critical Tables (1928)²⁵ are included as k in Figure 1-6.

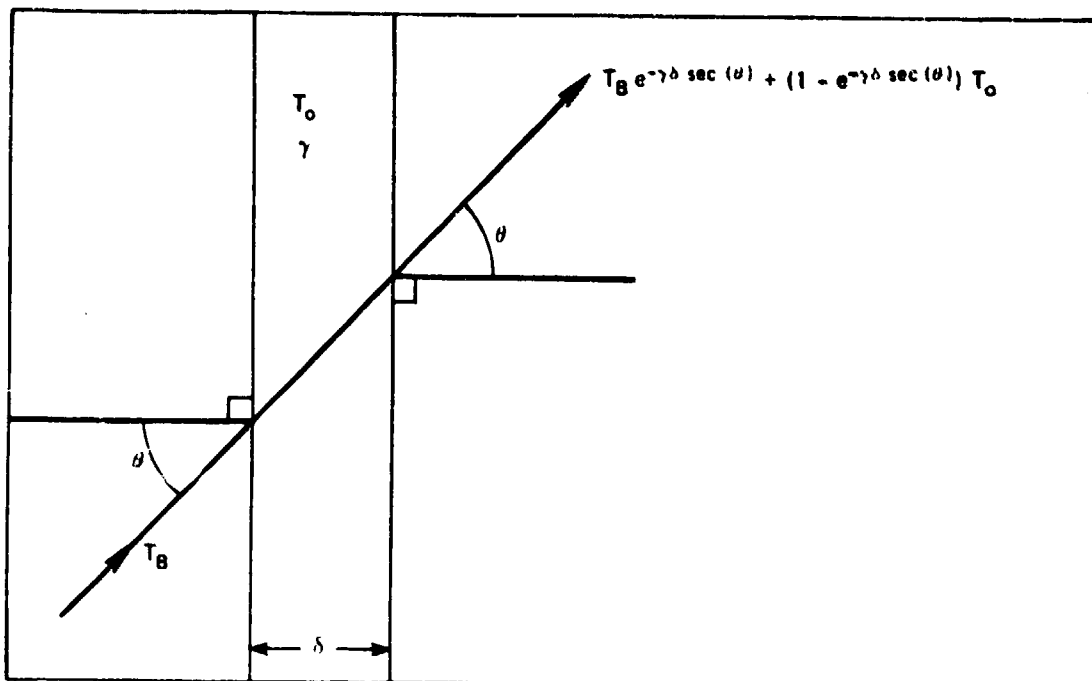


Figure 1-1. The Effect on Microwave Radiation at an Angle, θ , on an Absorbing Slab of Uniform Temperature Absorptivity and Thickness

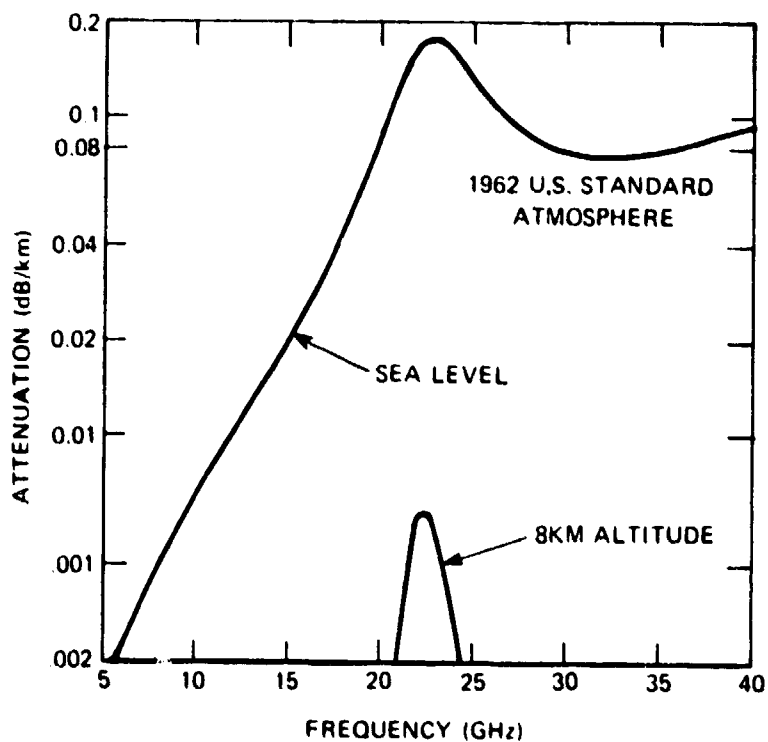


Figure 1-2. Microwave Attenuation Due to Atmospheric Water Vapor

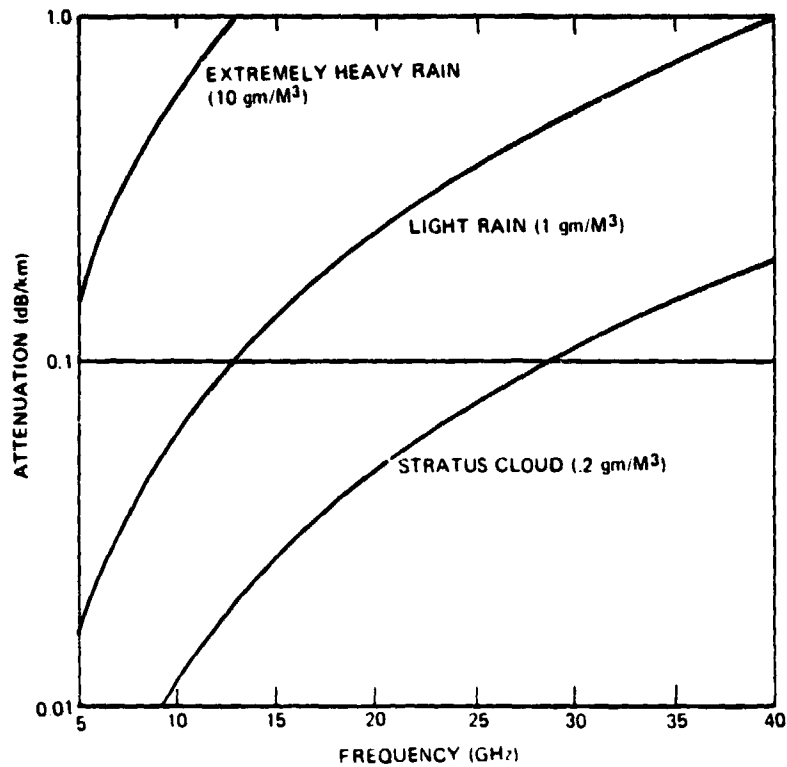


Figure 1-3. Microwave Attenuation Due to Liquid Water (Approximate)

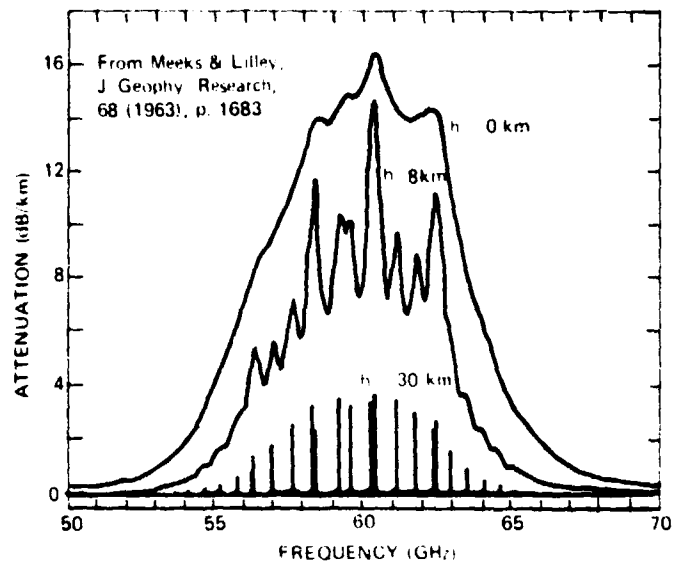


Figure 1-4. Microwave Absorption by Atmospheric Oxygen

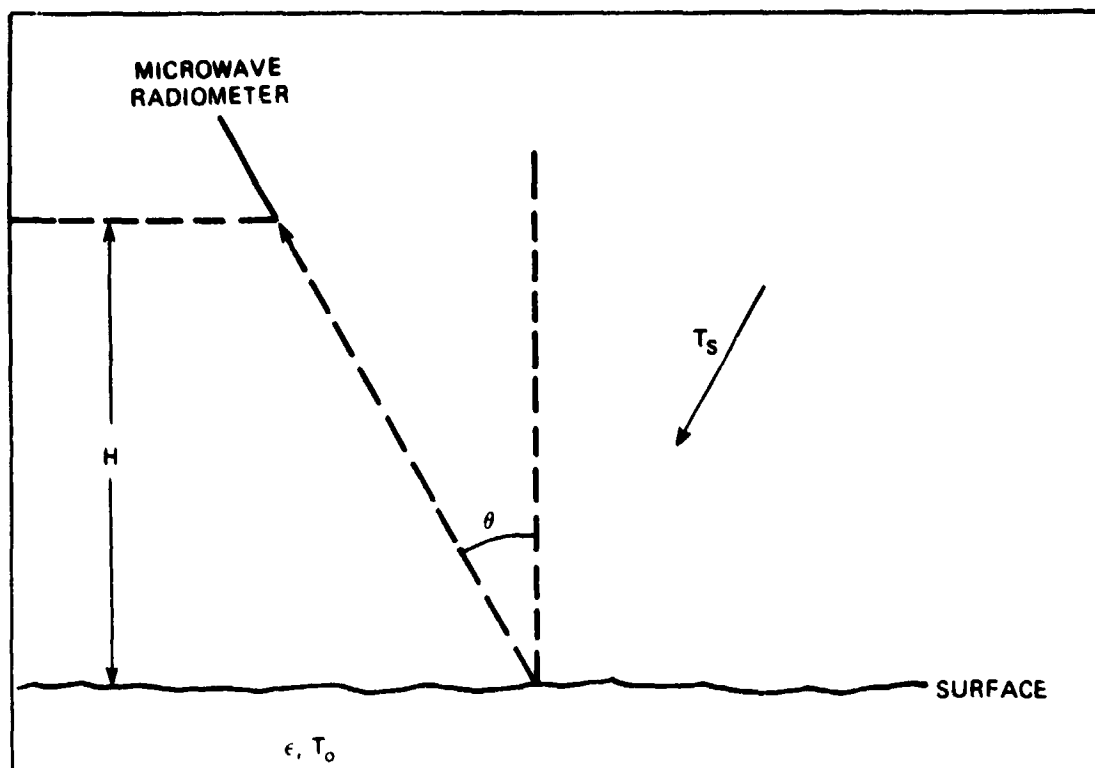


Figure 1-5. Typical Microwave Earth-Viewing Geometry

The emissivity can be calculated for smooth water for any angle and polarization from electromagnetic theory (Jackson 1962).²⁶ Figure 1-7 shows the emissivity as a function of frequency at 20°C for sea and fresh water for viewing at nadir, and at 45° for vertical and horizontal polarization. The dependence of the primary ϵT_0 term on the surface temperature is given in Figure 1-8 for nadir viewing (incidence angle = 0°) and for a 55° incidence angle for vertical polarization. The sensitivity to surface temperature is small, particularly near 1-1.5 cm wavelength. The maximum sensitivity to surface temperature occurs near a wavelength of 5 cm.

The emissivity of the surface also depends on surface wind because of the generation of roughness and foam. The roughness effect has been investigated by Hollinger (1971)²² and others. There is little roughness effect for viewing near nadir and near 55° with vertical polarization. The effect is maximized by viewing the surface obliquely with horizontal polarizations. At a 55° incidence angle the effect is about 1°K increase in brightness temperature for each meter per second

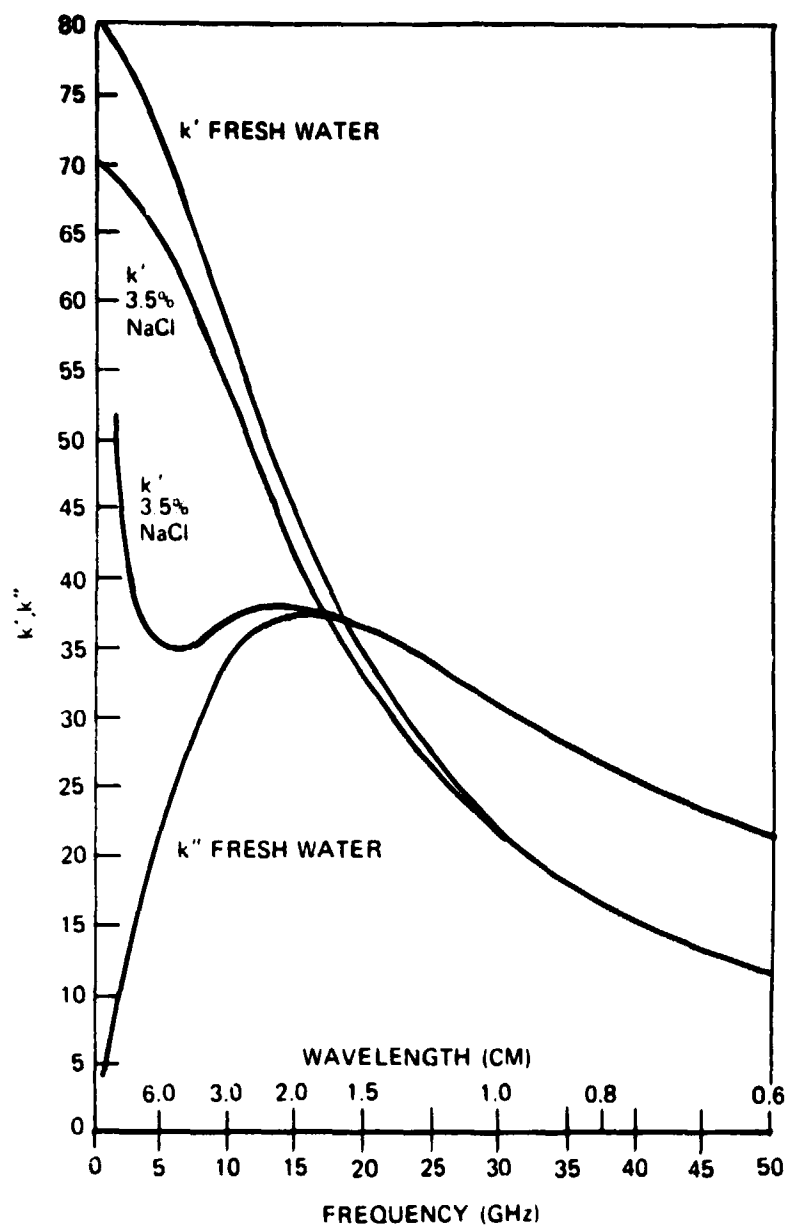


Figure 1-6. Dielectric Constant of Water
 $k = (k' + ik'')$ at 20°C

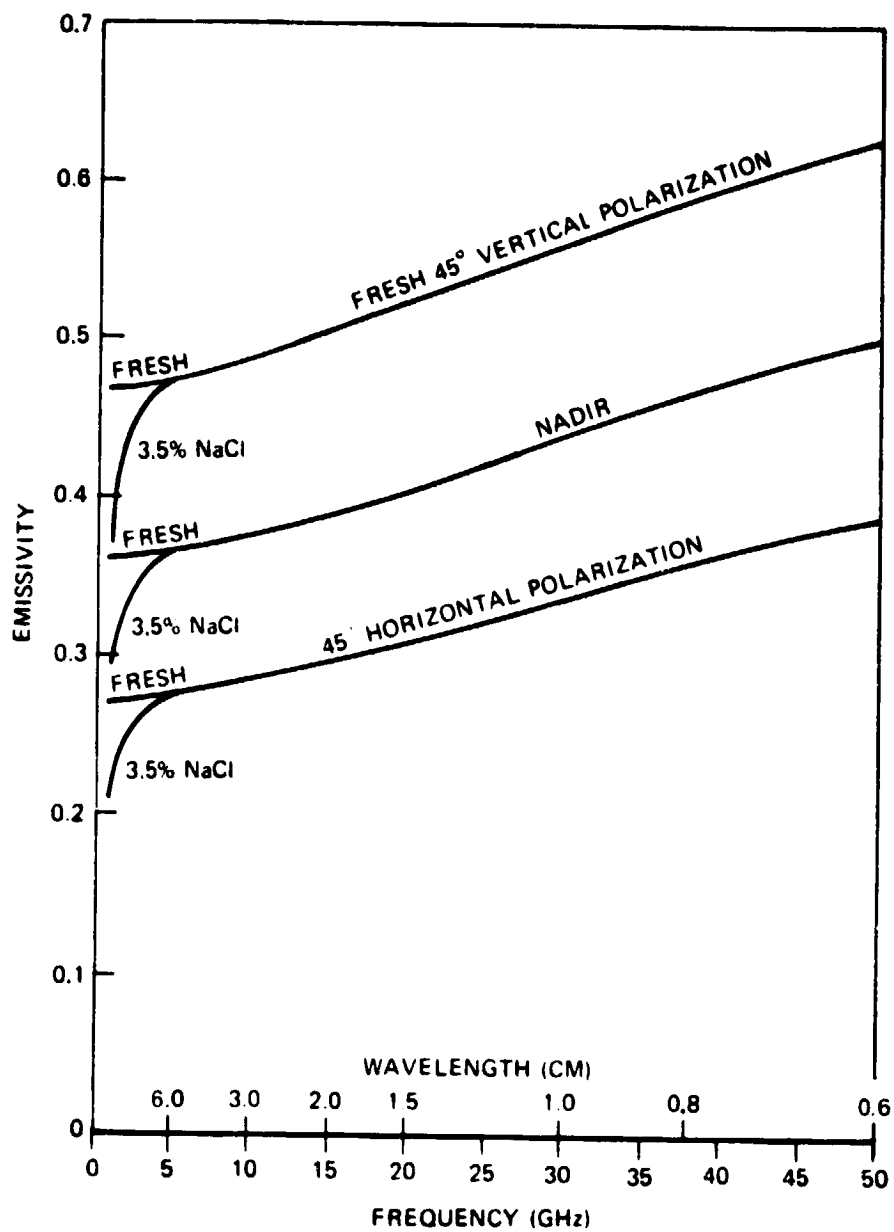


Figure 1-7. Emissivity of Water at 20°C

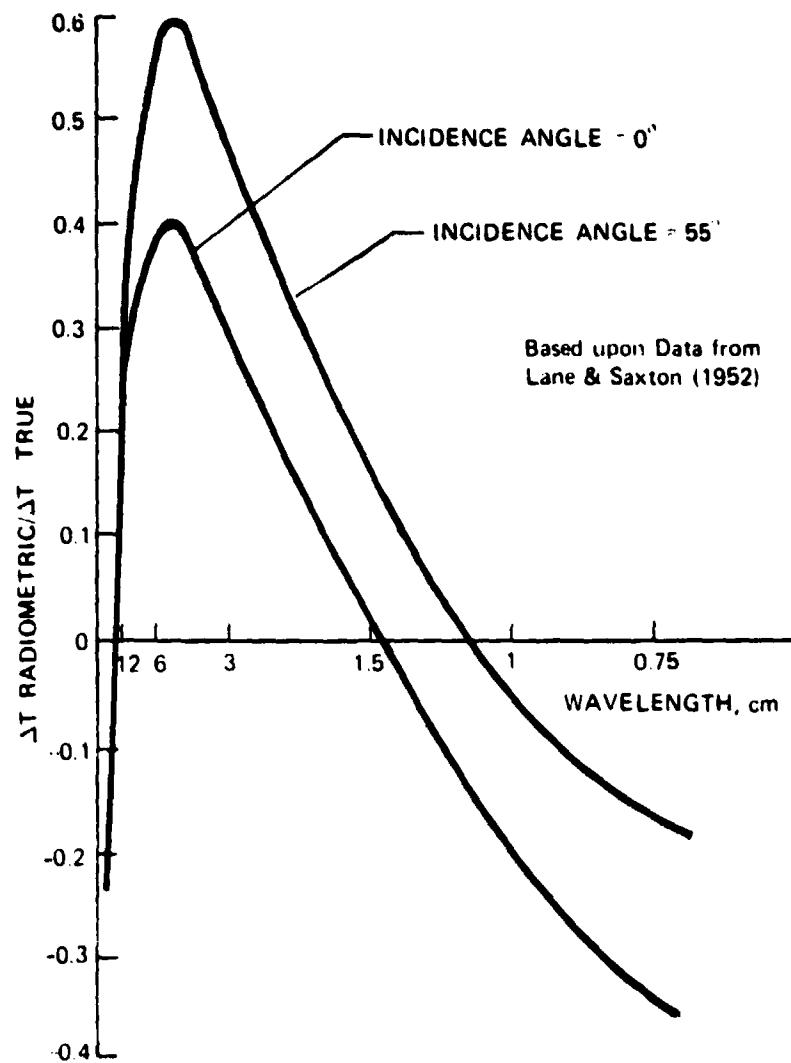


Figure 1-8. Radiometric Temperature Sensitivity for Calm Seawater, Vertically Polarized Component

increase in wind speed. Foam, which has been investigated by Nordberg, et al., (1971)²⁸ and Von Melle, et al., (1973) has an emissivity near 0.8. The foam coverage increases roughly 2% for each meter per second increase in wind speed about 7 m/s. Neither effect shows strong frequency dependence through the microwave range. The effect of surface wind is summarized in Figure 1-9.

The emissivity of a land surface is typically greater than 0.9 so the brightness temperature contrast between land and water is greater than 100°K; therefore, the outlines of the continents will be quite visible in the SMMR data. This will provide a convenient geographic reference but little scientific value. However, in areas with little vegetation, the moisture content of the soil affects the microwave signature markedly. Figure 1-10 (from Reference 29) shows data taken with the aircraft model of the ESMR on two flights over test fields near Phoenix, Arizona. Note that for this soil (a clay loam) the brightness temperature decreases rapidly for soil moisture values greater than about 20% by weight. There is a large scatter in the data but soil moisture estimates to the nearest 5% are possible in the 20-40% range. Such measurements may provide useful information in the arid regions where large areas with little vegetation are found.

In contrast with soils, the liquid water content of snow seems to increase the radiometric brightness (Reference 30). Very dry snow, less than 1% free water content by volume, showed anomalously low emissivities, less than 0.5 at 26GHz, whereas moist snow, greater than about 5% free water content by volume, showed emissivities greater than 0.9. This effect has been qualitatively observed at 19.35GHz (Reference 31). The effect is not understood theoretically nor adequately characterized experimentally, as yet. Nonetheless, it offers an interesting possibility of observing the onset of melting of the snow in the spring, and of mapping the snow cover in winter.

Like land/water boundaries, ice shows a significant emissivity contrast with water but unlike the case of land/water boundaries are quite variable and their locations are definitely of interest

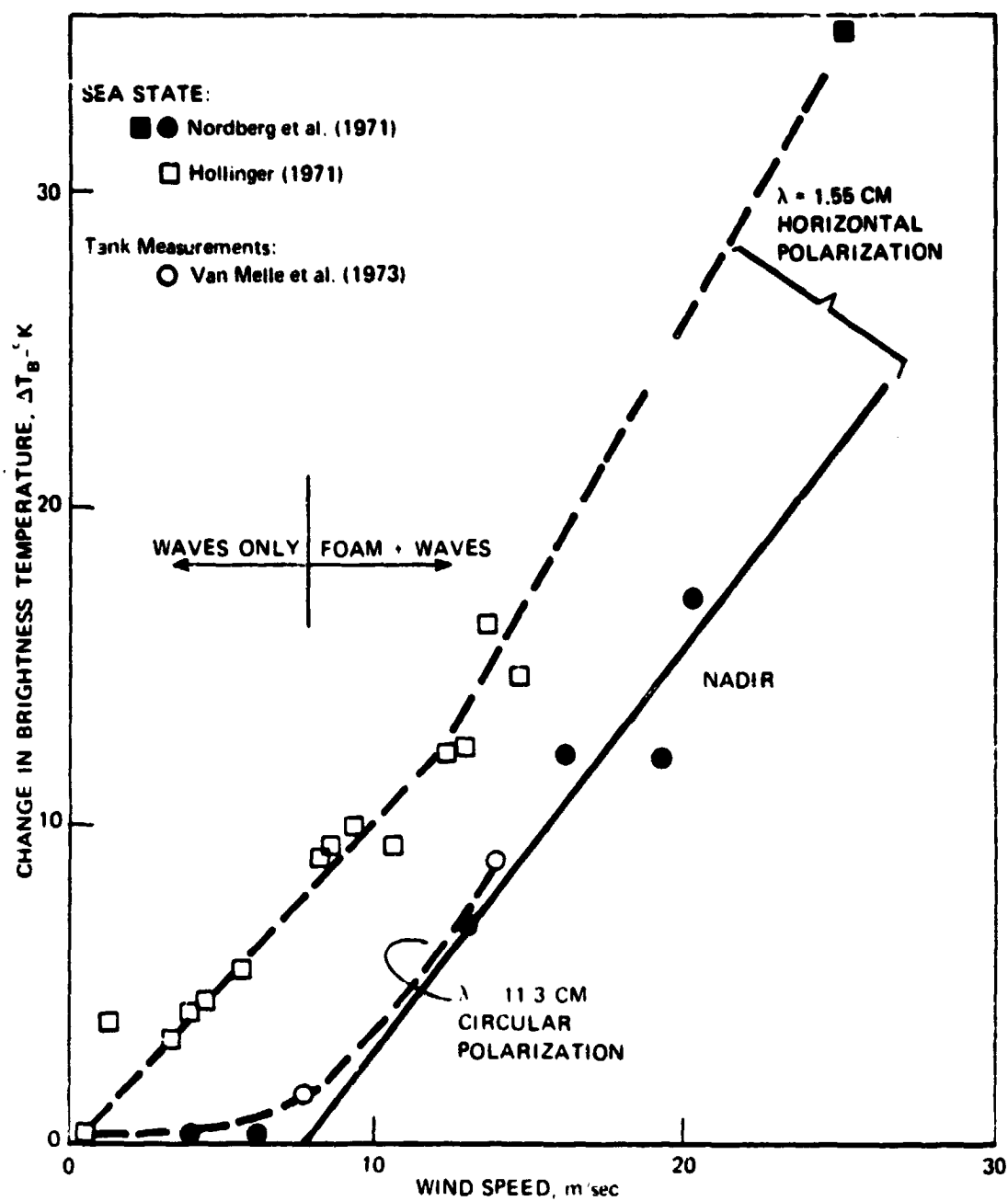


Figure 1-9. Dependence of Brightness Temperature on Sea State

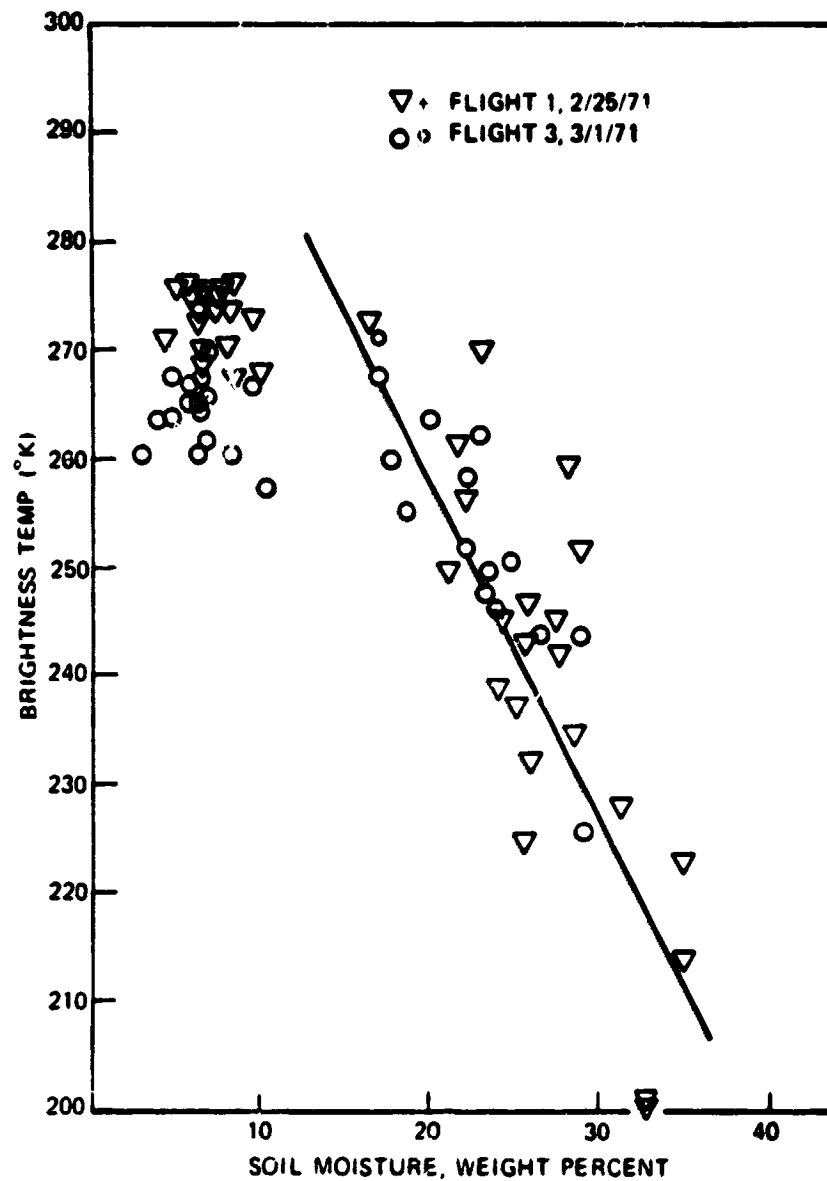


Figure 1-10. Brightness Temperature Results of Bare Fields with Clay Loam Soils, 1.55 cm Radiometer, Phoenix, Arizona

to the meteorological and maritime communities. These features are frequently covered with clouds which makes visible or infrared remote sensing difficult; it is expected that these clouds will rarely, if ever, be dense enough to alter significantly the microwave images. The ice/water boundary has been observed through clouds (Reference 31). The sea itself has been observed to have emissivity variations (Reference 31). These variations, at this point, are thought to be related to age, first year ice being more emissive than multi-year ice. Figure 1-11 shows the spectral nature of these two types of ice. Note that the contrast between the two types seems to increase linearly with frequency. In the non-beam filling situation, this effect will contribute about 10% uncertainty to estimates of the percentage of ice within one resolution element.

1.3.2 SMMR Parameters to be Measured – Frequency Selection

The parameters of interest for the SMMR are given below.

Freq. GHz	Wave Length Cm	Vertical Channel	Horizontal Channel
6.6	4.54	Sea temperature	Separation of surface atmosphere effects; surface winds
10.69	2.81	Rain water in heavy rain; separation of surface and atmospheric effects	Rain water in heavy rain; surface winds
18.0	1.67	Rain water in light rain; separation of surface and atmospheric effects	Rain water in light rain; surface winds
21.0	1.43	Tropospheric water vapor; separation of surface and atmospheric effects	Tropospheric water vapor; surface wind
37.00	0.81	Surface winds (through foam); sea ice/polynyas; old ice/new ice	Same as for vertical channel

The secondary objective is to measure soil moisture (6.6 to 21.0 GHz).

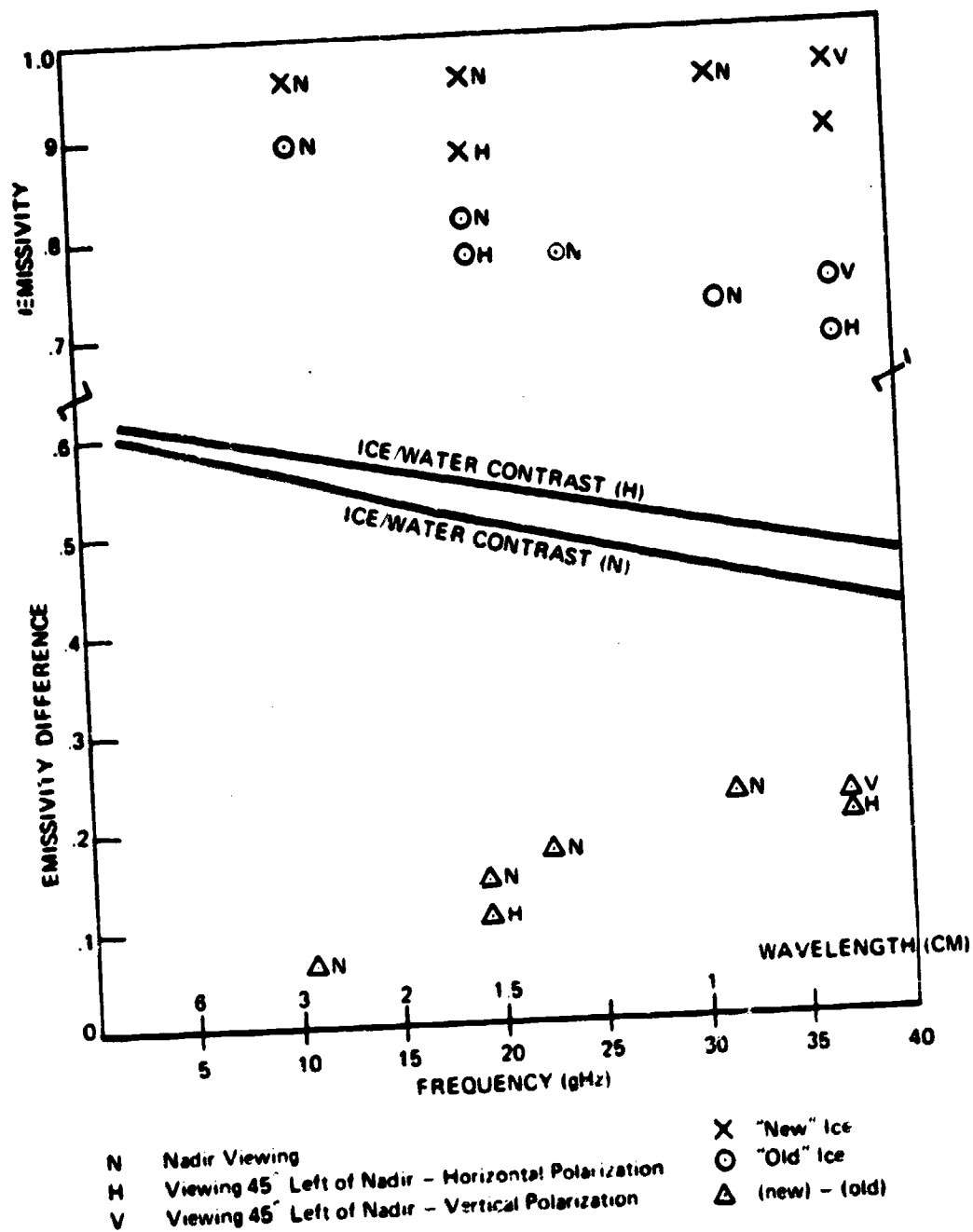


Figure 1-11. Microwave Emissivity Contrasts of Old and New Ice

The primary source for the sea-surface temperature data will be the vertically polarized 6.6 GHz channel. The basic reason for choosing this frequency is its proximity to the peak of the sensitivity curve and a spacecraft design limitation. Two of the major sources of interference, surface foam and heavy rain clouds, are polarization independent, so the horizontally polarized 6.6 GHz channel will be used to provide corrections for these two particular effects. Sea-surface roughness, however, appears to have some dependence on polarization. Since sea-surface roughness is frequency dependent, higher frequency channels that are not affected by the thermodynamic temperature of the water will be used to provide roughness data. The highest frequency channels (37.00GHz) will not be used for this purpose since they are too far removed from the 6.6GHz channels to permit extraction of roughness data by means of the frequency dependence. Although the correction for varying water-vapor concentration at 6.6GHz is not expected to be large in comparison with the corrections previously mentioned, it is nevertheless important. Data from the 21.0GHz channels will be utilized for making this correction. Heavy rainfall will also interfere with the determination of the sea-surface temperature because it will contribute to the sea-surface roughness. It may be possible to use data from the rainwater channels to correct for this interference; the range over which this will be possible remains to be determined.

The 37GHz channels will obtain data on the percentage of foam cover, which will be the prime source for determinations of sea-surface windspeeds (> 7 m/s). This type of determination can be performed best with data from the 37GHz channels, rather than from channels at 19.35GHz where observations have already been made with a mapping radiometer, since the higher frequency is better suited for observing thin layers of foam. Heavy rainfall will render the 37GHz channels useless for wind-speed measurements; under such conditions it may be possible to observe the foam cover at longer wavelengths if the rain striking the sea surface does not obscure it. The 37GHz channels also play an important role in the determination of open water in the polar ice canopies and in the determination of the age of the polar ice.

In addition to the interference caused by raindrops striking the sea surface, the effect of water vapor in the intervening atmosphere must also be properly considered. This is handled best by a real-time measurement approach, with the 21.0GHz channels, which is adjacent to the water-vapor line, used for accurate water-vapor corrections under a wide variety of humidity conditions.

A three-frequency approach has been chosen for the determination of the liquid water in the atmosphere, since this will permit detection of water droplets over a wide range of droplet sizes in both raining and nonraining clouds. Another important advantage of this approach is that it permits the wavelength dependence of the water-droplet signature to be utilized for the unfolding of this particular feature from the rest of the interwoven data. The frequencies chosen for this purpose must be sufficiently removed from the water-vapor line so that the interference is reduced to a manageable level. A frequency of 10.69GHz (a radio-astronomy frequency) has been chosen because it possesses maximum sensitivity to the water droplets found in heavy rainfalls; 18GHz has been selected for lighter rain and also its small response to water-vapor variations; and 37GHz has been selected for determining the amount of liquid water in non-raining clouds because the droplets in this type of cloud are smaller than in raining clouds and because there is an atmospheric window at this frequency.

Dual polarization at all frequencies has been utilized because it will facilitate the separation of surface and atmospheric effects since, in general, the former exhibit polarization and the latter do not.

It also should be emphasized that the dual-polarization approach dictates that observations must be made at angles away from the nadir; the optimum zenith angle for these observations, aside from other considerations, appears to be approximately 50°.

2.0 SMMR SIMULATOR RADIOMETER SYSTEMS DESCRIPTION

2.1 Basic Radiometer Operation

The radiometer systems comprising the SMMR simulator are all of the Dicke type. Each of the radiometers operates in a "receive time share" mode so that data are taken from both the

vertically and horizontally polarized components of the received signal power (T_A). Each radiometer system consists of the following subsystems (Figure 2-1):

- a. Antenna and Radome
- b. Electronics Package
 - 1. Switching and Calibration Network
 - 2. Receiver Electronics
 - 3. Post Detection Processor
- c. Power System
- d. Timing and Control System
- e. Data Buffer and Distribution System

2.2 Subsystem Description

A detailed description of these subsystems is given in Reference 36.

2.2.1 Antenna and Radome

The antenna system gathers the incident power and channels this power into horizontally and vertically polarized components. All antennas have a beamwidth of $6^\circ \pm 1^\circ$ at the 3 dB points. All planes exhibit low sidelobe levels, nominally -30dB maximum. Beam efficiency (percentage of received energy between first nulls) is at least 90%. For those antennas which are installed in the microwave antenna housing ("sled") carried beneath the aircraft body a radome is used for aerodynamic closure.

2.2.2 Electronics Package

2.2.2.1 Switching and Calibration Network

The switching and calibration network (SCN) performs the following functions:

- 1. supplies radiometer RF modulation ("Dicke" operation)
- 2. provides for received electronics time-sharing by switching between antenna polarizations, and
- 3. supplies reference temperature signals near the extremes of the system dynamic range.

The SCN consists of the following subsystems.

- a. switching block
- b. liquid nitrogen load

Its configuration is shown in Figure 2-2A.

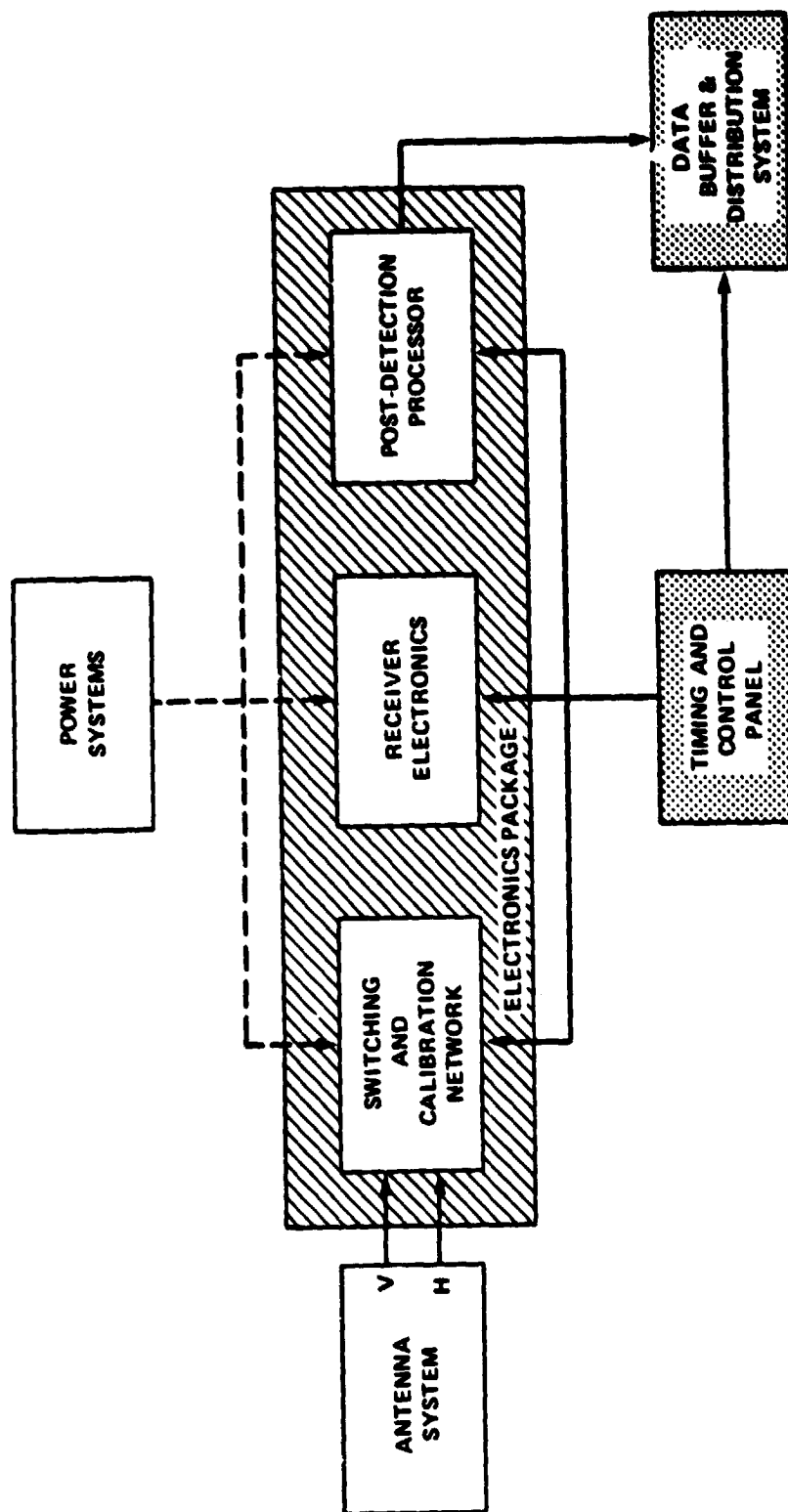


Figure 2-1. Radiometer System Block Diagram

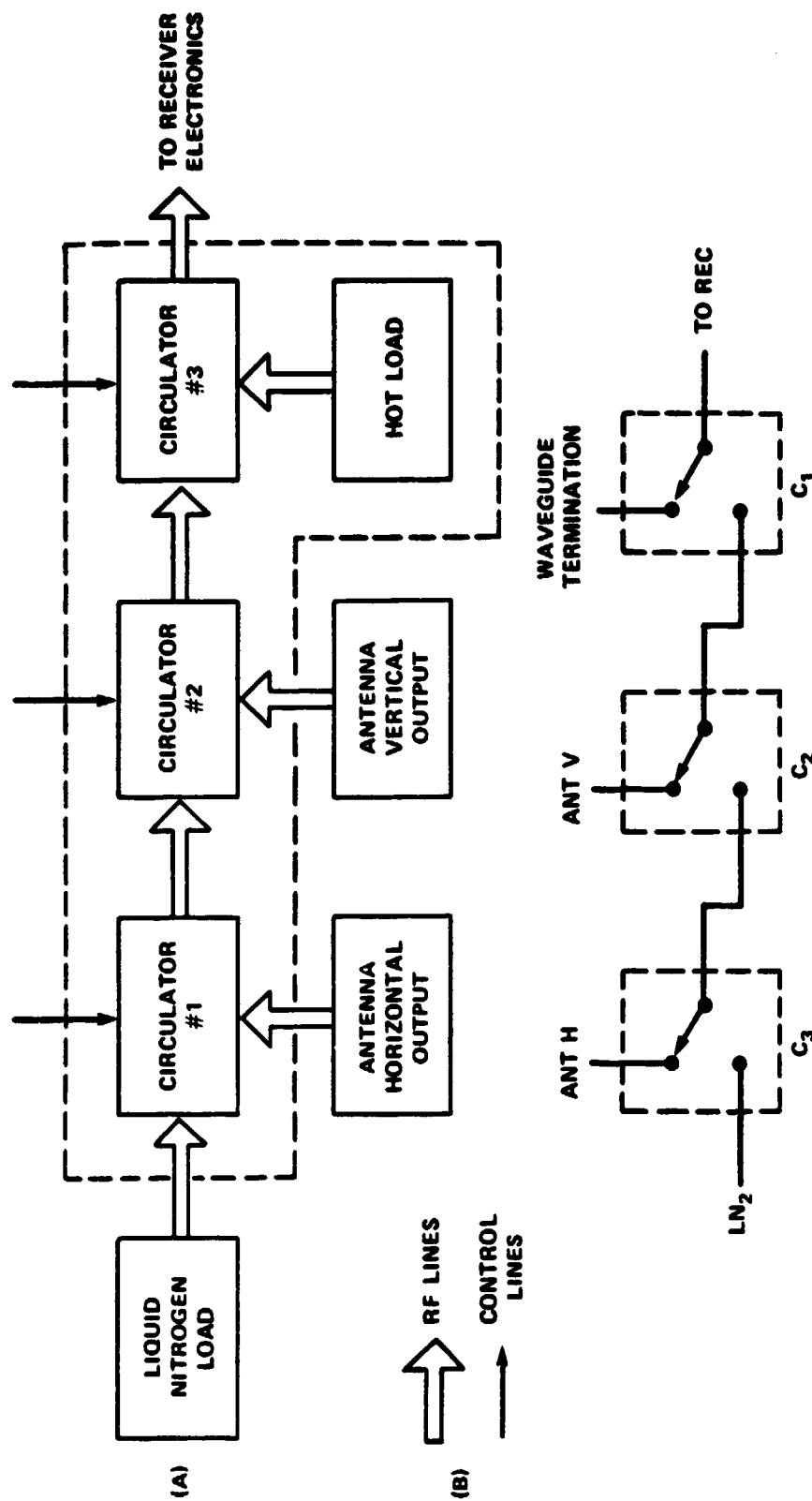


Figure 2-2. Switching and Calibration Network

2.2.2.1.1 Switching Block—The switching block (Figure 2-2B) is composed of latching ferrite circulators, arranged so as to provide three series-connected single-pole double-throw switches, a waveguide termination, and necessary driver circuitry. The temperature of the entire switching block is maintained at approximately 35°C. The circulator states are controlled by the timing and control system.

2.2.2.1.2 Liquid Nitron Load—The liquid nitrogen load consists of a closed cryogenic vessel and a waveguide termination immersed in a bath of LN₂.

2.2.2.2 Receiver Electronics

The receiver electronics converts the modulated FR signal from the SCN into a video signal which is applied to the Post Detection Processor.

2.2.2.3 Post Detection Processor

The post-detection processor synchronously detects the Dicke-modulated video signal and produces an output voltage of 0 to 10 volts DC. The output signal is linearity proportional to the received power, T_A , and is recorded for subsequent data reduction and analysis.

2.2.3 Power System

The power system supplies all required DC power for operation of the radiometer system.

2.2.4 Timing and Control System

The timing and control system provides the appropriate logic-control signals to the switching and calibration network. These select which radiometric measurement (cold ref., hot ref., scene vertical polarization, or scene horizontal polarization) will be processed at any one time.

2.2.5 Data Buffer and Distribution System

The data buffer and distribution system provides formatting, buffering and distribution of all data and status signals from the radiometers and the timing and control system.

2.3 CV-990 Aircraft Installation

2.3.1 Basic Capabilities of the CV-990 as an Experiment Platform

The CV-990 is a four-engine jet aircraft similar in size, appearance, and performance to other narrow-body transport aircraft (e.g., Boeing 707). It has been extensively modified internally to provide for the mounting of experimental equipment. Special equipment has been added to provide 120V 60Hz electrical power (U.S. standard voltage and frequency) in addition to the standard aircraft power, which is 115/200V, 400Hz, three-phase.

Aircraft modifications include additional windows. Three zenith windows have been cut in the ceiling of the cabin. There are eight windows along the left side of the cabin, looking upward at an angle of 65° to the horizontal. One window at an angle of 40° is available, also on the left side of the cabin. There are six nadir viewing windows, four in the forward cargo compartment and two in the aft cargo compartment. In addition, there are three small viewing ports looking downward from the aft cargo compartment. Eleven passenger windows (14° elevation angle) on the left side and one on the right are modified to accept special inserts. All the special windows, zenith, 65°, 40°, nadir and the modified passenger windows can accept special inserts of optical glass or other materials such as IR transmitting plastics. Metal inserts may be installed in these windows as supports for small outboard instrumentation in the airstream. Lightweight equipment such as cameras and photometers can be mounted directly to the frames of the zenith, 65°, 40°, and nadir windows. Wing surfaces are painted black to reduce reflections.

A limited amount of fairly large instrumentation may be mounted outside the aircraft in specially designed fairings. NASA-AMES has a fairing that mounts in a nadir position to the rear of the wing. It was designed primarily for mounting microwave antennas, but other uses of it have been made.

Some additional equipment may be mounted in the cargo holds, which are pressurized, but not heated, and are accessible in flight for equipment servicing.

Special equipment racks developed for this aircraft accept standard U.S. 19-in. (48cm) electronic panel-mounted equipment. Racks can be shipped to the experimenter's laboratory in advance of a mission to aid in the design of the aircraft configuration of the experimental equipment.

The aircraft carries an inertial navigation system (INS), which permits precise flight patterns to be flown accurately. Flight parameters from the INS and other instrumentation are normally displayed on TV monitors installed on the electronics racks. Arrangements can be made for experimenters to obtain data for their use from the INS in flight.

The aircraft also carries a computer system - the Airborne Digital Data Acquisition System (ADDAS). The ADDAS processes INS parameters and aircraft instrument data for the TV displays. It may also be used by experimenters as a high quality computation and recording device. Instrument calibration curves may be programmed to provide real-time readouts, for example. The ADDAS also accepts typed-in comments for the record. Normally, the ADDAS produces a continuous record of aircraft parameters and selected experimenter data. The printouts available after a flight can include the additional typed-in comments from experimenters. These comments will be in their proper chronological position in relation to the parameters normally printed out.

A timing system synchronized to WWV standard time broadcasts can provide a variety of time codes for the experimenter's data record. Individual time readouts are also available.

An aircraft intercom system permits conversation among experimenters and between experimenters and the Flight Director. Intercom outlets are distributed throughout the cabin.

Cryogenic cooling (liquid nitrogen or liquid helium) may be used in flight. Special design approval for safety will be required. The aircraft normally carries a 200-liter supply of liquid nitrogen, primarily to provide dry nitrogen gas for purging. The nitrogen supply is located in the aft cargo compartment.

The aircraft is normally pressurized to an altitude of 8000 ft. equivalent. Cabin temperature is normally maintained in the range of 65-70°F in the cabin. The heat dissipated by the ADDAS will make that portion of the cabin slightly warmer. Special cooling needs of an experiment should be built into the equipment, if possible.

Cabin humidity is low in flight, no more than 10 percent.

For night flights, cabin lighting can be controlled or extinguished altogether. Fireproofed black cloth can be provided to shroud lightsensitive equipment.

Windows, especially single-thickness optical windows, tend to frost or fog in flight. Special ducts to vent warm air over these windows can be provided and are usually necessary.

The cargo compartments are pressurized but are usually much cooler than the cabin.

2.3.2 SMMR Simulator CV-990 Installation

The radiometer systems/subsystems comprising the SMMR Simulator are installed at various locations, thus in various environments, through-out the CV-990 as noted below:

- (1) The Timing and Control System and the Data Buffer and Distribution System are both rack mounted and housed in the main cabin area.
- (2) The lower frequency units: 6.6, 10.7, 18GHz; are installed with their respective electronics packages in the aft cargo bay and their antennae housed in the Microwave Antenna Housing ("sled"). These units have a radome closure in front of the antenna.
- (3) The higher frequency units: 21 and 37GHz; are installed in the cabin area with their antennae mounted in 14° elevation angle windows.
- (4) All antenna/electronics package waveguide interconnections are heated and thermostatically controlled at approximately 20°C.
- (5) Only the 6.6GHz antenna is heated and thermostatically controlled. All other antenna systems take on their ambient environment temperature.
- (6) Antenna and waveguide temperatures are monitored using thermistors. These monitor points are routed to the DBDS for recording.

Table 2-1 summarizes the subsystem installation locations.

Table 2-1

Radiometer System	Electronics Package	Antenna System	Waveguide Connections
6.6	Aft Cargo	Sled	Cargo, Sled
10.7	Aft Cargo	Sled	Cargo, Sled
18	Aft Cargo	Sled	Cargo, Sled
21	Cabin	Window	Cabin
21 Uplook	Cabin	Window	Cabin
37	Cabin	Window	Cabin

The installation for the engineering check flight series flown in the 3rd quarter of FY77 is shown in the following photographs. Two installation changes were incorporated between the engineering check flights and the Fall 1978 Nimbus-6 underflight series:

- (1) 4.99GHz radiometer replaced with the 6.6GHz system-6.6GHz installed at same location as 4.99GHz system in photo.
- (2) Uplooking 21GHz and 37GHz antennas were combined as one antenna system in existing 21GHz antenna. This allowed fabrication of shorter waveguides for the antenna/electronics package interconnects for the 21 and 37GHz radiometer systems.

(These photographs were taken during installation operations and thus do not show the finished installation wherein heaters and insulation are on all waveguides. Also, the window mounted antennas were enclosed in an aerodynamic fairing.)

3.0 BASIC RADIOMETRIC EQUATION-DERIVATION

For the SMMR, the radiometer output voltage is linearly proportional to the power of the input signal, which is produced either by a warm or cold (liquid nitrogen) reference load or by the microwave radiation incident upon the antenna.

V_A represents the output voltage in response to an input signal from the antenna of brightness temperature, T_A . Linearity of the radiometer implies

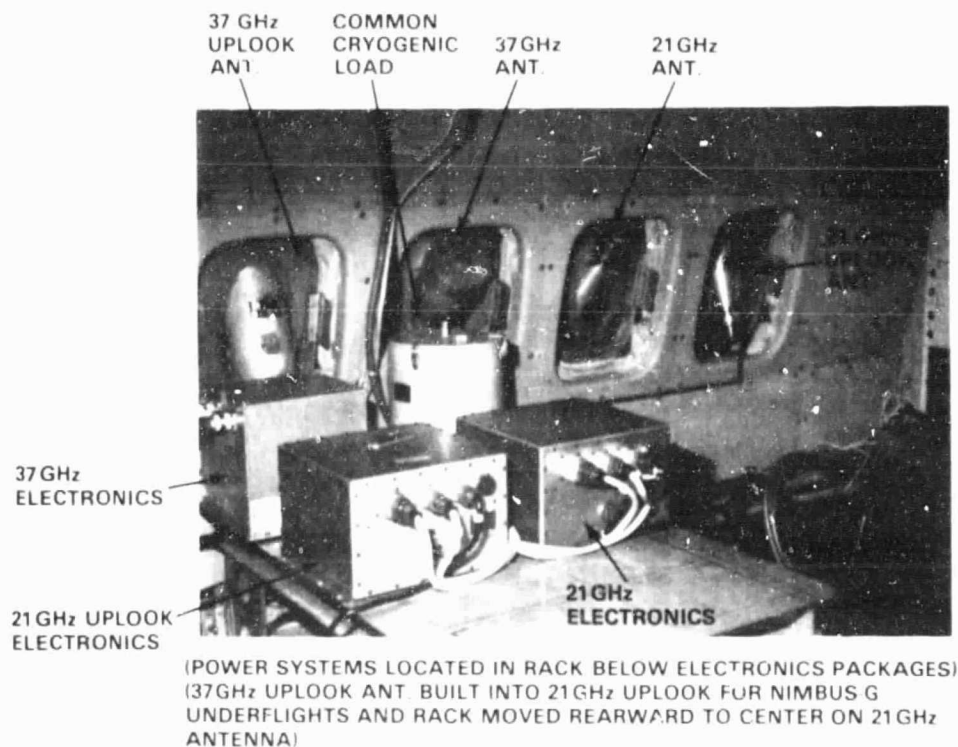


Figure 2-3. Cabin Installation

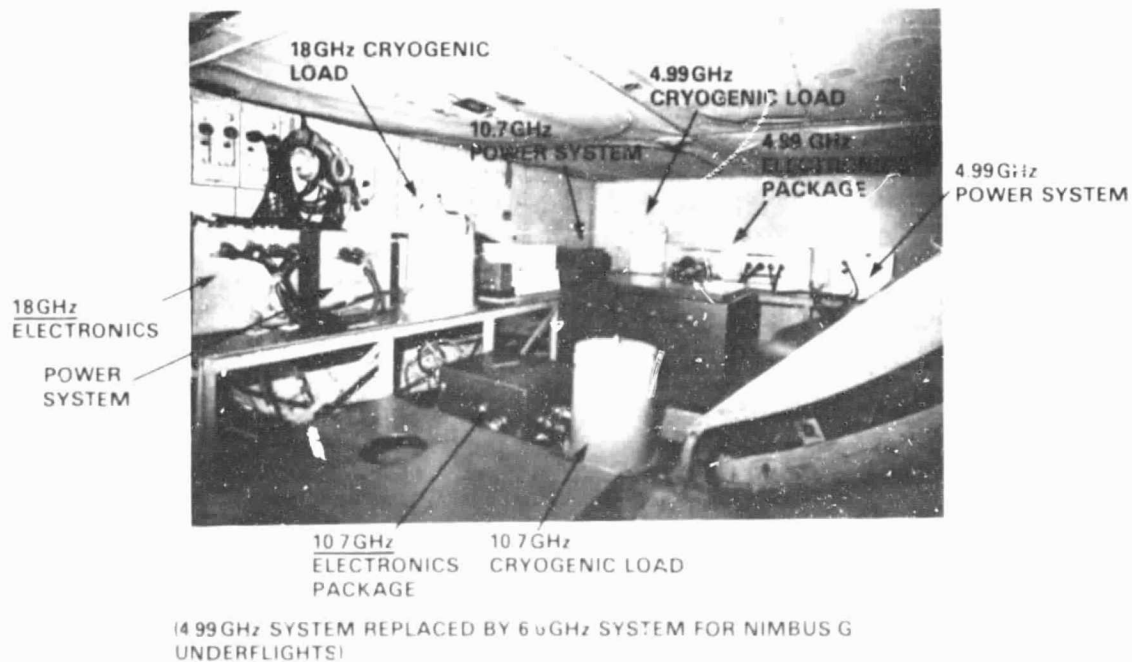


Figure 2-4. All Cargo Bay Installation

ORIGINAL PAGE 2
OF 8 - R 100-170

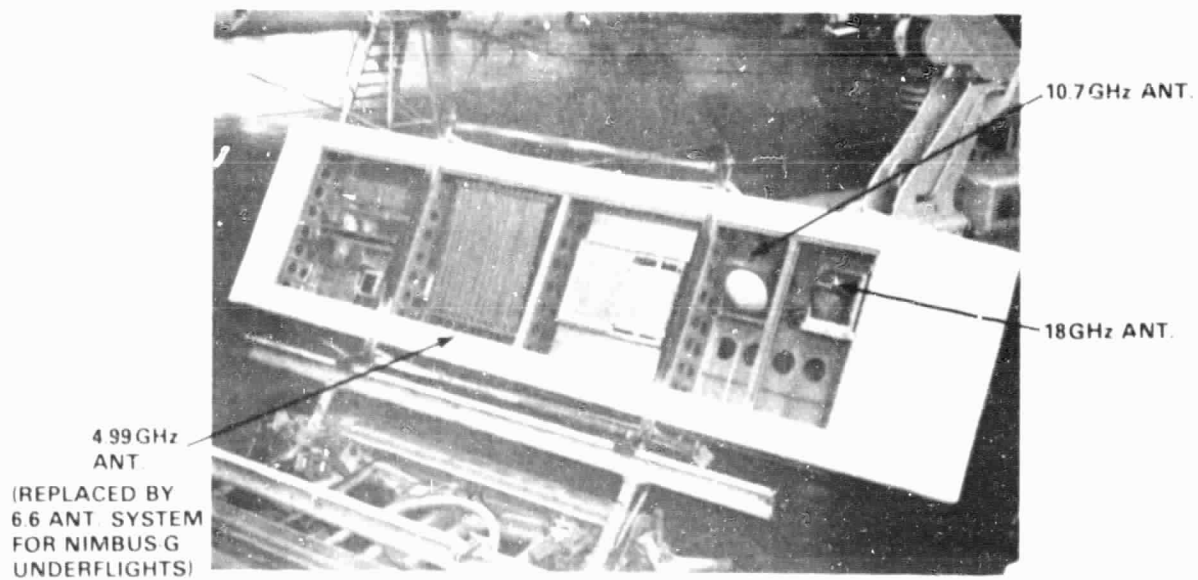


Figure 2-8 Microwave Antenna Housing ("SLID")

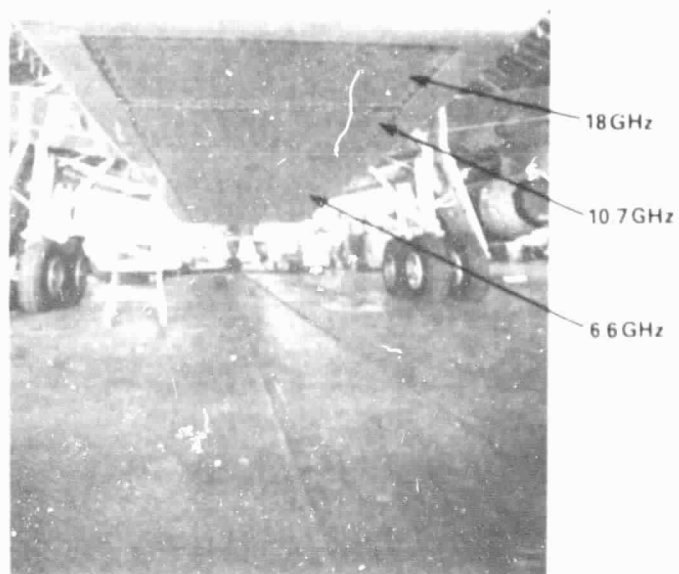


Figure 2-9 Radome Closures

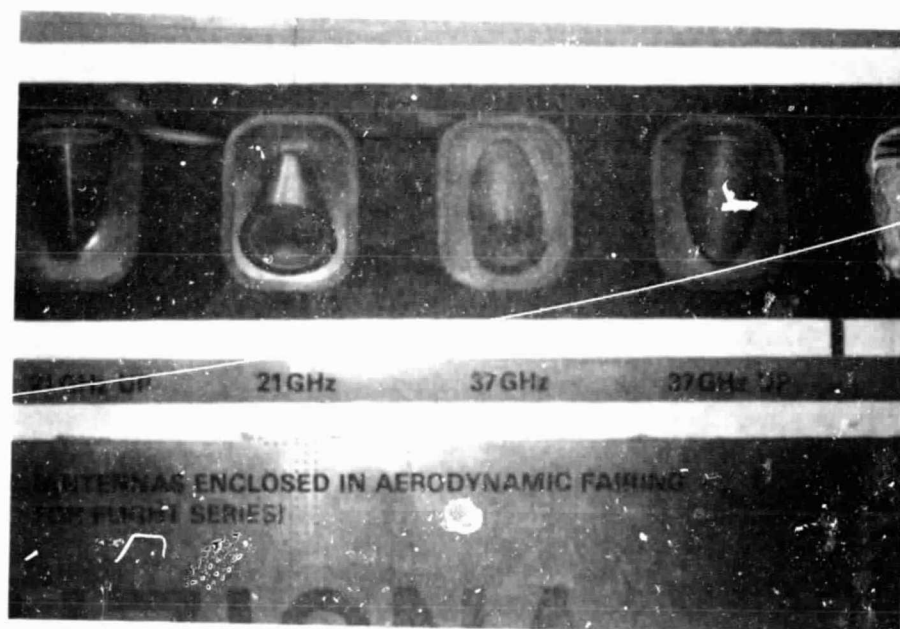


Figure 2- Window Mount Antennas

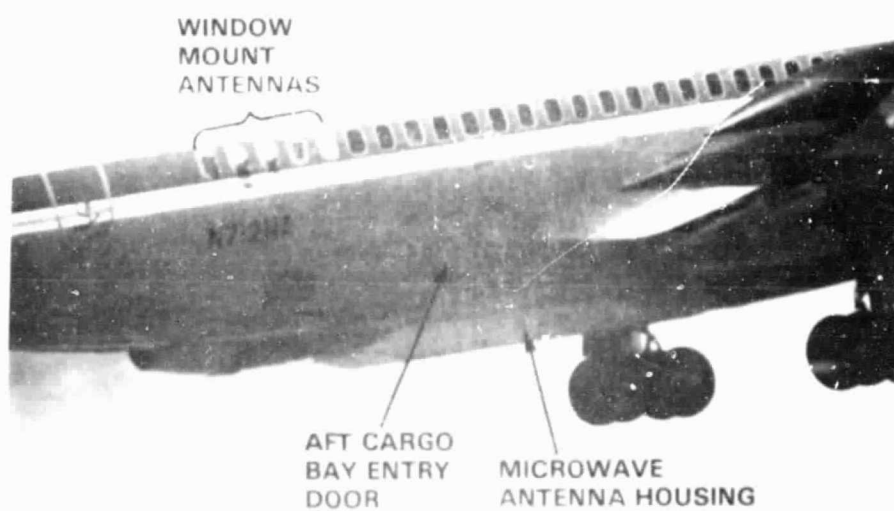


Figure 3- Aft Cargo Bay Entry Door

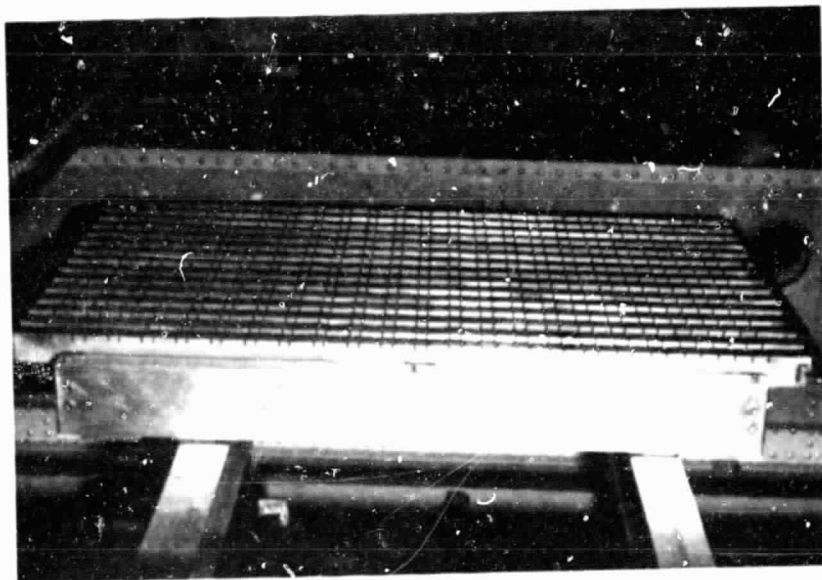


Figure 2-9 6.6GHz Antenna (Vertical Polarization)

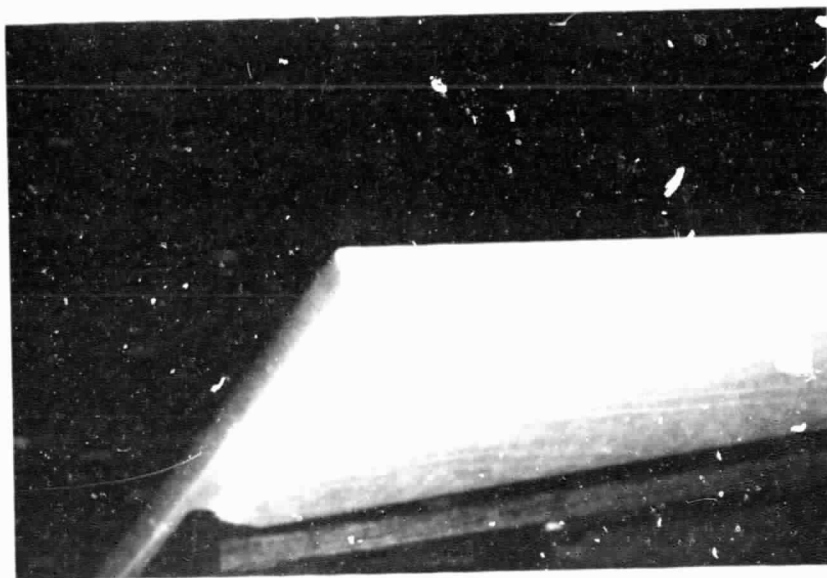
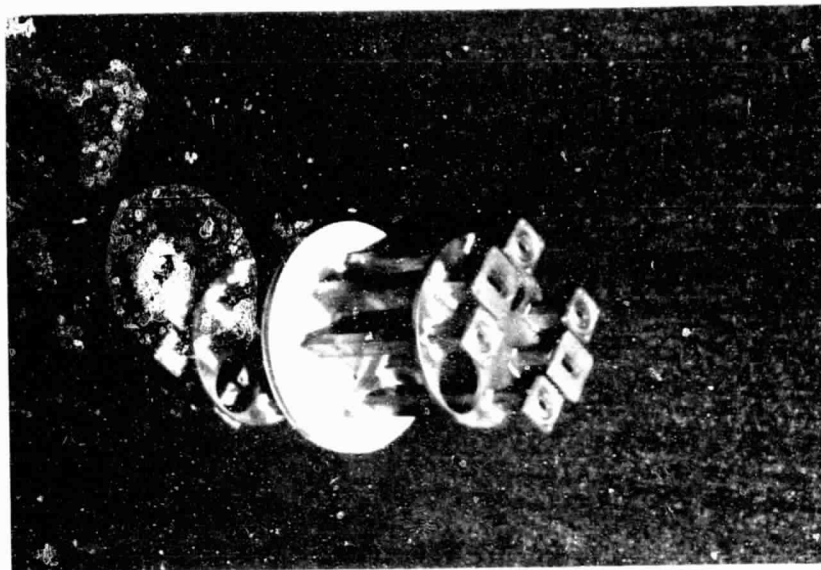
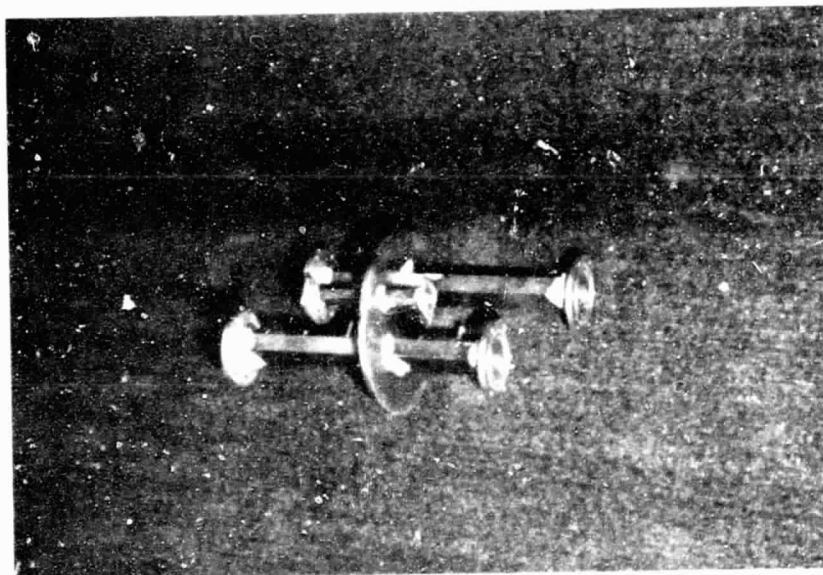


Figure 2-10 6.6GHz Radome



10.7GHz
AND
18GHz



6.6GHz

Figure 2-11. Aircraft Skin Waveguide Feedthru Alt Cargo to SLED



Figure 2-12. 10.7 and 18GHz Waveguide Runs - Att Cargo

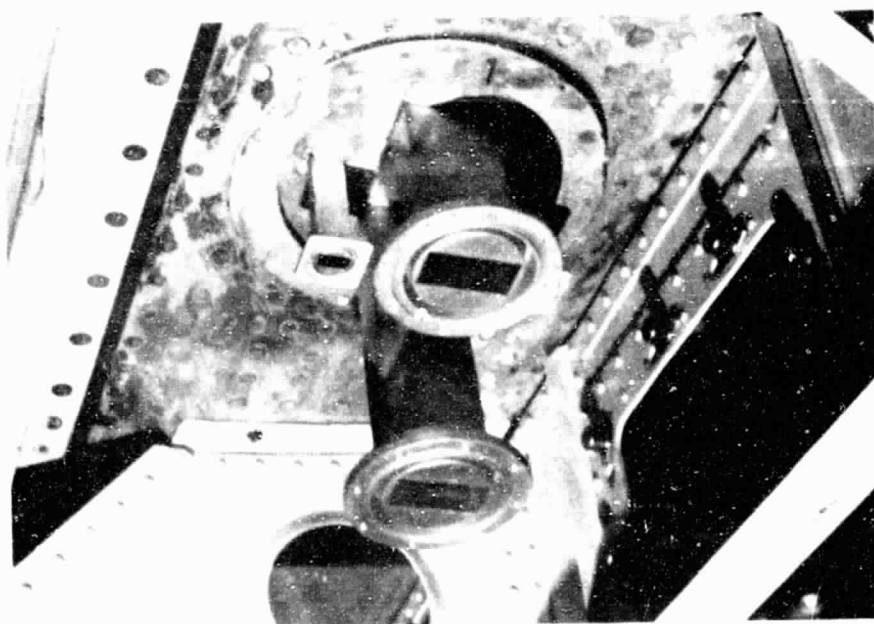


Figure 2-13. 6.6GHz Feedthru - Installed

$$V_A = u + vT_A \quad (3-1a)$$

where u is a constant offset voltage, and v is a proportionality constant. Similarly, when signals are observed from the warm and cold calibration sources at the effective radiometric temperatures, T_w and T_c , respectively, the radiometer response is

$$V_w = u + vT_w \quad (3-1b)$$

and

$$V_c = u + vT_c \quad (3-1c)$$

Voltages V_A , V_w , and V_c are measurable quantities. To eliminate calibration constants u and v , it is useful to define the parameter N , referred to as the "normalized voltage" or "normalized counts":

$$N = \frac{V_A - V_w}{V_c - V_w} \quad (3-2)$$

Substitution of Equation (3-1) into Equation (3-2) yields

$$N = \frac{(u + vT_A) - (u + vT_w)}{(u + vT_c) - (u + vT_w)} = \frac{T_A - T_w}{T_c - T_w} \quad (3-3)$$

After rearrangement, this becomes the radiometric equation

$$T_A = T_w + (T_c - T_w)N \quad (3-4)$$

Equation (3-4) relates the incident radiation intensity, T_A , to the observed normalized voltage, N , and two effective radiometric calibration temperatures, T_w and T_c .

This relationship is, however, incomplete in-as-much-as it does not take into account any system losses which will cause aberrations to the absolute temperatures T_A , T_w , T_c . These effects are considered in Section 4 and expressions formally equivalent to Equation (3-4) are derived by applying basic microwave radiative transfer theory to the SMMR collection system.

This procedure illustrates the relationships between the calibration constants, T_w and T_c , and the thermodynamic temperatures of the various components of the collection system.

4.0 SMMR SIMULATOR SYSTEM LOSSES – RADIATIVE TRANSFER ANALYSIS

4.1 Radiative Transfer Theory

This section examines the relationship between the radiation field reaching the SMMR collection system and the signal that eventually reaches the radiometer. Incident radiation does not pass unimpeded to the radiometer but is attenuated by losses in the waveguides and various switches. At the same time, thermal emissions by the lossy components contribute to the signal observed at the radiometer. The equation of microwave radiative transfer (References 39 and 40) may be used to relate the intensities of the two radiation fields as a function of the various system losses. In the following discussion, the Rayleigh-Jeans approximation to the Planck radiation law is assumed to be valid and is used throughout.

4.1.1 Radiative Transfer Theory Applied to a Cascade of Lossy Elements

Consider the transfer of radiation across a single lossy plane-parallel element, as illustrated in Figure 4-1, where the incident radiation is characterized by a brightness temperature, T_0 , and the output signal by T_1 . The lossy slab is at thermodynamic temperature t_1 , and has an effective transmissivity, α_1 .

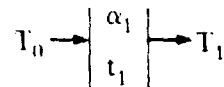


Figure 4-1. Radiative Transfer Across a Plane-Parallel Slab

The equation of radiative transfer becomes

$$T_1 = \alpha_1 T_0 + (1 - \alpha_1) t_1 \quad (4-1)$$

The effect of an additional loss is illustrated in Figure 4.2.

The second lossy slab is at thermodynamic temperature t_2 , and has an effective transmissivity, α_2 .

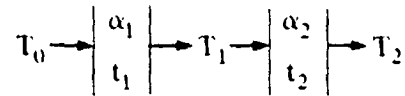


Figure 4-2. Radiative Transfer Across Two Plane-Parallel Slabs

The output signal, T_2 , is

$$T_2 = \alpha_2 T_1 + (1 - \alpha_2) t_2 \quad (4.1-2a)$$

$$T_2 = \alpha_2 [\alpha_1 T_0 + (1 - \alpha_1) t_1] + (1 - \alpha_2) t_2 \quad (4.1-2b)$$

$$T_2 = \alpha_1 \alpha_2 T_0 + [(1 - \alpha_1) t_1] \alpha_2 + (1 - \alpha_2) t_2 \quad (4.1-2c)$$

The original signal, T_0 , is reduced by the product of the two transmissivities, and the emission from the first lossy slab is, in turn, attenuated by the second.

If the signal T_2 now passes through a third lossy element the system becomes a cascaded triple loss as illustrated in Figure 4-3. The third lossy slab is at thermodynamic temperature, t_3 and has an effective transmissivity, α_3 . The output signal, T_3 , is given by

$$T_3 = \alpha_3 T_2 + (1 - \alpha_3) t_3 \quad (4.1-3a)$$

$$T_3 = \alpha_1 \alpha_2 \alpha_3 T_0 + [(1 - \alpha_1) t_1] \alpha_2 \alpha_3 + [(1 - \alpha_2) t_2] \alpha_3 + (1 - \alpha_3) t_3 \quad (4.1-3b)$$

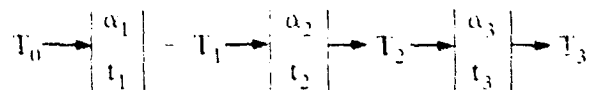


Figure 4-3. Radiative Transfer Across Three Plane-Parallel Slabs

If a cascaded triple loss system is characterized by

$$t_1 = t_2 = t_3 = t_0$$

the equation for radiative transfer becomes

$$T_3 = \alpha_3 \{ \alpha_2 [\alpha_1 T_0 + (1 - \alpha_1) t_0] + (1 - \alpha_2) t_0 \} + (1 - \alpha_3) t_0 \quad (4.1-4a)$$

$$T_3 = \alpha_1 \alpha_2 \alpha_3 T_0 + (1 - \alpha_1 \alpha_2 \alpha_3) t_0 \quad (4.1-4b)$$

The effects of thermal losses in the SMMR simulator collection system can be calculated by repeated application of this method. The input signal at the switch block, T_{F1} , can be computed from T_0 by applying expressions analogous to Equations (4.1-1), (4.1-2) and (4.1-3) across the entire network of losses traversed by the incident radiation. Section 4.2 develops the loss equations for the elements external to the switch block for the SMMR Simulator Radiometers.

4.1.2 Application to Cascade of Ferrite Circulator Junctions

As with the losses external to the ferrite switch block, incident radiation does not pass unimpeded through the switch block but is attenuated by losses in the various switches. The thermal emissions of the switch components also contribute to the signal received at the radiometer. The ferrite switch block used in the SMMR simulator is a cascade of two port ferrite circulators. A typical circulator, shown in Figure 4-4 consists of two input ports, T_{in1} and T_{in2} , one output port, T_{out} , and a ferrite element, F , in the center which is magnetically biased to provide direction of circulation through the junction.

If the ferrite is biased for clockwise circulation, T_{out} is proportional to T_{in1} . A term, α , defined as the direct path transmissivity relates the two signals, T_{out} and T_{in1} , as seen in Equation 4.1-5.

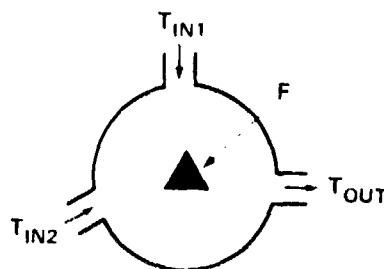


Figure 4-4. Typical Ferrite Junction-Circulator

$$T_{out} = T_{in1}\alpha + \text{an emissivity component of junction} \quad (4.1-5)$$

A certain amount of T_{in2} leaks to the output, T_{out} , due to incomplete termination of the counter-clockwise signal path. Therefore, a fraction of T_{in2} is also found in T_{out} . A leakage term, β , defined as the indirect path transmissivity, relates T_{in2} to T_{out} in Equation (2).

$$T_{out} = T_{in2}\beta + \text{an emissivity component of junction} \quad (4.1-6)$$

The total output can be defined as:

$$T_{out} = T_{in1}\alpha + T_{in2}\beta + \text{junction emissivity} \quad (4.1-7)$$

The effective junction emissivity,

$$\text{Emissivity} = \left(1 - \sum \frac{1}{\text{junction losses}}\right) t_{\text{junction}} \quad (4.1-8)$$

takes into account the total thermal emissivity of the junction. The losses in the junction include the direct path loss and the leakage loss. The temperature of the junction will be referred to as t_{junc} . The equation for the junction emissivity is

$$\epsilon = (1 - \alpha - \beta) t_{\text{junc}}. \quad (4.1-9)$$

Therefore the complete equation for total output becomes

$$T_{out} = T_{in1}\alpha + T_{in2}\beta + (1 - \alpha - \beta) t_{\text{junc}}. \quad (4.1-10)$$

Consider a double cascade of junctions where the temperatures for each junction are equal. A schematic representation of the system is shown in Figure 4-5.

Let α_{jk} be defined as the direct path transmissivity and β_{jk} be defined as the leakage loss where the subscript j refers to the junction number and k refers to the junction switch position. The junction position, $k = 1$ is indicative of clockwise rotation of the signal path while $k = 2$ indicates counter-clockwise rotation. Case 1, as shown in Figure 4-5, shall be examined in addition

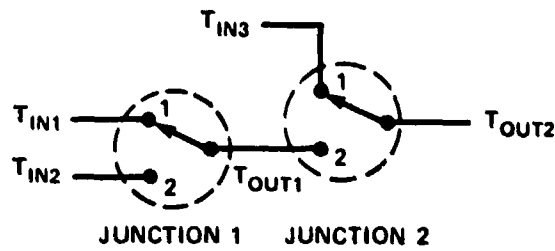


Figure 4-5. Schematic Representation
Two Junction Ferrite Switch
Configuration-Case 1

to all other cases of possible switch configurations. The equation for the output from Junction 1, T_{out1} is given as follows:

$$T_{out1} = T_{in1}\alpha_{11} + T_{in2}\beta_{11} + (1 - \alpha_{11} - \beta_{11})t \quad (4.1-11)$$

(in which all subscripts 11 refer to the first junction being in the first switch position). The output from junction 2, T_{out2} , is seen in Equation (4.1-12)

$$T_{out2} = T_{in3}\alpha_{21} + T_{out1}\beta_{21} + (1 - \alpha_{21} - \beta_{21})t \quad (4.1-12)$$

(The subscripts 21 indicate that the second junction is in the first switch position.) Substituting Equation (4.1-11) into Equation (4.1-12) yields the following:

$$T_{out2} = T_{in3}\alpha_{21} + [T_{in1}\alpha_{11} + T_{in2}\beta_{11} + (1 - \alpha_{11} - \beta_{11})t]\beta_{21} + (1 - \alpha_{21} - \beta_{21})t \quad (4.1-13)$$

which reduces to:

$$T_{out2} = T_{in3}\alpha_{21} + (T_{in1}\alpha_{11} + T_{in2}\beta_{11})\beta_{21} + [1 - \alpha_{21} - (\alpha_{11} + \beta_{11})\beta_{21}]t \quad (4.1-14)$$

Now, examine the switch configuration in Figure 4-6, in which junction 2 is now in the second switch position.

The equation for the output of the first junction is identical to the output equation of the first junction in the previous case (Recall Equation (4.1-11)).

$$T_{out1} = T_{in1}\alpha_{11} + T_{in2}\beta_{11} + (1 - \alpha_{11} - \beta_{11})t \quad (4.1-15)$$

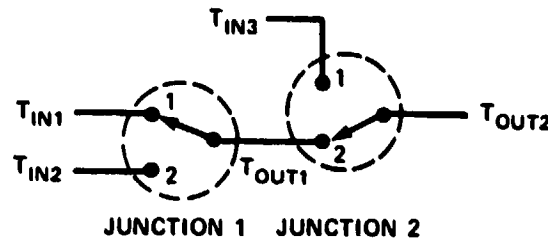


Figure 4-6. Schematic Representation
Two Junction Ferrite Switch
Configuration-Case 2

However, the equation for the output from Junction 2 for this case differs from the previous case, as seen below,

$$T_{OUT2} = T_{OUT1}\alpha_{22} + T_{IN3}\beta_{22} + (1 - \alpha_{22} - \beta_{22})t \quad (4.1-16)$$

When Equation (4.1-15) is substituted into Equation (4.1-16) one obtains the equation for T_{OUT2} for switch configuration 2.

$$T_{OUT2} = (T_{IN1}\alpha_{11} + T_{IN2}\beta_{11})\alpha_{22} + T_{IN3}\beta_{22} + [1 - \beta_{22} - (\alpha_{11} + \beta_{11})\alpha_{22}]t \quad (4.1-17)$$

The third possible switch configuration is shown in Figure 4-7.

The equation for T_{OUT1} is found below:

$$T_{OUT1} = T_{IN2}\alpha_{12} + T_{IN1}\beta_{12} + (1 - \alpha_{12} - \beta_{12})t \quad (4.1-18)$$

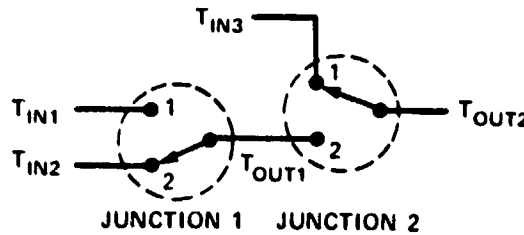


Figure 4-7. Schematic Representation
Two Junction Ferrite Switch
Configuration - Case 3

Note that the direct path loss α_{12} now is coupled with T_{in2} . The output from junction 2, T_{out2} , is defined in Equation (4.1-19)

$$T_{out2} = T_{in3}\alpha_{21} + T_{out1}\beta_{21} + (1 - \alpha_{21} - \beta_{21})t \quad (4.1-19)$$

Substitution and reduction yield the final form of the Equation for case 3.

$$T_{out2} = (T_{in1}\beta_{12} + T_{in2}\alpha_{12})\beta_{21} + T_{in3}\alpha_{21} + [1 - \alpha_{21} - (\alpha_{12} + \beta_{12})\beta_{21}]t \quad (4.1-20)$$

The final case where both junctions are in the second switch position is schematically represented in Figure 4-8.

The equation for the output of junction 1 is identical for that found in the preceeding case, and is repeated below.

$$T_{out1} = T_{in2}\alpha_{12} + T_{in1}\beta_{12} + (1 - \alpha_{12} - \beta_{12})t \quad (4.1-21)$$

The output from junction 2, T_{out2} , for this case is defined in Equation (4.1-22)

$$T_{out2} = T_{out1}\alpha_{22} + T_{in3}\beta_{22} + (1 - \alpha_{22} - \beta_{22})t \quad (4.1-22)$$

With the previously used methods, Equation (4.1-22) undergoes substitution and reduction to obtain a final expression for T_{out2} -case 4.

$$T_{out2} = (T_{in2}\alpha_{12} + T_{in1}\beta_{12})\alpha_{22} + T_{in3}\beta_{22} + [1 - \beta_{22} - (\alpha_{12} + \beta_{12})\alpha_{22}]t \quad (4.1-23)$$

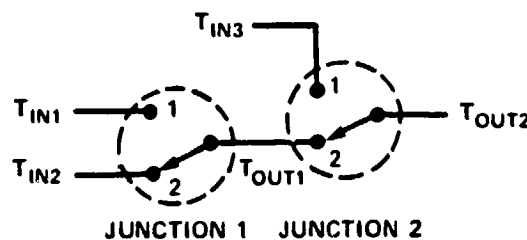


Figure 4-8. Schematic Representation
Two Junction Ferrite Switch
Configuration-Case 4

Similar expansion methods may be utilized to obtain the system output equations for tri-cascaded and quadruple cascaded ferrite switch junctions as are found in the SMMR simulator radiometers. Section 4.3 will develop the loss equations for the ferrite block for the SMMR simulator radiometers.

4.2 Losses External to the Switch Block

The losses experienced by the incident radiation external to the switch block vary according to the physical installation of the different radiometer systems in the CV-990 aircraft. Table 4-1 reviews the physical location of the radiometer system components in the CV-990 (See Section 2.3).

As was noted in Section 2.2.1, the antenna system channelizes the incident radiation field so that the vertically and horizontally polarized components travel through different waveguides from the antenna system to the switch block.

For purposes of this analysis, we shall define the following terms:

1. $T_{MN} \equiv$ effective radiometric temperature
2. $\alpha_{MN} \equiv$ transmissivity of the lossy element
3. $E_{MN} \equiv$ emissivity of the lossy element $\equiv 1 - \alpha_{MN}$
4. $t_{MN} \equiv$ physical temperature of the lossy element

where the subscript M identifies a particular lossy component (Table 4-2) and N delineates the various signal paths within the system (Table 4-2, Figure 4-9 through 4-13).

Table 4-1

Radiometer System	Electronics Package	Antenna System	Waveguide Connections
0.6	Aft Cargo	Sled	Cargo, Sled
10.7	Aft Cargo	Sled	Cargo, Sled
18	Aft Cargo	Sled	Cargo, Sled
21	Cabin	Window	Cabin
21 uplook	Cabin	Window	Cabin
37	Cabin	Window	Cabin

Table 4-2

Value	M	N
0	incident radiation	common to vertical and horizontal
1	radome	warm calibration load
2	antenna	vertical polarization
3	sled waveguide	horizontal polarization
4	cargo waveguide	cold calibration load
5	cabin waveguide	uplooking channel
6	cold load waveguide	N/A
F	switch block input	N/A

If the antenna patterns have cross-polarized sidelobes, there will be a mixture of the vertically and horizontally polarized components of the incident radiation. ρ_1 is defined as the percentage of the vertically polarized radiation mixed into the horizontally polarized channel, and ρ_2 is defined similarly for the vertically polarized channel.

The sections immediately following provide a detailed description of the external loss networks for each radiometric system. In each case, equations are obtained which relate the effective brightness temperatures at the input terminal of the switch block to the various incident brightness temperatures (scene, cold load, warm load).

4.2.1 6.6GHz and 10.7GHz Radiometers

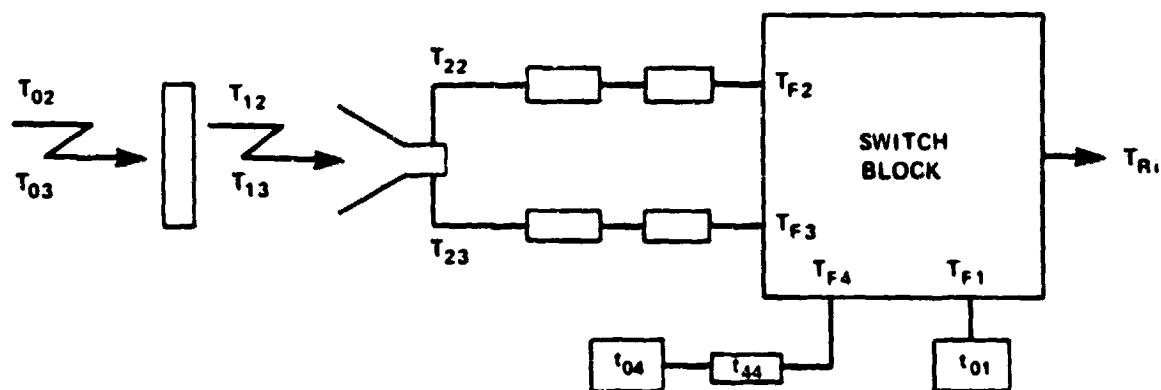


Figure 4-9

$$T_{12} = T_{02}\alpha_{12} + E_{12}t_{10} \quad (4.2-1a)$$

$$T_{13} = T_{03}\alpha_{13} + E_{13}t_{10} \quad (4.2-1b)$$

$$T_{23} = [(1 - \rho_1)T_{13} + \rho_1 T_{12}]\alpha_{23} + E_{23}t_{20} \quad (4.2-2a)$$

$$T_{22} = [(1 - \rho_2)T_{12} + \rho_2 T_{13}]\alpha_{22} + E_{22}t_{20} \quad (4.2-2b)$$

$$T_{F1} = t_{01} \quad (4.2-3)$$

$$T_{F2} = (T_{22}\alpha_{32} + E_{32}t_{32})\alpha_{42} + E_{42}t_{42} \quad (4.2-4)$$

$$T_{F3} = (T_{23}\alpha_{33} + E_{33}t_{33})\alpha_{43} + E_{43}t_{43} \quad (4.2-5)$$

$$T_{F4} = t_{04}\alpha_{60} + E_{60}t_{60} \quad (4.2-6)$$

4.2.2 18GHz Radiometer

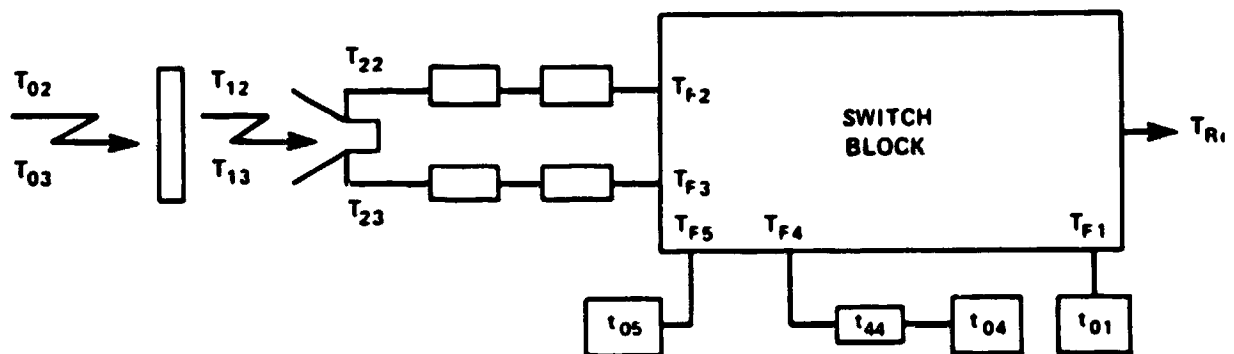


Figure 4-10

- Note: 1. t_{05} \Rightarrow physical temperature of a termination
 2. $t_{05} = t_{01}$

Loss term equations for the 18GHz radiometer are identical to the equations for the 0.6GHz and 10.7 GHz radiometers (Eqs. (4.2-1) through (4.2-6)).

One additional equation is required

$$T_{1,5} = t_{05} = t_{01} \quad (4.2-7)$$

4.2.3 21GHz Radiometer

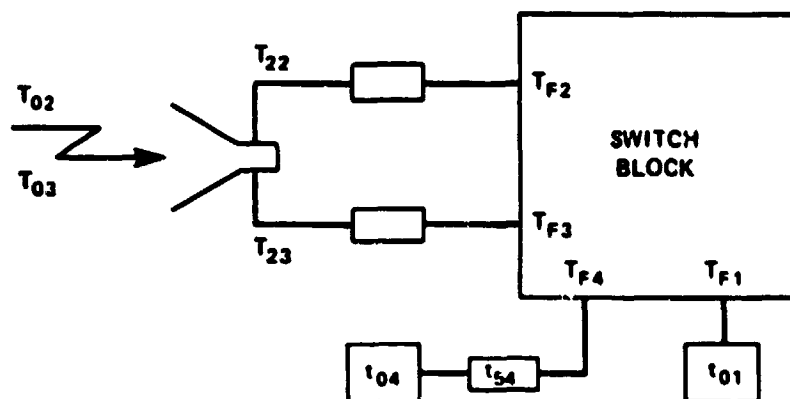


Figure 4-11

$$T_{23} = [(1 - \rho_1)T_{03} + \rho_1 T_{02}] \alpha_{23} + E_{23} t_{20} \quad (4.2-8a)$$

$$T_{22} = [(1 - \rho_2)T_{02} + \rho_2 T_{03}] \alpha_{22} + E_{22} t_{20} \quad (4.2-8b)$$

$T_{1,1}$ see Equation (4.2-3)

$$T_{1,2} = T_{22} \alpha_{52} + E_{52} t_{52} \quad (4.2-9)$$

$$T_{1,3} = T_{23} \alpha_{53} + E_{53} t_{53} \quad (4.2-10)$$

$T_{1,4}$ see Equation (4.2-6)

4.2.4 21GHz Uplook Radiometer

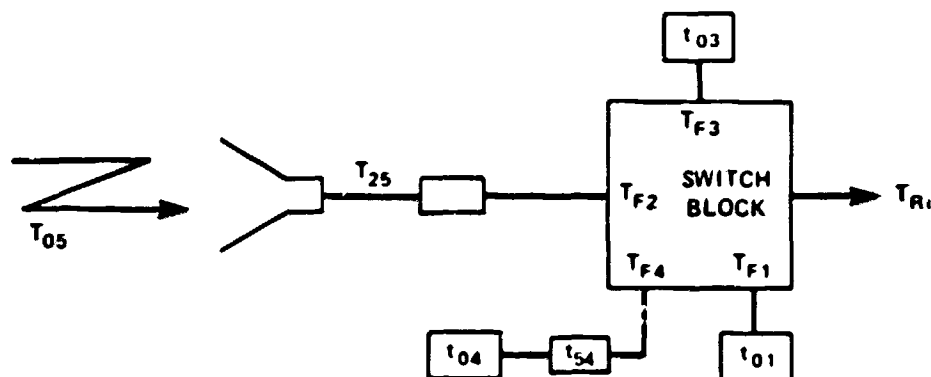


Figure 4-12

Note: 1. $t_{03} \Rightarrow$ physical temperature of a termination, $t_{03} = t_{01}$

2. Uplink channel for 21 GHz uses the vertical channel switch block input port

$$T_{25} = T_{05}\alpha_{25} + E_{25}t_{25} \quad (4.2-11)$$

T_{F1} see Equation (4.2-3)

$$T_{F2} = T_{25}\alpha_{55} + E_{55}t_{55} \quad (4.2-12)$$

$$T_{F3} = t_{01} \quad (4.2-13)$$

T_{F4} see Equation (4.2-6)

4.2.5 37 GHz Radiometer

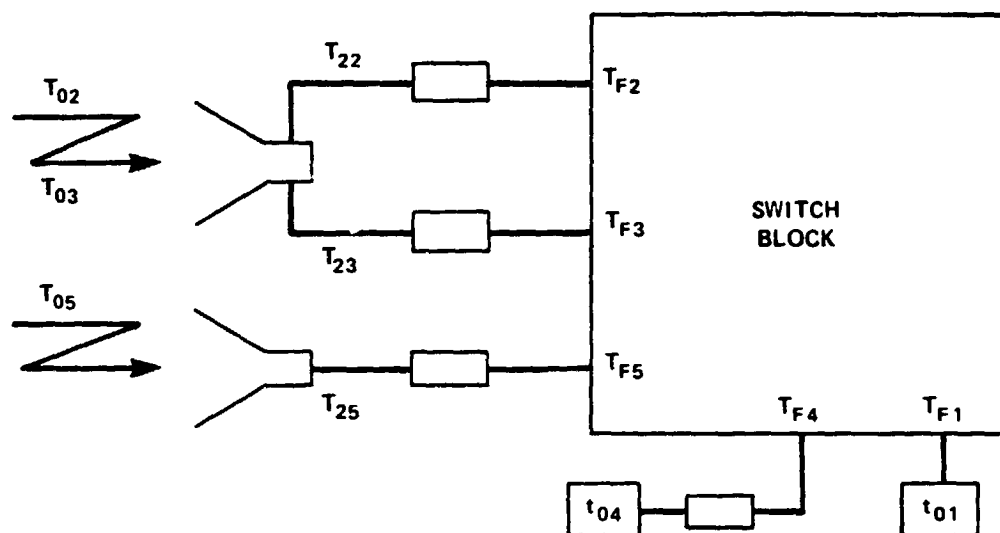


Figure 4-13

$T_{23} \Rightarrow$ see Equation (4.2-8a)

$T_{22} \Rightarrow$ see Equation (4.2-8b)

$T_{25} \Rightarrow$ see Equation (4.2-11)

$T_{F1} \Rightarrow$ see Equation (4.2-3)

$T_{F2} \Rightarrow$ see Equation (4.2-9)

$T_{F3} \Rightarrow$ see Equation (4.2-10)

$T_{F4} \Rightarrow$ see Equation (4.2-6)

$$T_{F5} = T_{25}\alpha_{55} + E_{55}t_{55} \quad (4.2-14)$$

4.3 Losses Internal to the Switch Block

Two different switch block configurations occur in the various SMMR simulator radiometers. The switch blocks consist of a cascade of ferrite circulator junctions. The 6.6, 10.7, 21, and 21 GHz uplook radiometers use a cascade of three junctions, while the 18 and 37 GHz radiometers have a four junction cascade. A set of equations is derived for each switch block configuration.

For purposes of this analysis the following terms are defined:

1. $T_{Fi} \equiv$ effective radiometric temperature at the input to the switch block
2. $T_{Ri} \equiv$ effective radiometric temperature at the output of the switch block
3. $\alpha_{jk} \equiv$ transmissivity of the junction
4. $E_{jk} \equiv$ emissivity of the junction
5. $\beta_{jk} \equiv$ isolation of the junction

where $i = 1 =$ warm calibration load

2 = vertical polarization of incident radiation

3 = horizontal polarization of incident radiation

4 = cold calibration load

5 = uplooking channel

$j \equiv$ switch number

$k = 1 \equiv$ schematic switch position representation of CW circulation

2 \equiv schematic switch position representation of CCW circulation

The analysis of the switch block takes two approaches. The first approach considers every circulator junction individually using the terms previously defined. The second approach considers only those parameters physically measurable. This is required since some circulator junction

ports are internal of the switch block and thus inaccessible. The final results of the two approaches are equivalent.

To facilitate the second approach additional terms are defined:

1. $A_{MN} \equiv$ measurable path loss
2. $B_{MN} \equiv$ measurable path isolation
3. $\epsilon_N \equiv$ switch block emissivity

where $M \equiv$ input (i) contributing the signal

$N \equiv$ switch setting for primary input signal path

4.3.1 Switch Block 6.6, 10.7, 21, 21 Uplook

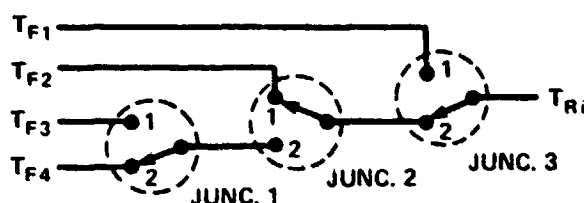


Figure 4-14. Schematic Representation Switch Block 6.6, 10.7, 21, 21 GHz Uplook

Analysis of the switch block for the 6.6, 10.7, 21, and 21 GHz uplook radiometers (Figure 4-14) in each of the four measurement configurations (T_{R1} , T_{R2} , T_{R3} , T_{R4}) yields the set of equations given below in matrix notation where $t_0 \equiv$ physical temperature of the switch block.

$$\begin{bmatrix} T_{R1} \\ T_{R2} \\ T_{R3} \\ T_{R4} \end{bmatrix} = \begin{bmatrix} \alpha_{31} & \rho_{22}\rho_{31} & \rho_{12}\alpha_{22}\rho_{31} & \alpha_{12}\alpha_{22}\rho_{31} \\ \rho_{32} & \alpha_{21}\alpha_{32} & \rho_{12}\rho_{21}\alpha_{32} & \alpha_{12}\rho_{21}\alpha_{32} \\ \rho_{32} & \rho_{22}\alpha_{32} & \alpha_{11}\alpha_{22}\alpha_{32} & \rho_{11}\alpha_{22}\alpha_{32} \\ \rho_{32} & \rho_{22}\alpha_{32} & \rho_{12}\alpha_{22}\alpha_{32} & \alpha_{12}\alpha_{22}\alpha_{32} \end{bmatrix} \begin{bmatrix} T_{F1} \\ T_{F2} \\ T_{F3} \\ T_{F4} \end{bmatrix} + \begin{bmatrix} E_{12}\alpha_{22}\rho_{31} + E_{22}\rho_{31} + E_{31} \\ E_{12}\rho_{21}\alpha_{32} + E_{21}\alpha_{32} + E_{32} \\ E_{11}\alpha_{22}\alpha_{32} + E_{22}\alpha_{32} + E_{32} \\ E_{12}\alpha_{22}\alpha_{32} + E_{22}\alpha_{32} + E_{32} \end{bmatrix} t_0 \quad (4-M1)$$

The matrix Equation (4-M1) is generated in terms of the individual switch characteristics. Since these are not separately measurable as noted above, the matrix equation is rewritten in terms of measurable quantities.

$$\begin{bmatrix} T_{R1} \\ T_{R2} \\ T_{R3} \\ T_{R4} \end{bmatrix} = \begin{bmatrix} A_{11} & B_{21} & B_{31} & B_{41} \\ B_{12} & A_{22} & B_{32} & B_{42} \\ B_{13} & B_{23} & A_{33} & B_{43} \\ B_{14} & B_{24} & B_{34} & A_{44} \end{bmatrix} \begin{bmatrix} T_{F1} \\ T_{F2} \\ T_{F3} \\ T_{F4} \end{bmatrix} + \begin{bmatrix} \epsilon_1 \\ \epsilon_2 \\ \epsilon_3 \\ \epsilon_4 \end{bmatrix} t_0 \quad (4-M2)$$

The matrices and vectors in Equations (4-M1) and (4-M2) are equivalent term for term. Examination of the switch configurations and the term equivalency equations for (4-M1) and (4-M2), yields the following simplification:

1. $B_{12} = B_{13} = B_{14}$ define as B_1
- and 2. $B_{23} = B_{24}$ define as B_2

Equivalence of the two emissivity vectors yields the following where each effective emissivity is expressed in terms of the measurable characteristics A_{MN} and B_{MN}

$$\epsilon_1 = 1 - A_{11} - B_{21} - B_{31} - B_{41} \quad (4.3-1)$$

$$\epsilon_2 = 1 - A_{22} - B_1 - B_{32} - B_{42} \quad (4.3-2)$$

$$\epsilon_3 = 1 - A_{33} - B_1 - B_2 - B_{43} \quad (4.3-3)$$

$$\epsilon_4 = 1 - A_{44} - B_1 - B_2 - B_{34} \quad (4.3-4)$$

The final form of the switch block loss equation for the 6.6, 10.7 and 21 and 21GHz uplook radiometer systems can thus be written as follows:

$$\begin{bmatrix} T_{R1} \\ T_{R2} \\ T_{R3} \\ T_{R4} \end{bmatrix} = \begin{bmatrix} A_{11} & B_{21} & B_{31} & B_{41} \\ B_1 & A_{22} & B_{32} & B_{42} \\ B_1 & B_2 & A_{33} & B_{43} \\ B_1 & B_2 & B_{34} & A_{44} \end{bmatrix} \begin{bmatrix} T_{F1} \\ T_{F2} \\ T_{F3} \\ T_{F4} \end{bmatrix} + \begin{bmatrix} 1 - A_{11} - B_{21} - B_{31} - B_{41} \\ 1 - B_1 - A_{22} - B_{32} - B_{42} \\ 1 - B_1 - B_2 - A_{33} - B_{43} \\ 1 - B_1 - B_2 - B_{34} - A_{44} \end{bmatrix} t_0 \quad (4-M3)$$

4.3.2 Switch Block 18 and 37GHz

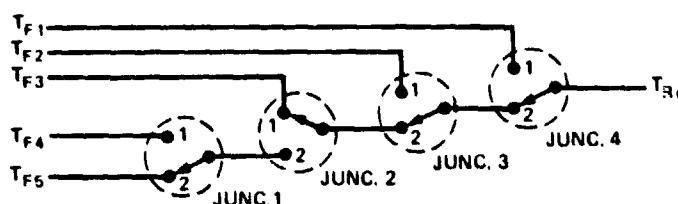


Figure 4-15. Schematic Representation Switch Block for 18 and 37GHz

Analysis of the switch block for the 18 and 37 GHz radiometer systems, Figure 4-15, gives the equation set (4-M4) shown below, in terms of the individual switch characteristics.

$$\begin{bmatrix} T_{R1} \\ T_{R2} \\ T_{R3} \\ T_{R4} \\ T_{R5} \end{bmatrix} = \begin{bmatrix} \alpha_{41} & \beta_{32}\beta_{41} & \beta_{22}\alpha_{32}\beta_{41} & \alpha_{11}\alpha_{22}\alpha_{32}\beta_{41} & \beta_{11}\alpha_{22}\alpha_{32}\beta_{41} \\ \beta_{42} & \alpha_{31}\alpha_{42} & \beta_{22}\beta_{31}\alpha_{42} & \alpha_{11}\alpha_{22}\beta_{31}\alpha_{42} & \beta_{11}\alpha_{22}\beta_{31}\alpha_{42} \\ \beta_{42} & \beta_{32}\alpha_{42} & \alpha_{21}\alpha_{32}\alpha_{42} & \alpha_{11}\beta_{21}\alpha_{32}\alpha_{42} & \beta_{11}\beta_{21}\alpha_{32}\alpha_{42} \\ \beta_{42} & \beta_{32}\alpha_{42} & \beta_{22}\alpha_{32}\alpha_{42} & \alpha_{11}\alpha_{22}\alpha_{32}\alpha_{42} & \beta_{11}\alpha_{22}\alpha_{32}\alpha_{42} \\ \beta_{42} & \beta_{32}\alpha_{42} & \beta_{22}\alpha_{32}\alpha_{42} & \beta_{12}\alpha_{22}\alpha_{32}\alpha_{42} & \alpha_{12}\alpha_{22}\alpha_{32}\alpha_{42} \end{bmatrix} \begin{bmatrix} T_{F1} \\ T_{F2} \\ T_{F3} \\ T_{F4} \\ T_{F5} \end{bmatrix} + \begin{bmatrix} E_{11}\alpha_{22}\alpha_{32}\beta_{41} + E_{22}\alpha_{32}\beta_{41} + E_{32}\beta_{41} + E_{41} \\ E_{11}\alpha_{22}\beta_{31}\alpha_{42} + E_{22}\beta_{31}\alpha_{42} + E_{31}\alpha_{42} + E_{42} \\ E_{11}\beta_{21}\alpha_{32}\alpha_{42} + E_{21}\alpha_{32}\alpha_{42} + E_{32}\alpha_{42} + E_{42} \\ E_{11}\alpha_{22}\alpha_{32}\alpha_{42} + E_{22}\alpha_{32}\alpha_{42} + E_{32}\alpha_{42} + E_{42} \\ E_{11}\alpha_{22}\alpha_{32}\alpha_{42} + E_{22}\alpha_{32}\alpha_{42} + E_{32}\alpha_{42} + E_{42} \end{bmatrix} t_0 \quad (4-M4)$$

When rewritten in terms of physically measurable switch block characteristics, the equation set becomes

$$\begin{bmatrix} T_{R1} \\ T_{R2} \\ T_{R3} \\ T_{R4} \\ T_{R5} \end{bmatrix} = \begin{bmatrix} A_{11} & B_{21} & B_{31} & B_{41} & B_{51} \\ B_{12} & A_{22} & B_{32} & B_{42} & B_{52} \\ B_{13} & B_{23} & A_{33} & B_{43} & B_{53} \\ B_{14} & B_{24} & B_{34} & A_{44} & B_{54} \\ B_{15} & B_{25} & B_{35} & B_{45} & A_{55} \end{bmatrix} \begin{bmatrix} T_{F1} \\ T_{F2} \\ T_{F3} \\ T_{F4} \\ T_{F5} \end{bmatrix} + \begin{bmatrix} \epsilon_1 \\ \epsilon_2 \\ \epsilon_3 \\ \epsilon_4 \\ \epsilon_5 \end{bmatrix} \quad (4-M5)$$

Examination of the term equivalency equations shows that

$$B_{12} = B_{13} = B_{14} = B_{15} \quad \text{define as } B_1$$

$$B_{23} = B_{24} = B_{25} \quad \text{define as } B_2$$

$$\text{and } B_{34} = B_{35} \quad \text{define as } B_3$$

The final form of the switch-loss equation for the 18 and 37 GHz radiometers in terms of measurable quantities is Equation (4-M6):

$$\begin{bmatrix} T_{R1} \\ T_{R2} \\ T_{R3} \\ T_{R4} \\ T_{R5} \end{bmatrix} = \begin{bmatrix} A_{11} & B_1 & B_1 & B_1 & B_1 \\ B_1 & A_{22} & B_2 & B_2 & B_2 \\ B_1 & B_2 & A_{33} & B_3 & B_3 \\ B_1 & B_2 & B_3 & A_{44} & B_4 \\ B_1 & B_2 & B_3 & B_4 & A_{55} \end{bmatrix} \begin{bmatrix} T_{F1} \\ T_{F2} \\ T_{F3} \\ T_{F4} \\ T_{F5} \end{bmatrix} + \begin{bmatrix} 1 - A_{11} - B_1 - B_1 - B_1 - B_1 \\ 1 - A_{22} - B_1 - B_2 - B_2 - B_2 \\ 1 - B_1 - B_2 - A_{33} - B_3 - B_3 \\ 1 - B_1 - B_2 - B_3 - A_{44} - B_4 \\ 1 - B_1 - B_2 - B_3 - B_4 - A_{55} \end{bmatrix} t_0 \quad (4-M6)$$

4.4 SMMR Simulator Radiometer Equations

In Sections 4.2 and 4.3, sets of equations were developed for each radiometer which describe the effects of thermal losses, switch leakages, and polarization mixings on the different incident signals (scene, warm load, cold load). In this section each set of equations is combined to obtain an expression for the absolute brightness temperature of the incident scene radiation.

4.4.1 Derivation Method

Recall the basic radiometric equation derived in Section 3:

$$T_A = T_w + (T_c - T_w)N \quad (4.4-1)$$

where

$$N = \frac{V_A - V_w}{V_c - V_w} \quad (4.4-2)$$

Three analogous equation sets may be written for the SMMR simulator radiometers:

$$T_{R2} = T_{R1} + (T_{R4} - T_{R1})N_2 \quad (4.4-3a)$$

where

$$N_2 = \frac{V_2 - V_1}{V_4 - V_1} \quad (4.4-3b)$$

$$T_{R3} = T_{R1} + (T_{R4} - T_{R1})N_3 \quad (4.4-4a)$$

where

$$N_3 = \frac{V_3 - V_1}{V_4 - V_1} \quad (4.4-4b)$$

and

$$T_{R5} = T_{R1} - (T_{R4} - T_{R1})N_5 \quad (4.4-5a)$$

where

$$N_5 = \frac{V_5 - V_1}{V_4 - V_1} \quad (4.4-5b)$$

where 1 = warm calibration load

2 = vertical component of signal

3 = horizontal component of signal

4 = cold calibration load

5 = uplooking signal

The incident scene brightness temperatures are obtained by substituting expressions for T_{Ri} derived in Sections 4.2 and 4.3 into Equations (4.4-3a), (4.4-4a) and (4.4-5a). For the 6.6, 10.7, and 21 GHz radiometers, T_{R2} and T_{R3} contain mixtures of the horizontally and vertically polarized incident signals. Thus Equations (4.4-3a) and (4.4-3b) must be solved simultaneously to yield separate expressions for the differently polarized signals T_{02} and T_{03} . For the 37GHz radiometer, mixtures of three states (horizontal, vertical, uplook) are obtained and three equations must be solved simultaneously for T_{02} , T_{03} and T_{05} . The details of these laborious derivations are presented in Reference 42; the results are presented below.

4.4.2 Radiometric Equations

This section tabulates the various radiometric equations for SMMR simulator.

Note: α_{MN} , E_{MN} , and t_{MN} as defined in section 4.2; A_{MN} , B_{MN} , and ϵ_N as defined in section 4.3.

4.4.2.1 6.6 and 10.7GHz Radiometer Systems

$$T_{02} = t_{01} \left[\frac{B_2 C_1 - B_1 C_2}{A_1 B_2 - A_2 B_1} \right] + t_{04} \left[\frac{B_2 D_1 - B_1 D_2}{A_1 B_2 - A_2 B_1} \right] + \left[\frac{B_2 F_1 - B_1 F_2}{A_1 B_2 - A_2 B_1} \right]$$
$$T_{03} = t_{01} \left[\frac{A_1 C_2 - C_1 A_2}{A_1 B_2 - A_2 B_1} \right] + t_{04} \left[\frac{A_1 D_2 - A_2 D_1}{A_1 B_2 - A_2 B_1} \right] + \left[\frac{A_1 E_2 - E_1 A_2}{A_1 B_2 - A_2 B_1} \right]$$

where:

$$A_1 = a_1 \rho_1 \alpha_{12} \alpha_{23} \alpha_{33} \alpha_{43} + b_1 (1 - \rho_2) \alpha_{12} \alpha_{22} \alpha_{32} \alpha_{42}$$

$$A_2 = a_2 \rho_1 \alpha_{12} \alpha_{23} \alpha_{33} \alpha_{43} + b_2 (1 - \rho_2) \alpha_{12} \alpha_{22} \alpha_{32} \alpha_{42}$$

$$B_1 = a_1 (1 - \rho_1) \alpha_{13} \alpha_{23} \alpha_{33} \alpha_{43} + b_1 \rho_2 \alpha_{13} \alpha_{22} \alpha_{32} \alpha_{42}$$

$$B_2 = a_2 (1 - \rho_1) \alpha_{13} \alpha_{23} \alpha_{33} \alpha_{43} + b_2 \rho_2 \alpha_{13} \alpha_{22} \alpha_{32} \alpha_{42}$$

$$C_1 = c_1 + e_1$$

$$C_2 = c_2 + e_2$$

$$D_1 = d_1 \alpha_{60}$$

$$D_2 = d_2 \alpha_{60}$$

$$E_1 = d_1 E_{60} t_{60} - b_1 [E_{32} t_{32} \alpha_{42} + E_{42} t_{42} + E_{22} t_2 \alpha_{32} \alpha_{42} + E_{13} t_1 \rho_2 \alpha_{22} \alpha_{32} \alpha_{42} \\ + E_{12} t_1 (1 - \rho_2) \alpha_{22} \alpha_{32} \alpha_{42}] - a_1 [E_{33} t_{33} \alpha_{43} + E_{43} t_{43} + \alpha_{33} \alpha_{43} E_{23} t_2 \\ + E_{13} t_1 (1 - \rho_1) \alpha_{33} \alpha_{23} \alpha_{43} + E_{12} t_1 \rho_1 \alpha_{23} \alpha_{33} \alpha_{43}]$$

$$E_2 = d_2 E_{60} t_{60} - b_2 [E_{32} t_{32} \alpha_{42} + E_{42} t_{42} + E_{22} t_2 \alpha_{32} \alpha_{42} + E_{13} t_1 \rho_2 \alpha_{22} \alpha_{32} \alpha_{42} \\ + E_{12} t_1 (1 - \rho_2) \alpha_{22} \alpha_{32} \alpha_{42}] - a_2 [E_{33} t_{33} \alpha_{43} + E_{43} t_{43} + \alpha_{33} \alpha_{43} E_{23} t_2 \\ + E_{13} t_1 (1 - \rho_1) \alpha_{33} \alpha_{23} \alpha_{43} + E_{12} t_1 \rho_1 \alpha_{23} \alpha_{33} \alpha_{43}]$$

$$a_1 = A_{33} - B_{31} + N_H (B_{31} - B_{34})$$

$$a_2 = B_{32} - B_{31} + N_V (B_{31} - B_{34})$$

$$b_1 = B_2 - B_{21} + N_H (B_{21} - B_2)$$

$$b_2 = A_{22} - B_{21} + N_V (B_{21} - B_2)$$

$$c_1 = A_{11} - B_1 + N_H (B_1 - A_{11})$$

$$c_2 = A_{11} - B_1 + N_V (B_1 - A_{11})$$

$$d_1 = B_{41} - B_{43} + N_H (A_{44} - B_{41})$$

$$d_2 = B_{41} - B_{42} + N_V (A_{44} - B_{41})$$

$$e_1 = \epsilon_1 - \epsilon_3 + N_H (\epsilon_4 - \epsilon_1)$$

$$e_2 = \epsilon_1 - \epsilon_2 + N_V (\epsilon_4 - \epsilon_1)$$

4.4.2.2 18GHz Radiometers

$$T_{02} = t_{01} \left[\frac{B_2 C_1 - B_1 C_2}{A_1 B_2 - A_2 B_1} \right] + t_{04} \left[\frac{B_2 D_1 - B_1 D_2}{A_1 B_2 - A_2 B_1} \right] + \left[\frac{B_2 E_1 - B_1 E_2}{A_1 B_2 - A_2 B_1} \right]$$

$$T_{03} = t_{01} \left[\frac{A_1 C_2 - A_2 C_1}{A_1 B_2 - A_2 B_1} \right] + t_{04} \left[\frac{A_1 D_2 - A_2 D_1}{A_1 B_2 - A_2 B_1} \right] + \left[\frac{A_1 E_2 - A_2 E_1}{A_1 B_2 - A_2 B_1} \right]$$

where:

$$A_1 = a_1 \rho_1 \alpha_{12} \alpha_{33} \alpha_{43} \alpha_{23} + b_1 (1 - \rho_2) \alpha_{12} \alpha_{22} \alpha_{32} \alpha_{42}$$

$$A_2 = a_2 \rho_1 \alpha_{12} \alpha_{33} \alpha_{43} \alpha_{23} + b_2 (1 - \rho_2) \alpha_{12} \alpha_{22} \alpha_{32} \alpha_{42}$$

$$\begin{aligned} B_1 &= a_1(1 - \rho_1)\alpha_{13}\alpha_{23}\alpha_{33}\alpha_{43} + b_1\rho_2\alpha_{13}\alpha_{22}\alpha_{32}\alpha_{42} \\ B_2 &= a_2(1 - \rho_1)\alpha_{13}\alpha_{23}\alpha_{33}\alpha_{43} + b_2\rho_2\alpha_{13}\alpha_{22}\alpha_{32}\alpha_{42} \end{aligned} \left. \vphantom{\begin{aligned} B_1 \\ B_2 \end{aligned}} \right\} \text{same as 6.6/10.7}$$

$$C_1 = c_1 + e_1 + f_1$$

$$C_2 = c_2 + e_2 + f_2$$

$$D_1 \Rightarrow \text{same as 6.6/10.7}$$

$$D_2 \Rightarrow \text{same as 6.6/10.7}$$

$$E_1 \Rightarrow \text{same as 6.6/10.7}$$

$$E_2 \Rightarrow \text{same as 6.6/10.7}$$

$$a_1 = A_{33} - B_{31} + N_H(B_{31} - B_3)$$

$$e_2 = B_{51} - B_{52} + N_V(B_{54} - B_{51})$$

$$a_2 = B_{32} - B_{31} + N_V(B_{31} - B_3)$$

$$f_1 = \epsilon_1 - \epsilon_3 + N_H(\epsilon_4 - \epsilon_1)$$

$$b_1 = B_2 - B_{21} + N_H(B_{21} - B_2)$$

$$f_2 = \epsilon_1 - \epsilon_2 + N_V(\epsilon_4 - \epsilon_1)$$

$$b_2 = A_{22} - B_{21} + N_V(B_{21} - B_2)$$

$$c_1 = A_{11} - B_{12} + N_H(B_{12} - A_{11})$$

$$c_2 = A_{11} - B_{12} + N_V(B_{12} - A_{11})$$

$$d_1 = B_{41} - B_{43} + N_H(A_{44} - B_{41})$$

$$d_2 = B_{41} - B_{42} + N_V(A_{44} - B_{41})$$

$$e_1 = B_{51} - B_{53} + N_H(B_{54} - B_{51})$$

4.4.2.3 21 GHz Radiometer

$$T_{02} = t_{01} \left[\frac{B_2 C_1 - B_1 C_2}{A_1 B_2 - A_2 B_1} \right] + t_{04} \left[\frac{B_2 D_1 - B_1 D_2}{A_1 B_2 - A_2 B_1} \right] + \left[\frac{B_2 F_1 - B_1 F_2}{A_1 B_2 - A_2 B_1} \right]$$

$$T_{03} = t_{01} \left[\frac{A_1 C_2 - A_2 C_1}{A_1 B_2 - A_2 B_1} \right] + t_{04} \left[\frac{A_1 D_2 - A_2 D_1}{A_1 B_2 - A_2 B_1} \right] + \left[\frac{A_1 F_2 - A_2 F_1}{A_1 B_2 - A_2 B_1} \right]$$

where:

$$A_1 = a_1\rho_1\alpha_{23}\alpha_{53} + b_1(1 - \rho_2)\alpha_{22}\alpha_{52}$$

$$A_2 = a_2\rho_1\alpha_{23}\alpha_{53} + b_2(1 - \rho_2)\alpha_{22}\alpha_{52}$$

$$B_1 = a_1(1 - \rho_1)\alpha_{23}\alpha_{53} + b_1\rho_2\alpha_{22}\alpha_{52}$$

$$B_2 = a_2(1 - \rho_1)\alpha_{23}\alpha_{53} + b_2\rho_2\alpha_{22}\alpha_{52}$$

$$C_1 = c_1 + e_1$$

$$C_2 = c_2 + e_2$$

$$D_1 = \text{same as 6.6/10.7}$$

$$D_2 = \text{same as 6.6/10.7}$$

$$E_1 = d_1 E_{60} t_{60} - b_1 (E_{22} t_2 \alpha_{52} + E_{52} t_{52}) - a_1 (E_{23} t_2 \alpha_{53} + E_{53} t_{53})$$

$$E_2 = d_2 E_{60} t_{60} - b_2 (E_{22} t_2 \alpha_{52} + E_{52} t_{52}) - a_2 (E_{23} t_2 \alpha_{53} + E_{53} t_{53})$$

$$a_1 = A_{33} - B_{31} + N_H(B_{31} - B_{34})$$

$$a_2 = B_{32} - B_{31} + N_V(B_{31} - B_{34})$$

$$b_1 = B_2 - B_{21} + N_H(B_{21} - B_2)$$

$$b_2 = A_{22} - B_{21} + N_V(B_{21} - B_2)$$

$$c_1 = A_{11} - B_1 + N_H(B_1 - A_{11})$$

$$c_2 = A_{11} - B_1 + N_V(B_1 - A_{11})$$

$$d_1 = B_{41} - B_{43} + N_H(A_{44} - B_{41})$$

$$d_2 = B_{41} - B_{42} + N_V(A_{44} - B_{41})$$

$$e_1 = \epsilon_1 - \epsilon_3 + N_H(\epsilon_4 - \epsilon_1)$$

$$e_2 = \epsilon_1 - \epsilon_2 + N_V(\epsilon_4 - \epsilon_1)$$

4.4.2.4 21 GHz Uplook Radiometer

$$T_{05} = A t_{01} + B t_{01} N + C t_{04} + D t_{04} N + E N + F + G + H$$

where:

$$A = \{1 + B_{31} - \epsilon_2 - B_1 B_{32}\} \div 1$$

$$B = \{-1 - B_{31} + \epsilon_4 + B_1 + B_{34}\} \div 1$$

$$C = \{\alpha_{60} [B_{41} - \alpha_{60}]\} \div 1$$

$$D = \{\alpha_{60} [\alpha_{60} - B_{41}]\} \div 1$$

$$E = \{E_{60} t_{60} [B_{41} + A_{44}] + E_{55} t_{55} [B_2 - B_1] + E_{25} t_{25} [B_1 \alpha_{55} \alpha_{25} - B_2 \alpha_{55} \alpha_{25}]\} \div 1$$

$$F = \{E_{60} t_{60} [B_{41} - B_{42}]\} \div 1$$

$$G = \{E_{55} t_{55} [B_{21} - A_{22}] \} \div 1$$

$$H = \{E_{25} t_{25} [\alpha_{25}\alpha_{55}(A_{22} - B_{21})]\} \div 1$$

$$I = [\alpha_{55}A_{22} - (B_{21}\alpha_{55})(1 - N) - B_2\alpha_{55}N]$$

4.4.2.5 37GHz Radiometer

$$\begin{aligned} T_{05} = & \{t_{04}[R_1(Y_2 Z_3 - Y_3 Z_2) - S_1(Y_1 Z_3 - Y_3 Z_1) + U_1(Y_1 Z_2 - Y_2 Z_1)] \\ & + t_{01}[R_2(Y_2 Z_3 - Y_3 Z_2) - S_2(Y_1 Z_3 - Y_3 Z_1) + U_2(Y_1 Z_2 - Y_2 Z_1)] \\ & + [R_3(Y_2 Z_3 - Y_3 Z_2) - S_3(Y_1 Z_3 - Y_3 Z_1) + U_3(Y_1 Z_2 - Y_2 Z_1)]\} \\ & \div [X_1(Y_2 Z_3 - Y_3 Z_2) - X_2(Y_1 Z_3 - Y_3 Z_1) + X_3(Y_1 Z_2 - Y_2 Z_1)] \end{aligned}$$

$$\begin{aligned} T_{03} = & \{t_{04}[X_1(S_1 Z_3 - U_1 Z_2) + X_2(U_1 Z_1 - R_1 Z_3) + X_3(R_1 Z_2 - S_1 Z_1)] \\ & + t_{01}[X_1(S_2 Z_3 - U_2 Z_2) + X_2(U_2 Z_1 - R_2 Z_3) + X_3(R_2 Z_2 - S_2 Z_1)] \\ & + [X_1(S_3 Z_3 - U_3 Z_2) + X_2(U_3 Z_1 - R_3 Z_3) + X_3(R_3 Z_2 - S_3 Z_1)]\} \\ & \div [X_1(Y_2 Z_3 - Y_3 Z_2) - X_2(Y_1 Z_3 - Y_3 Z_1) + X_3(Y_1 Z_2 - Y_2 Z_1)] \end{aligned}$$

$$\begin{aligned} T_{02} = & \{t_{04}[X_1(U_1 Y_2 - S_1 Y_3) + X_2(R_1 Y_3 - U_1 Y_1) + X_3(S_1 Y_1 - R_1 Y_2)] \\ & + t_{01}[X_1(U_2 Y_2 - S_2 Y_3) + X_2(R_2 Y_3 - U_2 Y_1) + X_3(S_2 Y_1 - R_2 Y_2)] \\ & + [X_1(U_3 Y_2 - S_3 Y_3) + X_2(R_3 Y_3 - U_3 Y_1) + X_3(S_3 Y_1 - R_3 Y_2)]\} \\ & \div [X_1(Y_2 Z_3 - Y_3 Z_2) - X_2(Y_1 Z_3 - Y_3 Z_1) + X_3(Y_1 Z_2 - Y_2 Z_1)] \end{aligned}$$

where:

$$R_1 = e_1 - d_1 + N_V(a_1 - e_1)$$

$$X_1 = d_6 - e_5 + N_V(e_5 - a_6)$$

$$R_2 = -d_2 + N_V a_2$$

$$X_2 = C_6 - e_5 + N_H(e_5 - a_6)$$

$$R_3 = -d_5 + e_4 + N_V(-e_4 + a_5)$$

$$X_3 = b_6 - e_5 + N_S(e_5 - a_6)$$

$$S_1 = e_1 - e_1 + N_H(a_1 - e_1)$$

$$Y_1 = d_3 - e_2 + N_V(e_2 - a_3)$$

$$S_2 = -e_2 + N_H a_2$$

$$Y_2 = e_3 - e_2 + N_H(e_2 - a_3)$$

$$S_3 = -e_5 + e_4 + N_H(-e_4 + a_5)$$

$$Y_3 = b_3 - e_2 + N_S(e_2 - a_3)$$

$$U_1 = e_1 - b_1 + N_S(a_1 - e_1)$$

$$Z_1 = d_4 - e_3 + N_V(e_3 - a_4)$$

$$U_2 = -b_2 + N_S a_2$$

$$Z_2 = e_4 - e_3 + N_H(e_3 - a_4)$$

$$U_3 = -b_5 + e_4 + N_S(-e_4 + a_5)$$

$$Z_3 = b_4 - e_3 + N_S(e_3 - a_4)$$

$$a_1 = \alpha_{60} A_{44}$$

$$a_2 = B_{12} + \epsilon_4$$

$$a_3 = (1 - \rho_1) \alpha_{23} \alpha_{53} B_3 + \rho_2 \alpha_{22} \alpha_{52} B_2$$

$$a_4 = \rho_1 \alpha_{23} \alpha_{53} B_3 + (1 - \rho_2) \alpha_{22} \alpha_{52} B_2$$

$$a_5 = E_{60} t_{60} A_{44} + B_{51} (E_{25} t_{25} \alpha_{55} + E_{55} t_{55}) + B_3 (E_{23} t_{23} \alpha_{53} + E_{53} t_{53}) \\ + B_2 (E_{22} t_{22} \alpha_{52} + E_{52} t_{52})$$

$$a_6 = \alpha_{25} \alpha_{55} B_{51}$$

$$b_1 = \alpha_{60} B_{45}$$

$$b_2 = B_1 + \epsilon_5$$

$$b_3 = (1 - \rho_1) \alpha_{23} \alpha_{53} B_3 + \rho_2 \alpha_{22} \alpha_{52} B_2 = a_3$$

$$b_4 = \rho_1 \alpha_{23} \alpha_{53} B_3 + (1 - \rho_2) \alpha_{22} \alpha_{52} B_2 = a_4$$

$$b_5 = E_{60} t_{60} B_{45} + A_{55} (E_{25} t_{25} \alpha_{55} + E_{55} t_{55}) + B_3 (E_{23} t_{23} \alpha_{53} + E_{53} t_{53}) \\ + B_2 (E_{22} t_{22} \alpha_{52} + E_{52} t_{52})$$

$$b_6 = \alpha_{25} \alpha_{55} A_{55}$$

$$c_1 = \alpha_{60} B_{43}$$

$$c_2 = B_1 + \epsilon_3$$

$$c_3 = (1 - \rho_1) \alpha_{23} \alpha_{53} A_{33} + \rho_2 \alpha_{22} \alpha_{52} B_2$$

$$c_4 = \rho_1 \alpha_{23} \alpha_{53} A_{33} + (1 - \rho_2) \alpha_{22} \alpha_{52} B_2$$

$$c_5 = E_{60} t_{60} B_{43} + B_{53} (E_{25} t_{25} \alpha_{55} + E_{55} t_{55}) + A_{33} (E_{23} t_{23} \alpha_{53} + E_{53} t_{53}) \\ + B_2 (E_{22} t_{22} \alpha_{52} + E_{52} t_{52})$$

$$c_6 = \alpha_{25} \alpha_{55} B_{53}$$

$$d_1 = \alpha_{60} B_{42}$$

$$d_2 = B_1 + \epsilon_2$$

$$d_3 = (1 - \rho_1) \alpha_{23} \alpha_{53} B_{32} + \rho_2 \alpha_{22} \alpha_{52} A_{22}$$

$$d_4 = \rho_1 \alpha_{23} \alpha_{53} B_{32} + (1 - \rho_2) \alpha_{22} \alpha_{52} A_{22}$$

$$d_5 = E_{60} t_{60} B_{42} + B_{52} (E_{25} t_{25} \alpha_{55} + E_{55} t_{55}) + B_{32} (E_{23} t_{23} \alpha_{53} + E_{53} t_{53}) \\ + A_{22} (E_{22} t_{22} \alpha_{52} + E_{52} t_{52})$$

$$d_6 = \alpha_{25} \alpha_{55} B_{52}$$

$$e_1 = \alpha_{60} B_{41}, \quad e_2 = B_{21} + e_1$$

$$e_3 = (1 - \rho_1) \alpha_{23} \alpha_{53} B_{31} + \rho_2 \alpha_{22} \alpha_{52} B_{21}$$

$$e_4 = \rho_1 \alpha_{23} \alpha_{53} B_{31} + (1 - \rho_2) \alpha_{22} \alpha_{52} B_{21}$$

$$e_5 = E_{60} t_{60} B_{41} + B_{51} (E_{25} t_{25} \alpha_{55} + E_{55} t_{55}) + B_{31} (E_{23} t_{23} \alpha_{53} + E_{53} t_{53}) \\ + B_{21} (E_{22} t_{22} \alpha_{52} + E_{52} t_{52})$$

$$e_6 = \alpha_{25} \alpha_{55} B_{51}$$

4.4.3 Radiometer Equations -SMMR Simulator--General Form

This section presents the general form of the radiometer equation realized when the questions in Section 4.4.2 are fully expanded. This expansion is undertaken in Reference 42.

6.6/10.7/18/21 GHz Radiometers

$$T = At_w + Bt_w N_H + Ct_w N_V + Dt_L + Et_L N_H + Ft_L N_V \\ + N_H \Sigma G_i E_i t_i + N_V \Sigma H_i E_i t_i + \Sigma I_i E_i t_i$$

21 GHz Uplook

$$T = At_w + Bt_w N + Ct_L + Dt_L N + N \Sigma E_i E_i t_i + \Sigma F_i E_i t_i$$

37 GHz Radiometer

$$T = At_w + Bt_w N_H + Ct_w N_V + Dt_w N_S + Et_L + Ft_L N_H \\ + Gt_2 N_V + Ht_2 N_S + N_H \Sigma I_i E_i t_i + N_V \Sigma J_i E_i t_i \\ + N_S \Sigma K_i E_i t_i + \Sigma L_i E_i t_i$$

5.0 SMMR SIMULATOR ALGORITHM DEVELOPMENT

This section develops the algorithms for reduction of SMMR Simulator data for the 1978 Nimbus-G Underflight Test Series. Two of the seven radiometer systems will not be considered in this effort:

- (1) 18GHz radiometer system: The 18GHz radiometer system developed an oscillation in the receiver electronics during the experiment flight series. At this writing it has proven impossible to extract data information from the oscillatory signal.
- (2) 6.6GHz radiometer system: The horizontal polarization receive antenna for the 6.6GHz radiometer system exhibits an anomolous grating lobe located at approximately 40° right and -30° elevation relative to aircraft. The lobe magnitude approximates 30% of the receive power in the horizontal channel. With the unknown target observed by this lobe at the high receive power in the lobe, data analysis has been deemed impossible. Analysis may be undertaken separate from the present work to reduce the 6.6 vertical channel data.

5.1 Derivation Technique

A typical SMMR Simulator signal path is schematically represented in Figure 5-5-1.

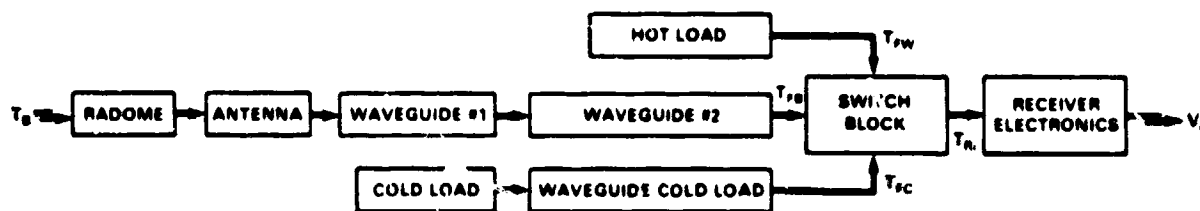


Figure 5-1

Define the following terms:

T_B = received power, incident radiation effective brightness temperature

T_H = effective brightness temperature at switch block input

$i = b$ = antenna signal path

$i = c$ = cold calibration load signal path

$i = w$ = warm calibration load signal path

α_j = transmissivity of external element

j = 4 = radome

3 = antenna

2 = waveguide 1

1 = waveguide 2

$t_j \equiv$ physical temperature of external element

From radiative transfer theory (Section 4) it is seen that:

$$T_{FB} = \alpha_4 \alpha_3 \alpha_2 \alpha_1 T_B + (1 - \alpha_4) \alpha_3 \alpha_2 \alpha_1 t_4 + (1 - \alpha_3) \alpha_2 \alpha_1 t_3 \quad (5.1-1a)$$

$$+ (1 - \alpha_2) \alpha_1 t_2 + (1 - \alpha_1) t_1 \quad (5.1-1b)$$

$$T_{IC} = T_C \alpha_C + (1 - \alpha_C) t_C \quad (5.1-1c)$$

$$T_{FW} = T_W$$

Define:

$$\alpha_0 = \alpha_4 \alpha_3 \alpha_2 \alpha_1 \quad (5.1-2)$$

$$\ell_1 = 1 - \alpha_1 \quad (5.1-3)$$

$$\ell_2 = (1 - \alpha_2) \alpha_1 \quad (5.1-4)$$

$$\ell_3 = (1 - \alpha_3) \alpha_2 \alpha_1 \quad (5.1-5)$$

$$\ell_4 = (1 - \alpha_4) \alpha_3 \alpha_2 \alpha_1 \quad (5.1-6)$$

Then:

$$T_{FB} = \alpha_0 T_B + \ell_1 t_1 + \ell_2 t_2 + \ell_3 t_3 + \ell_4 t_4 \quad (5.1-7)$$

Define two additional terms:

$T_{Ri} \equiv$ effective brightness temperature at receiver electronics input

$V_i \equiv$ receiver electronics output voltage

For the switch block, radiative transfer analysis in Section 4 showed:

$$T_{Ri} = A_i T_{Fi} + (1 - A_i) t_o + L_i \quad (5.1-8)$$

where $A_i \equiv$ switch block transmissivity for measurement channel

$L_i \equiv$ leakage from other channels into measurement channel

Define $\beta_{mn} \equiv$ leakage path transmissivity

m \equiv leakage signal

n \equiv measurement signal

Then:

$$L_B = \beta_{CB} T_{FC} + \beta_{WB} T_{FW} - (\beta_{CB} + \beta_{WB}) t_o \quad (5.1-9)$$

$$L_C = \beta_{BC} T_{FB} + \beta_{WC} T_{FW} - (\beta_{BC} + \beta_{WC}) t_o \quad (5.1-10)$$

$$L_W = \beta_{BW} T_{FB} + \beta_{CW} T_{FC} - (\beta_{BW} + \beta_{CW}) t_o \quad (5.1-11)$$

At this writing, a measurement technique has not been devised to determine values associated with leakage from and/or into the warm load channel. For this algorithm development, it will be assumed all such leakages are negligible, thus $\beta_{mw} = \beta_{wn} = 0$.

Then:

$$L_B = \beta_{CB} T_{FC} - \beta_{CB} t_o \quad (5.1-12)$$

$$L_C = \beta_{BC} T_{FB} - \beta_{BC} t_o \quad (5.1-13)$$

$$L_W = 0 \quad (5.1-14)$$

Recall the basic radiometer response equation

$$V_i = U + G T_{Ri} = U + G (A_i T_{Ri} + (1 - A_i) t_o + L_i) \quad (5.1-15)$$

where U \equiv offset

G \equiv gain

$$V_c = U + G (A_c T_{FC} + (1 - A_c) t_o + L_c) \quad (5.1-16)$$

$$V_w = U + G (A_w T_{FW} + (1 - A_w) t_o + L_w) \quad (5.1-17)$$

note $t_o = T_{FW}$

$$V_c - V_w = G (A_c T_{FC} - A_w T_{FW} + L_c - L_w) \quad (5.1-18)$$

therefore

$$G = (V_c - V_w) / (A_c T_{FC} - A_w T_{FW} + L_c - L_w) \quad (5.1-19)$$

from equation 5.1-15

$$T_{Ri} = \frac{V_i - U}{G} \quad (5.1-20)$$

Equating (5.1-8) and (5.1-20) and substituting (5.1-19) yields

$$T_{FI} = T_{FN} - \left[T_{FW} - T_{FC} - \frac{L_c - L_w}{A_c} \right] \alpha_{Ri} N_i - \frac{L_i + L_w}{A_i} \quad (5.1-21)$$

where

$$N_i = \frac{V_i - V_w}{V_c - V_w} \quad (5.1-22)$$

and

$$\alpha_{Ri} = A_c/A_i \quad (5.1-23)$$

Note $t_o \equiv T_{FW}$ and substitute equations (5.1-12, 13, 14) into equation (5.1-21)

$$T_{FB} = T_{FW} + \left[T_{FC} - T_{FW} + \frac{\beta_{BC}}{A_c} (T_{FB} - T_{FW}) \right] \alpha_{RB} N_B - \frac{\beta_{CB}}{A_B} (T_{FC} - T_{FW}) \quad (5.1-24)$$

Define a term:

$$\mathcal{L}_{mn} \equiv \frac{\beta_{mn}}{A_n} \text{ as the switch block leakage ratio(s):}$$

Then

$$T_{AB} = T_{FW} + [T_{FC} - T_{FW} + \mathcal{L}_{BC} (T_{FB} - T_{FW})] \alpha_{RB} N_B - \mathcal{L}_{CB} (T_{FC} - T_{FW}) \quad (5.1-25)$$

Rearranging terms

$$T_{FB} = \frac{T_{FW} + [T_{FC} - T_{FW} (1 + \mathcal{L}_{BC})] \alpha_{RB} N_B - \mathcal{L}_{CB} (T_{FC} - T_{FW})}{1 - \mathcal{L}_{BC} \alpha_{RB} N_B} \quad (5.1-26)$$

Equating equations (5.1-26) and (5.1-7) and rearranging terms we arrive at the algorithm equation solution for the incident radiation effective brightness temperature:

$$T_B = \frac{1}{\alpha_o} \left\{ \frac{T_{FW} + [T_{FC} - T_{FW} (1 - \mathcal{L}_{BC})] \alpha_{RB} N_B - \mathcal{L}_{CB} (T_{FC} - T_{FW})}{1 - \mathcal{L}_{BC} \alpha_{RB} N_B} - \mathcal{L}_1 t_1 - \mathcal{L}_2 t_2 - \mathcal{L}_3 t_3 - \mathcal{L}_4 t_4 \right\} \quad (5.1-27)$$

5.2 SMMR Simulator System Algorithms

This section presents the SMMR Simulator system algorithms for the 10.7GHz, 21GHz Uplook, 37GHz, and 37GHz uplook radiometers. The equations are left as two independent sets.

derived as in Section 5.1, for the external loss elements and the switch block leakage paths. These equations are analogous to equations (5.1-7) and (5.1-26).

(Note: For the algorithm development undertaken, antenna polarization cross talk is assumed to be negligible and is therefore not included at this writing.)

5.2.1 10.7GHz Radiometer System

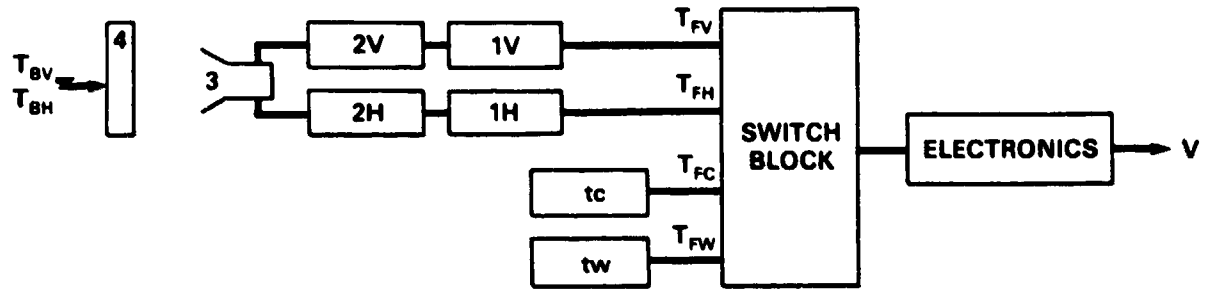


Figure 5-2

$$T_{FH} = T_{BH} \alpha_{0H} + \ell_{1H} t_{1H} + \ell_{2H} t_{2H} + \ell_{3H} t_3 + \ell_{4H} t_4 \quad (5.2-1)$$

$$T_{FV} = T_{BV} \alpha_{0V} + \ell_{1V} t_{1V} + \ell_{2V} t_{2V} + \ell_{3V} t_3 + \ell_{4V} t_4 \quad (5.2-2)$$

$$T_{FC} = t_c \quad (5.2-3)$$

$$T_{FW} = t_w \quad (5.2-4)$$

$$\begin{bmatrix} T_{FH} \\ T_{FV} \end{bmatrix} = \begin{bmatrix} 1 - \alpha_{RH} \ell_{HC} N_H & \ell_{VH} - \alpha_{RH} \ell_{VC} N_H \\ \ell_{HV} - \alpha_{RV} \ell_{HC} N_V & 1 - \alpha_{RV} \ell_{VC} N_V \end{bmatrix}^{-1} \quad (5.2-5)$$

$$\times \begin{bmatrix} t_w(1 + \ell_{CH} + \ell_{VH}) - \ell_{CH} t_c - \alpha_{RH} N_H \{ t_w(1 + \ell_{HC} + \ell_{VC}) - t_c \} \\ t_w(1 + \ell_{CV} + \ell_{HV}) - \ell_{CV} t_c - \alpha_{RV} N_V \{ t_w(1 + \ell_{HC} + \ell_{VC}) - t_c \} \end{bmatrix}$$

where

$$N_H = \frac{V_H - V_w}{V_c - V_w} \quad (5.2-6)$$

and

$$N_V = \frac{V_V - V_w}{V_c - V_w} \quad (5.2-7)$$

Solution for incident brightness temperatures equates (5.2-1), (5.2-2) and (5.2-5).

5.2.2 21GHz Radiometer System

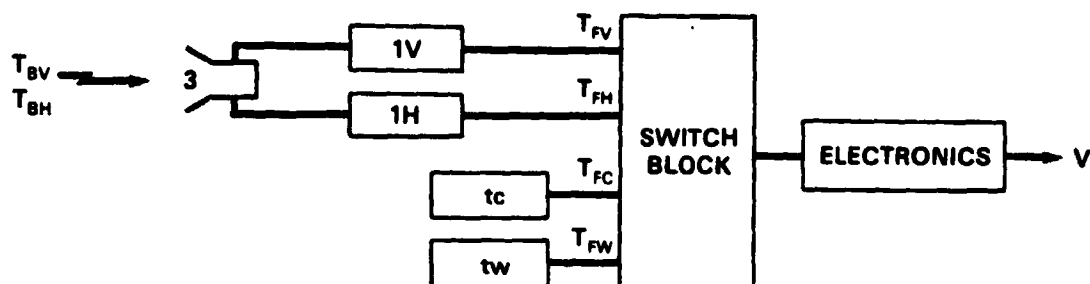


Figure 5-3

$$T_{FH} = T_{BH} \alpha_{0H} + \ell_{3H} t_3 + \ell_{1H} t_{1H} \quad (5.2-8)$$

$$T_{FV} = T_{BV} \alpha_{0V} + \ell_{3V} t_3 + \ell_{1V} t_{1V} \quad (5.2-9)$$

$$T_{FC} = t_c \quad (5.2-10)$$

$$T_{FW} = t_w \quad (5.2-11)$$

$$\begin{bmatrix} T_{FH} \\ T_{FV} \end{bmatrix} = \begin{bmatrix} 1 - \alpha_{RH} \ell_{HC} N_H & \ell_{VH} - \alpha_{RH} \ell_{VC} N_H \\ \ell_{HV} - \alpha_{RV} \ell_{HC} N_V & 1 - \alpha_{RV} \ell_{VC} N_V \end{bmatrix}^{-1} \times \begin{bmatrix} t_w(1 + \ell_{CH} + \ell_{VH}) - \ell_{CH} t_c - \alpha_{RH} N_H \{t_w(1 + \ell_{HC} + \ell_{VC}) - t_c\} \\ t_w(1 + \ell_{CV} + \ell_{HV}) - \ell_{CV} t_c - \alpha_{RV} N_V \{t_w(1 + \ell_{HC} + \ell_{VC}) - t_c\} \end{bmatrix} \quad (5.2-12)$$

Solution for incident brightness temperatures equates (5.2-8), (5.2-9), and (5.2-12).

5.2.3 21GHz Uplooking Radiometer System

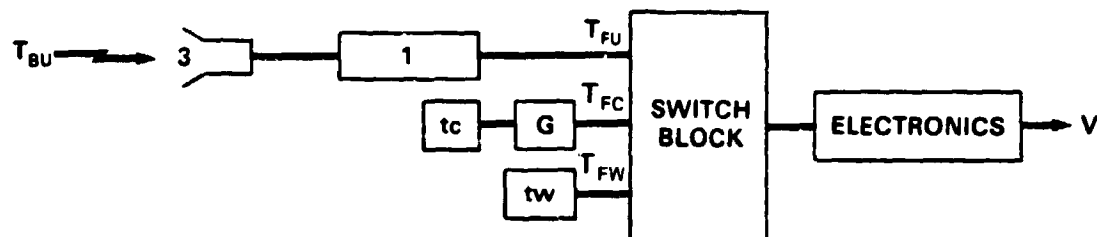


Figure 5-4

$$T_{FU} = T_{BU} \alpha_0 + \ell_3 t_3 + \ell_1 t_1 \quad (5.2-13)$$

$$T_{FC} = t_c \alpha_c + (1 - \alpha_c) t_G \quad (5.2-14)$$

$$T_{FW} = t_w \quad (5.2-15)$$

$$T_{FU} = (1 - \alpha_R \mathcal{L}_{UC} N) [t_w(1 + \mathcal{L}_{CU}) - \mathcal{L}_{CU} T_{FC} - \alpha_R N \{t_w(1 + \mathcal{L}_{UC}) - T_{FC}\}] \quad (5.2-16)$$

Solution for incident brightness temperature equates (5.2-13) and (5.2-16).

5.2.4 37GHz and 37GHz Uplook Radiometer Systems

In-as-much-as the 37GHz and 37GHz uplook radiometer systems share a common switch block and electronics, these systems are treated as a single unit.

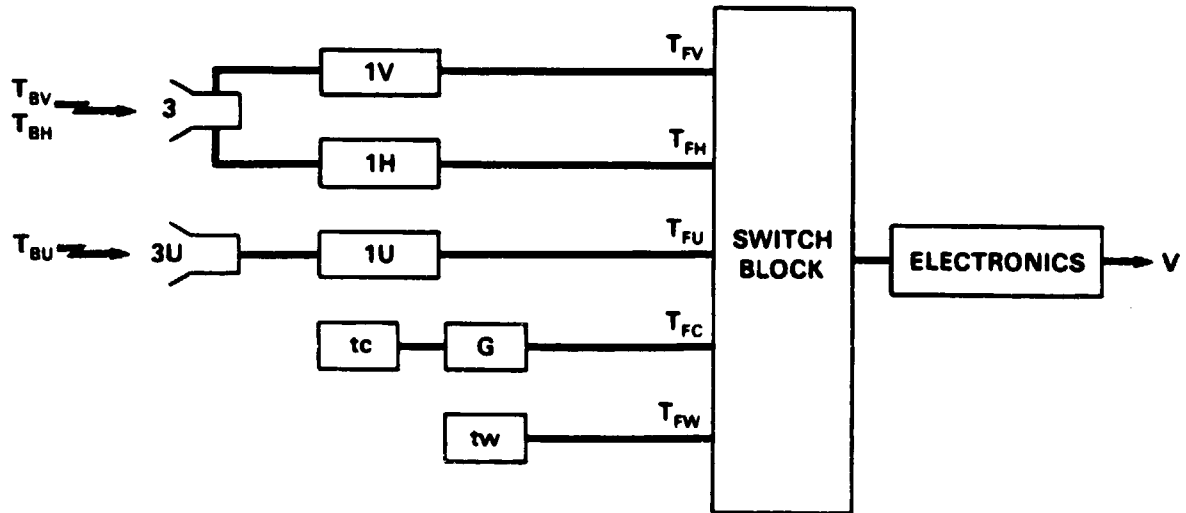


Figure 5-5

$$T_{FH} = T_{BH} \alpha_{0H} + \ell_{3H} t_3 + \ell_{1H} t_{1H} \quad (5.2-17)$$

$$T_{FV} = T_{BV} \alpha_{0V} + \ell_{3V} t_3 + \ell_{1V} t_{1V} \quad (5.2-18)$$

$$T_{FU} = T_{BU} \alpha_{0U} + \ell_{3U} t_{3U} + \ell_{1U} t_{1U} \quad (5.2-19)$$

$$T_{FC} = t_c \alpha_G + (1 - \alpha_G) t_G \quad (5.2-20)$$

$$T_{FW} = t_w \quad (5.2-21)$$

$$\begin{bmatrix} T_{IH} \\ T_{IV} \\ T_{IU} \end{bmatrix} = \begin{bmatrix} A \end{bmatrix}^{-1} \begin{bmatrix} B \end{bmatrix} \quad (5.2-22)$$

$$\begin{bmatrix} A \end{bmatrix} = \begin{bmatrix} (1 - \alpha_{RH} \mathcal{L}_{HC} N_H) & (\mathcal{L}_{VH} - \alpha_{RH} \mathcal{L}_{VC} N_H) & (\mathcal{L}_{UH} - \alpha_{RH} \mathcal{L}_{UC} N_H) \\ (\mathcal{L}_{HV} - \alpha_{RV} \mathcal{L}_{HC} N_V) & (1 - \alpha_{RV} \mathcal{L}_{VC} N_V) & (\mathcal{L}_{UV} - \alpha_{RV} \mathcal{L}_{UC} N_V) \\ (\mathcal{L}_{HU} - \alpha_{RU} \mathcal{L}_{HC} N_U) & (\mathcal{L}_{VU} - \alpha_{RU} \mathcal{L}_{VC} N_U) & (1 - \alpha_{RU} \mathcal{L}_{UC} N_U) \end{bmatrix} \quad (5.2-23)$$

$$\begin{bmatrix} B \end{bmatrix} = \begin{bmatrix} t_w(1 + \mathcal{L}_{CH} + \mathcal{L}_{VH} + \mathcal{L}_{UH}) - \mathcal{L}_{CH} T_{FC} \\ t_w(1 + \mathcal{L}_{CV} + \mathcal{L}_{HV} + \mathcal{L}_{UV}) - \mathcal{L}_{CV} T_{FC} \\ t_w(1 + \mathcal{L}_{CU} + \mathcal{L}_{HU} + \mathcal{L}_{VU}) - \mathcal{L}_{CU} T_{FC} \\ - \alpha_{RH} N_H(t_w[1 + \mathcal{L}_{HC} + \mathcal{L}_{VC} + \mathcal{L}_{UC}] - T_{FC}) \\ - \alpha_{RV} N_V(t_w[1 + \mathcal{L}_{HC} + \mathcal{L}_{VC} + \mathcal{L}_{UC}] - T_{FC}) \\ - \alpha_{RU} N_U(t_w[1 + \mathcal{L}_{HC} + \mathcal{L}_{VC} + \mathcal{L}_{UC}] - T_{FC}) \end{bmatrix} \quad (5.2-24)$$

Solution for incident brightness temperatures equates (5.2-17), (5.2-18), (5.2-19) and (5.2-22).

5.3 SMMR Simulator Algorithm Coefficient Values

Table 5-1 is a summary of the external coefficient values required to solve the algorithm equation sets presented in Section 5.2. Sections 7 and 8 will detail the determination of these coefficient values.

Table 5-1

External Loss Coefficient	10.7		21			37		
	H	V	H	V	UP	H	V	UP
α_R	0.94	0.94	0.90	0.90	0.96	0.97	0.95	0.95
α_0	0.65	0.76	0.77	0.76	0.59	0.54	0.74	0.49
ϵ_1	0.03	0.03	0.12	0.08	0.13	0.07	0.11	0.18
ϵ_2	0.03	0.06	N/A	N/A	N/A	N/A	N/A	N/A
ϵ_3	0.15	0.09	0.11	0.16	0.28	0.39	0.15	0.33
ϵ_4	0.14	0.06	N/A	N/A	N/A	N/A	N/A	N/A
ϵ_c	N/A	N/A	N/A	N/A	0.88	0.82	0.82	0.82

Table 5-2
Leakage Ratio x 100

Leakage Coefficient	10.7	21	21UP	37	37UP
L_{VH}	0.354	0.000	N/A	0.165	N/A
L_{CH}	3.100	0.588	N/A	3.554	N/A
L_{UH}	N/A	N/A	N/A	N/A	0.165
L_{HV}	0.371	0.091	N/A	0.146	N/A
L_{CV}	1.206	2.366	N/A	0.512	N/A
L_{UV}	N/A	N/A	N/A	N/A	0.146
L_{HC}	0.918	0.710	N/A	0.880	N/A
L_{VC}	0.184	0.850	N/A	1.110	N/A
L_{UC}	N/A	N/A	0.809	N/A	2.840
L_{HU}	N/A	N/A	N/A	N/A	0.091
L_{VU}	N/A	N/A	N/A	N/A	0.274
L_{CU}	N/A	N/A	2.635	N/A	0.183

6.0 EFFECTS OF COMPONENT MISMATCH ON THE OPERATION CHARACTERISTICS OF A RADIOMETER SYSTEM

All equations and derivations in the previous sections of this document assume a negligible component mismatch ($VSWR \approx 1$). This section will investigate the effect of component mismatch on the operation characteristics previously discussed.

It is noted at the outset that any numerical analysis attempted will provide an inexact solution in-as-much-as only the magnitude of the mismatch effect ($VSWR$) can be calculated. Any phase relationships causing variation in the radiometer system operation characteristics must be determined empirically.

6.1 First Order VSWR Effect

The principle effect of the antenna $VSWR$ is a reduction in the power transmitted to the rest of the radiometric system. There is a partial reflection of the incident signal at the

antenna/radiometer interface, which may be characterized by a power reflection coefficient R and a transmittance θ , such that $\theta = 1 - R$. When an incident signal of brightness temperature T_B falls on the antenna, a fraction θT_B is transmitted to the radiometric system while the fraction RT_B is reflected back into space (assuming no thermal losses within the antenna). The reflection coefficient is related to the measured VSWR V_o by

$$|R| = \frac{VSWR - 1}{VSWR + 1} \quad (6.1-1)$$

When an ideal lossless radiometer is calibrated according to the standard form, θ is assumed to be unity. As shown previously, the standard calibration equation and calibration constants A and B are given by

$$T_B = A - BN \quad (6.1-2a)$$

$$A = \frac{W^0 N_c}{N_c - N_w} - \frac{C^0 N_w}{N_c - N_w} \quad (6.1-2b)$$

and

$$B = \frac{W^0 - C^0}{N_c - N_w} \quad (6.1-2c)$$

where N is a normalized output voltage, W^0 is a known warm-temperature reference load yielding a normalized output voltage N_w , and C^0 is a known cold-temperature source yielding a normalized output voltage N_c .

Assume the 1st order antenna VSWR effect is included in the calibration procedure. When the hot load at temperature W^0 is observed the system "sees" $T_{\text{Beff}} = \theta W^0$. Similarly the system sees $T_{\text{Beff}} = \theta C^0$ when the cold load is observed. The revised calibration equations become:

$$T_B^{\text{VSWR}\theta} = a - bN \quad (6.1-3a)$$

$$W^0\theta = a - bN_w \quad (6.1-3b)$$

and

$$C^0\theta = a - bN_c \quad (6.1-3c)$$

with the new calibration constant a and b now defined as:

$$a = \theta \frac{(W^0 N_c - C^0 N_w)}{(N_c - N_w)} = \theta A \quad (6.1-4a)$$

$$b = \theta \frac{(W^0 - C^0)}{N_c - N_w} = \theta B \quad (6.1-4b)$$

Although the interpretation of the calibration constants is somewhat changed from the standard case, the predicted brightness temperatures, T_B and T_{Beff} , are identical because of the linearity of the radiometer. This is seen if we consider a general observation with normalized output voltage N . The formulation including the effect of VSWR's (Equations (6.1-3) and (6.1-4) yields:

$$T_B^{\text{VSWR}\theta} = a - bN = \theta A - \theta BN \quad (6.1-5)$$

or

$$T_B^{\text{VSWR}\theta} = a - bN = A - BN$$

which is identical to the case (Equation (6.1-2a)) when VSWRs were not explicitly included. Only the physical interpretation of the calibration constants (a , b , A , and B) is different in two cases. The same predicted brightness temperatures result from any observation.

6.2 Second Order VSWR Effect

When external thermal losses are present (e.g., waveguide, radome and antenna losses), the VSWR's have a more subtle effect, since they affect the values of these losses which are radiometrically determined.

A typical SMMR simulator radiometer system is schematically represented in Figure 6-1. That component which contributes an appreciable mismatch into the radiometer system is the antenna. Transmission line theory shows that the antenna VSWR, as determined at the antenna output, will be reduced when measured at the output of the waveguide section connecting the antenna to the ferrite switch assembly.

Define S_A = Antenna VSWR at the antenna output

S_G = VSWR of the antenna at the waveguide output

L = insertion loss in dB through the waveguide



Figure 6-1

The following relationship can be expressed for the effective VSWR:

$$\text{COTH}^{-1} S_G = \text{COTH}^{-1} S_A + L/8.686 \quad (6.2-1)$$

The VSWR of the antenna/waveguide component will cause a change in the operation characteristics (VSWR, isolation, insertion loss) of the ferrite switch assembly. Define the following additional terms:

S_F = ferrite switch input VSWR

S_{FE} = effective ferrite switch VSWR

L_A = insertion loss of antenna/waveguide

L_F = insertion loss of ferrite switch

L_S = system insertion loss

The following relations hold:

$$S_{FE} = \frac{S_F^2 S_G + S_I}{S_F + S_G} \quad (6.2-2)$$

and

$$L_S = L_A + L_F + 20 \log_{10} (1 \pm |\Gamma_G \Gamma_{FE}|) \quad (6.2-3)$$

where

$$|\Gamma_G| = \frac{S_G - 1}{S_G + 1} \quad \text{and} \quad |\Gamma_{FE}| = \frac{S_{FE} - 1}{S_{FE} + 1} \quad (6.2-4)$$

Define L_{FE} as an effective ferrite switch insertion loss where

$$L_{FE} = L_1 + 20 \log_{10} (1 \pm |\Gamma_G \Gamma_{FE}|) \quad (6.2-5)$$

The effective ferrite switch isolation may be determined from Table 6-1 using the value S_{FE} calculated in Equation (6.2-2).

Recall the ferrite switch junction in the SMMR Simulator radiometer systems is a three port circulator (Figure 6-2). When the ferrite is biased for clockwise circulation, any input signal at port 1 travels to port 2, signal at port 2 travels to port 3, and signal at port 3 travels to port 1. The ferrite's magnetic field does not entirely cut off counterclockwise signal travel. Therefore, a portion of the input signal at port 2 reaches port 1, at port 1 reaches port 3, and at port 3 reaches port 2. The direct (clockwise) path transmissivity is defined as α while the indirect (counterclockwise) path isolation transmissivity is defined as β . Therefore, the outputs at each port will be

$$OUT_1 = IN_3\alpha + IN_2\beta \quad (6.2-6a)$$

$$OUT_2 = IN_1\alpha + IN_3\beta \quad (6.2-6b)$$

$$OUT_3 = IN_2\alpha + IN_1\beta \quad (6.2-6c)$$

A similar equation set may be developed when the ferrite is biased to provide counterclockwise direct path circulation.

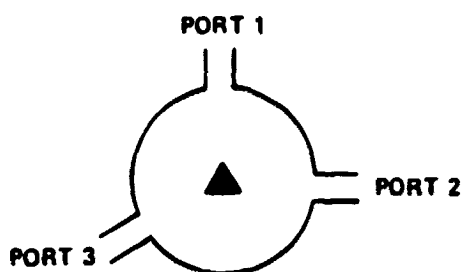


Figure 6-2

Table 6-1
Ferrite Junction VSWR-Isolation (Approximate)

VSWR	ISOL	VSWR	ISOL	VSWR	ISOL	VSWR	ISOL
1.001	66.025	1.051	32.088	1.102	26.281	1.210	20.443
1.002	60.009	1.052	31.923	1.104	26.120	1.220	20.079
1.003	56.491	1.053	31.762	1.106	25.963	1.230	19.732
1.004	53.997	1.054	31.604	1.108	25.809	1.240	19.401
1.005	52.063	1.055	31.449	1.110	25.658	1.250	19.085
1.006	50.484	1.056	31.297	1.112	25.510	1.260	18.783
1.007	49.149	1.057	31.147	1.114	25.364	1.270	18.493
1.008	47.993	1.058	31.000	1.116	25.221	1.280	18.216
1.009	46.975	1.059	30.865	1.118	25.081	1.290	17.949
1.010	46.064	1.060	30.714	1.120	24.943	1.300	17.692
1.011	45.240	1.061	30.575	1.122	24.808	1.310	17.445
1.012	44.489	1.062	30.438	1.124	24.675	1.320	17.207
1.013	43.798	1.063	30.303	1.126	24.544	1.330	16.977
1.014	43.159	1.064	30.171	1.128	24.415	1.340	16.755
1.015	42.564	1.065	30.040	1.130	24.289	1.350	16.540
1.016	42.007	1.066	29.912	1.132	24.164	1.360	16.332
1.017	41.485	1.067	29.785	1.134	24.042	1.370	16.131
1.018	40.993	1.068	29.661	1.136	23.921	1.380	15.936
1.019	40.528	1.069	29.538	1.138	23.803	1.390	15.747
1.020	40.086	1.070	29.417	1.140	23.686	1.400	15.563
1.021	39.667	1.071	29.298	1.142	23.571	1.410	15.385
1.022	39.267	1.072	29.181	1.144	23.457	1.420	15.211
1.023	38.885	1.073	29.066	1.146	23.346	1.430	15.043
1.024	38.520	1.074	28.952	1.148	23.235	1.440	14.879
1.025	38.170	1.075	28.839	1.150	23.127	1.450	14.719
1.026	37.833	1.076	28.728	1.152	23.020	1.460	14.564
1.027	37.510	1.077	28.619	1.154	22.914	1.470	14.412
1.028	37.198	1.078	28.511	1.156	22.810	1.480	14.264
1.029	36.898	1.079	28.405	1.158	22.708	1.490	14.120
1.030	36.607	1.080	28.299	1.160	22.607	1.500	13.979
1.031	36.327	1.081	28.196	1.162	22.507	1.520	13.708
1.032	36.055	1.082	28.093	1.164	22.408	1.540	13.449
1.033	35.792	1.083	27.992	1.166	22.311	1.560	13.201
1.034	35.537	1.084	27.892	1.168	22.215	1.580	12.964
1.035	35.290	1.085	27.794	1.170	22.120	1.600	12.736
1.036	35.049	1.086	27.696	1.172	22.027		
1.037	34.816	1.087	27.600	1.174	21.934	1.620	12.518
1.038	34.588	1.088	27.505	1.176	21.843	1.640	12.308
1.039	34.367	1.089	27.411	1.178	21.753	1.660	12.107
1.040	34.151	1.090	27.318	1.180	21.664	1.680	11.913
1.041	33.941	1.091	27.226	1.182	21.576	1.700	11.725
1.042	33.736	1.092	27.135	1.184	21.489	1.720	11.545
1.043	33.536	1.093	27.046	1.186	21.403	1.740	11.370
1.044	33.341	1.094	26.957	1.188	21.318	1.760	11.202
1.045	33.150	1.095	26.869	1.190	21.234	1.780	11.039
1.046	32.963	1.096	26.782	1.192	21.151	1.800	10.881
1.047	32.780	1.097	26.697	1.194	21.069		
1.048	32.602	1.098	26.612	1.196	20.988	1.820	10.729
1.049	32.427	1.099	26.528	1.198	20.907	1.840	10.581
1.050	32.256	1.100	26.444	1.200	20.828	1.860	10.437
						1.880	10.298
						1.900	10.163

Equation set (6.2-6) will hold true as long as there is no component mismatch at the input ports. Should such a mismatch occur, additional terms will be required in the equation set. These terms will account for any reflected signal caused by the mismatch. The coefficient of reflectivity, Γ (Equation 6.2-4), for a given mismatch (VSWR) is defined as that fractional amount of a signal which is reflected when a mismatch is encountered (see Table 6-2).

Given a mismatch at port 1 (Figure 6-2), a portion of the signal output at port 1 (Equation (6.2-6a)) will be reflected as a secondary input:

$$IN'_1 = \Gamma (OUT_1) = \Gamma (IN_3\alpha + IN_2\beta) \quad (6.2-7)$$

Thus the input signal at port 1 becomes: IN''_1

$$\text{where} \quad IN''_1 = IN_1 + IN'_1 \quad (6.2-8)$$

Therefore, from Equation (6.2-6):

$$OUT_2 = IN''_1\alpha + IN_3\beta = [IN_1 + \Gamma(IN_3\alpha + IN_2\beta)]\alpha + IN_3\beta \quad (6.2-9a)$$

$$OUT_3 = IN_2\alpha + IN''_1\beta = IN_2\alpha + [IN_1 + \Gamma(IN_3\alpha + IN_2\beta)]\beta \quad (6.2-9b)$$

Similar equations may be generated with mismatches at other ports. These further mismatches will cause a "domino effect" through the entire equation set.

The following effects when a mismatch occurs in a radiometer system typical of the SMMR simulator have been noted:

- a. The ferrite junction isolation will be reduced from that physically measured.
- b. The ferrite junction insertion loss will vary, may increase or decrease, dependent upon VSWR phase relations.
- c. Input signal mixing will occur due to circulator operation and mismatch reflection.

Table 6-2
VSWR-Coefficient of Reflectivity

VSWR	Rho V	Rho P	VSWR	Rho V	Rho P	VSWR	Rho V	Rho P	VSWR	Rho V	Rho P
1.001	0.0005	0.00000	1.051	0.0249	0.00062	1.102	0.0485	0.00235	0.210	0.0950	0.00903
1.002	0.0010	0.00000	1.052	0.0253	0.00064	1.104	0.0494	0.00244	0.220	0.0991	0.00982
1.003	0.0015	0.00000	1.053	0.0258	0.00067	1.106	0.0503	0.00253	1.230	0.1031	0.01064
1.004	0.0020	0.00000	1.054	0.0263	0.00069	1.108	0.0512	0.00262	1.240	0.1071	0.01148
1.005	0.0025	0.00001	1.055	0.0268	0.00072	1.110	0.0521	0.00272	1.250	0.1111	0.01235
1.006	0.0030	0.00001	1.056	0.0272	0.00074	1.112	0.0530	0.00281	1.260	0.1150	0.01324
1.007	0.0035	0.00001	1.057	0.0277	0.00077	1.114	0.0539	0.00291	1.270	0.1189	0.01415
1.008	0.0040	0.00002	1.058	0.0282	0.00079	1.116	0.0548	0.00301	1.280	0.1228	0.01508
1.009	0.0045	0.00002	1.059	0.0287	0.00082	1.118	0.0557	0.00310	1.290	0.1266	0.01604
1.010	0.0050	0.00002	1.060	0.0291	0.00085	1.120	0.0566	0.00320	1.300	0.1304	0.01701
1.011	0.0055	0.00003	1.061	0.0296	0.00088	1.122	0.0575	0.00331	1.310	0.1342	0.01801
1.012	0.0060	0.00004	1.062	0.0301	0.00090	1.124	0.0584	0.00341	1.320	0.1379	0.01902
1.013	0.0065	0.00004	1.063	0.0305	0.00093	1.126	0.0593	0.00351	1.330	0.1416	0.02006
1.014	0.0070	0.00005	1.064	0.0310	0.00096	1.128	0.0602	0.00362	1.340	0.1453	0.02111
1.015	0.0074	0.00006	1.065	0.0315	0.00099	1.130	0.0610	0.00373	1.350	0.1489	0.02218
1.016	0.0079	0.00006	1.066	0.0319	0.00102	1.132	0.0619	0.00383	1.360	0.1525	0.02327
1.017	0.0084	0.00007	1.067	0.0324	0.00105	1.134	0.0628	0.00394	1.370	0.1561	0.02437
1.018	0.0089	0.00008	1.068	0.0329	0.00108	1.136	0.0637	0.00405	1.380	0.1597	0.02549
1.019	0.0094	0.00009	1.069	0.0333	0.00111	1.138	0.0645	0.00417	1.390	0.1632	0.02663
1.020	0.0099	0.00010	1.070	0.0338	0.00114	1.140	0.0654	0.00428	1.400	0.1667	0.02778
1.021	0.0104	0.00011	1.071	0.0343	0.00118	1.142	0.0663	0.00439	1.410	0.1701	0.02894
1.022	0.0109	0.00012	1.072	0.0347	0.00121	1.144	0.0672	0.00451	1.420	0.1736	0.03012
1.023	0.0114	0.00013	1.073	0.0352	0.00124	1.146	0.0680	0.00463	1.430	0.1770	0.03131
1.024	0.0119	0.00014	1.074	0.0357	0.00127	1.148	0.0689	0.00475	1.440	0.1803	0.03252
1.025	0.0123	0.00015	1.075	0.0361	0.00131	1.150	0.0698	0.00487	1.450	0.1837	0.03374
1.026	0.0128	0.00016	1.076	0.0366	0.00134	1.152	0.0706	0.00499	1.460	0.1870	0.03497
1.027	0.0133	0.00018	1.077	0.0371	0.00137	1.154	0.0715	0.00511	1.470	0.1903	0.03621
1.028	0.0138	0.00019	1.078	0.0375	0.00141	1.156	0.0724	0.00524	1.480	0.1935	0.03746
1.029	0.0143	0.00020	1.079	0.0380	0.00144	1.158	0.0732	0.00536	1.490	0.1968	0.03873
1.030	0.0148	0.00022	1.080	0.0385	0.00148	1.160	0.0741	0.00549	1.500	0.2000	0.04000
1.031	0.0153	0.00023	1.081	0.0389	0.00152	1.162	0.0749	0.00561	1.520	0.2063	0.04258
1.032	0.0157	0.00025	1.082	0.0394	0.00155	1.164	0.0758	0.00574	1.540	0.2126	0.04520
1.033	0.0162	0.00026	1.083	0.0398	0.00159	1.166	0.0766	0.00587	1.560	0.2188	0.04785
1.034	0.0167	0.00028	1.084	0.0403	0.00162	1.168	0.0775	0.00600	1.580	0.2248	0.05054
1.035	0.0172	0.00030	1.085	0.0408	0.00166	1.170	0.0783	0.00614	1.600	0.2308	0.05325
1.036	0.0177	0.00031	1.086	0.0412	0.00170	1.172	0.0792	0.00627	1.620	0.2366	0.05600
1.037	0.0182	0.00033	1.087	0.0417	0.00174	1.174	0.0800	0.00641	1.640	0.2424	0.05877
1.038	0.0186	0.00035	1.088	0.0421	0.00178	1.176	0.0809	0.00654	1.660	0.2481	0.06156
1.039	0.0191	0.00037	1.089	0.0426	0.00182	1.178	0.0817	0.00668	1.680	0.2537	0.06438
1.040	0.0196	0.00038	1.090	0.0431	0.00185	1.180	0.0826	0.00682	1.700	0.2593	0.06722
1.041	0.0201	0.00040	1.091	0.0435	0.00189	1.182	0.0834	0.00696	1.720	0.2647	0.07007
1.042	0.0206	0.00042	1.092	0.0440	0.00193	1.184	0.0842	0.00710	1.740	0.2701	0.07294
1.043	0.0210	0.00044	1.093	0.0444	0.00197	1.186	0.0851	0.00724	1.760	0.2754	0.07582
1.044	0.0215	0.00046	1.094	0.0449	0.00202	1.188	0.0859	0.00738	1.780	0.2806	0.07872
1.045	0.0220	0.00048	1.095	0.0453	0.00206	1.190	0.0868	0.00753	1.800	0.2857	0.08163
1.046	0.0225	0.00051	1.096	0.0458	0.00210	1.192	0.0876	0.00767	1.820	0.2908	0.08455
1.047	0.0230	0.00053	1.097	0.0463	0.00214	1.194	0.0884	0.00782	1.840	0.2958	0.08748
1.048	0.0234	0.00055	1.098	0.0467	0.00218	1.196	0.0893	0.00797	1.860	0.3007	0.09042
1.049	0.0239	0.00057	1.099	0.0472	0.00222	1.198	0.0901	0.00811	1.880	0.3056	0.09336
1.050	0.0244	0.00059	1.100	0.0476	0.00227	1.200	0.0909	0.00826	1.900	0.3103	0.09631

VSWR Voltage Standing Wave Ratio
Rho V (ρ_v) Voltage Reflection Coefficient
Rho P (ρ_p) Power Reflection Coefficient = ρ_v^2

It is concluded that to determine the true nature of these effects on the radiometer system calibration, a "full-up" mission configuration testing program must be undertaken so as to determine the phase dependent relationships noted in the previous discussion.

7.0 SMMR SIMULATOR CALIBRATION TESTING

In Section 5 an equation set was derived whereby the absolute brightness temperature of the incident scene radiation may be obtained. It was seen that these equations require knowledge of the physical temperature and the signal loss characteristics of the system components. This section details the temperature monitoring techniques and the calibration tests made for component characteristics determinations.

7.1 Component Physical Temperature Monitoring

Table 7-1 delineates the method by which the component physical temperatures are monitored. The components are as defined in Section 4, subscripting as in Table 4-2.

Table 7-1

Component	Equation Symbol(s)	Monitor Method
Radome	t_{10}	Mathematical Average of Total Air Temp ^① and the Antenna Ambient
Antenna	t_{20}	Thermistor ^②
Waveguides Sled Cargo Bay Cabin Cold Load	t_{32} t_{33} t_{42} t_{43} t_{52} t_{53} t_{55} t_{44} t_{54}	Thermistor Thermistor Thermistor Ambient
Calibration Loads Cold	t_{04}	Calculated Boiling Point of LN ₂ ^③
Hot	t_{01}	Thermistor
Ferrite Switch	t_0	Thermistor

Notes:

- (1) Total Air Temperature: ambient air temperature plus ram air temperature where the ram air temperature is a heating effect caused by air flow friction on the aircraft skin—for ground based calibrations ram air temperature is zero.
- (2) Thermistor Monitor: YSI 44006 or YSI 44031; thermistor monitor points are multiplexed to the data recording system; sample rate of approximately once every two minutes.
- (3) Boiling Point of Liquid Nitrogen (LN_2): the cold load temperature is the boiling point of the cryogenic liquid; nominal value 77.2°K; housekeeping data records aircraft cabin altitude, using this value the boiling point is calculated for the given atmospheric pressure.

7.2 Component Calibration Tests

The component characteristics required for the equation sets of Sections 4 and 5 are determined in two sets of tests. Test set one is a component level testing program. Test set two is a system level testing program to take into account the VSWR effects noted in Section 6.

7.2.1 Component Level ("Piece Part") Testing

7.2.1.1 Waveguide, Antenna, Radome Transmissivities

In all instances, the transmissivity (α) for the waveguides, antennae, and radomes is determined radiometrically. The radiometer response equation has the form

$$T_B = A + BV \quad (7.2-1)$$

where

$$T_B \equiv \text{scene}$$

$$A, B \equiv \text{operation constants}$$

$$V \equiv \text{system output voltage}$$

To determine the transmissivity of the lossy element under test, two targets are observed with the radiometer system. Target one is viewed at ambient temperature yielding a radiometer response form:

$$T_{amb} = A + B V_1 \quad (7.2-2)$$

Target two is a cold temperature, either as liquid nitrogen load or the sky. This target will be viewed by the radiometer system twice, once with and once without the lossy element included in the system. For the case of no lossy element we have:

$$T_{cold} = A + B V_2 \quad (7.2-3)$$

For the case of including the lossy element we recall equation 4-1 for radiative transfer through a lossy element and have a response equation of the form

$$\alpha T_{cold} + (1 - \alpha) T_{amb} = A + B V_3 \quad (7.2-4)$$

The element transmissivity is calculated from equations 7.2-2, 7.2-3 and 7.2-4 wherein:

$$\frac{V_3 - V_1}{V_2 - V_1} = \frac{\left(\frac{\alpha T_{cold}}{B} + \frac{(1 - \alpha) T_{amb}}{B} \frac{A}{B} \right) - \left(\frac{T_{amb}}{B} - \frac{A}{B} \right)}{\left(\frac{T_{cold}}{B} - \frac{A}{B} \right) - \left(\frac{T_{amb}}{B} - \frac{A}{B} \right)} \quad (7.2-5)$$

When reduced

$$\frac{V_3 - V_1}{V_2 - V_1} = \alpha \quad (7.2-6)$$

Tables 7-2 and 7-3 delineate the transmissivities for the SMMR Simulator components as determined by the above method.

7.2.1.2 Ferrite Switch Block Leakage Ratios

As was discussed in Section 6, the ferrite switch block will have altered operational characteristics when installed in the radiometer system (altered from manufacturers test data taken with matched loads) due to mismatch with the antenna/waveguide system. Table 7-4 tabulates the VSWR seen by the ferrite junctions looking at the antenna/waveguide systems.

Table 7-2
Waveguide Transmissivities

	10.7		21			37		
	V	H	V	H	UP	V	H	UP
Sled	0.9444	0.9664						
Feedthru	0.9785	0.9809						
Cargo	0.9879	0.9889						
Cabin			0.8498	0.8723	0.8706	0.8335	0.8931	0.7865
Cold Load ¹					0.8766	0.8212	0.8212	0.8212

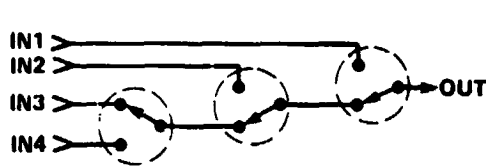
Table 7-3
Antenna Transmissivities

	10.7		21			37		
	V	H	V	H	UP	V	H	UP
Antenna System	0.904	0.839	0.827	0.859	0.826	0.807	0.535	0.5944
Launch Horn	0.982	0.956	0.932	0.947	0.915	0.891	0.592	0.7072
Lens	0.921	0.878	0.886	0.907	0.903	0.906	0.903	0.8405

Table 7-4
Antenna and Waveguide System VSWR

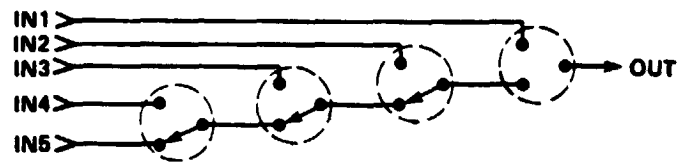
	10.7		21			37		
	V	H	V	H	UP	V	H	UP
Antenna	1.20	1.08	1.35	1.04	1.26	1.13	1.40	1.26
Waveguide	1.08	1.10	1.15	1.12	1.20	1.22	1.16	1.04
Ant and W/G	1.24	1.28	1.47	1.14	1.29	1.19	1.32	1.19

Recall Figures 4-14 and 4-15, schematic representations of the ferrite switch block assemblies (Figure 7-1 below):



6.6, 10.7, 22 GHz

Figure 7-1(a).



18, 37 GHz

Figure 7-1(b).

Define the following symbols:

$W \equiv IN1$ = warm calibration input

$V \equiv IN2$ = vertical polarization input

$H \equiv IN3$ = horizontal polarization input

$C \equiv IN4$ = cold calibration input

$U \equiv IN5$ = uplook (37GHz), terminated (18GHz) input

Define a term called leakage ratio as the ratio of the transmissivity of an undesired signal path (β_{ij}) to the transmissivity of the primary/desired signal path (α_{ij})

$$\mathcal{L}_{ij} \equiv \beta_{ij}/\alpha_{ij} \quad (7.2-7)$$

where $i \equiv$ input where signal originates

$j \equiv$ primary signal path

Observing the possible primary signal paths in Figure 7-1, the following transmissivity values may be determined:

Table 7-5

Primary Path	Undesired Paths
α_{WW}	$\beta_{VW} \beta_{HW} \beta_{CW} \beta_{UW}$
α_{VW}	$\beta_{WV} \beta_{HV} \beta_{CV} \beta_{UV}$
α_{HH}	$\beta_{VH} \beta_{WH} \beta_{CH} \beta_{UH}$
α_{CC}	$\beta_{VC} \beta_{HC} \beta_{WC} \beta_{UC}$
α_{UU}	$\beta_{VU} \beta_{HU} \beta_{CU} \beta_{WU}$

(Note: however, no values are obtained for warm load transmissivities. All measurements are made utilizing the radiometer system. So as to make warm load measurements, disassembly of the radiometer would be required, leaving no test facility.)

The following test procedure was utilized to determine the leakage ratios cognizant with the transmissivities listed in Table 7-5.

Test Step No.	Procedure
1	Turn on radiometer system, allow to thermally stabilize
2	Connect external elements (antenna, waveguide, LN ₂ load) to primary signal path—antenna views ambient load
3	Connect matched load(s) to undesired path(s)
4	Take radiometer output reading with all ports ambient
5	Place LN ₂ matched load on one of unwanted signal path input ports, take radiometer output reading.
6	Calculate β = reading step 5—reading step 4.
7	Repeat step 5 and 6 on other unwanted signal path ports
8	Remove external elements from primary path port, place ambient matched loads on all ports, take radiometer output reading.
9	Place LN ₂ matched load on primary path port, take radiometer output reading.

10 Calculate α = reading step 9- reading step 8.

11 Calculate $\mathcal{L} = \beta/\alpha$

Table 7-6 delineates the SMMR Simulator Ferrite switch(s) leakage ratios as determined by the above procedure.

Table 7-6
Ferrite Leakage Ratio x 100

	10.7	21	37
\mathcal{L}_{CV}	1.206	2.366	0.512
\mathcal{L}_{CH}	3.100	0.588	3.554
\mathcal{L}_{CU}	N/A	2.635	0.183
\mathcal{L}_{VC}	0.184	0.850	1.110
\mathcal{L}_{VH}	0.354	0	0.165
\mathcal{L}_{VU}	N/A	N/A	0.274
\mathcal{L}_{UC}	N/A	0.809	2.840
\mathcal{L}_{UV}	N/A	N/A	0.146
\mathcal{L}_{UH}	N/A	N/A	0.165
\mathcal{L}_{HC}	0.918	0.710	0.880
\mathcal{L}_{HV}	0.371	0.091	0.146
\mathcal{L}_{HU}	N/A	N/A	0.091

7.2.2 System Level Testing

7.2.2.1 Ground ("Hangar") Tests

SMMR Simulator data retrieval is complicated by the factor that the system temperatures/losses are variant dependent upon aircraft installation positioning and aircraft operations wherein sufficient warm up and stabilization time may not be available prior to deployment and data taking commencement and operation at varying altitudes giving varying ambient temperatures.

The following procedure was utilized whereby the SMMR Simulator temperature dependent characteristics were monitored under test conditions. All radiometer system outputs and thermistor monitor points were recorded on magnetic tape for analysis at a later date. Target temperatures were periodically hand logged.

The calibrations involve viewing an Eccosorb target at both ambient temperature and when cooled to liquid nitrogen (77°K) temperature. Therefore, the following procedure is run twice for each radiometer system.

Test Step No.	Procedure
1	Position target before antenna aperture.
2	Start automatic data taking system.
3	Turn on radiometer electronics--allow to stabilize, monitoring hot load temperature.
4	Turn on waveguide heater Section 1 (cabin or cargo bay) - allow system to stabilize.
5	Turn on waveguide Section 2 (sled) if applicable - allow system to stabilize.
6	Turn on antenna heater - if applicable - allow to stabilize.
7	Turn all heater systems off - allow all components to cool to ambient temperature.
8	Turn off data recording system.
9	Repeat procedure with second target temperature.

(Note: Three sets of "hangar" test data were made for the 1978 NIMBUS-G underflight: (1) AMES, pre-deployment, (2) FAIRBANKS, mid-deployment, and (3) AMES, post-deployment. The Fairbanks data set afforded a greater temperature dynamic test range than the two Ames data sets.)

7.2.2.2 Airborn Testing

All SMMR Simulator antennas are installed so as to view the earth at an attitude of 45° down and to the right with respect to the aircraft. Two aircraft maneuvers were executed as often as feasible during the NIMBUS-G underflight series to provide calibration points for the SMMR Simulator.

One maneuver has been termed a "wing over" where the aircraft is placed in a 90° left bank (wings perpendicular to the earth). This points the SMMR Simulator antenna 45° above the horizon thus viewing the sky or cosmic background radiation of approximately 3°K , the best possible cold calibration for the systems.

The second aircraft maneuver utilized for calibration is a 45° right bank during which the radiometer systems are nadir viewing. When nadir viewing, all polarization effects become non-existent and the radiometer channels, when properly calibrated, will have identical readings.

8.0 ALGORITHM COEFFICIENT DETERMINATIONS

The equations have been derived to determine brightness temperatures and calibration tests have been performed. The external loss coefficients and leakage ratios must now be determined using the developed algorithm and test results.

8.1 Determination Technique

Determination of the algorithm coefficients involves an iterative process. Data recorded during the ground and airborne testing procedures is first examined and any gross irregularities noted for exclusion from processing so as to avoid biasing. Six second time averages are calculated for system normalized counts and coordinated with thermistor value temperature calculations. All data is subsequently stored on magnetic disc media for analysis. "Piece part" data are entered into the data set by hand for each appropriate calculation.

The coefficients are calculated in a four pass process. First, the value of α_R is determined from the warm up data obtained in ground testing. Secondly, piece part measurements for leakage ratios are utilized to calculate values of T_{FH} , T_{FV} , and/or T_{FU} . The third pass calculates the external loss coefficients utilizing piece part and ground test data. The fourth pass utilizes air-born test data to "fine tune" the coefficients.

8.1.1 Determination of α_R

Recall the switch block input effective brightness temperature equation (5.1-21)

$$T_{Fi} = T_{FW} - \left(T_{FW} - T_{FC} + \frac{L_c - L_w}{A_c} \right) \alpha_{Ri} N_i - \frac{L_i + L_w}{A_i} \quad (8.1-1)$$

The term α_{Ri} was seen to be a transmissivity ratio between the cold calibration signal path and the measurement path of interest.

$$\alpha_{Ri} = A_c/A_i \quad (8.1-2)$$

Let the switch block leakages be negligible ($L = 0$) and define

$$Z = (-T_{FC} + T_{FW}) N_i \quad (8.1-3)$$

Then

$$T_{Fi} = T_{FW} - Z \alpha_{Ri} \quad (8.1-4)$$

$$\frac{dT_{Fi}}{dT_{FW}} = 1 - \frac{dZ}{dT_{FW}} \alpha_{Ri} \quad (8.1-5)$$

Under test conditions, T_{Fi} is held constant and therefore:

$$\frac{dT_{Fi}}{dT_{FW}} = 0 \quad (8.1-6)$$

thus

$$\alpha_{Ri} = \frac{dT_{FW}}{dZ} \quad (8.1-7)$$

It is thus seen that α_R is dependent upon the physical temperature of the switch block. Therefore data taken during warm up testing is descriptive of α_R .

An initial value of α_R is determined from a plot of $(T_{Fi} - T_{iW})$ vs. $(T_{iW} - T_{iC}) N_i$. If the warm up characteristic is a linear relationship, the slope of the plotted line will be α_R . Figures 8-1, 8-2, and 8-3 are the graphic determination of α_R for the 10.7, 21, and 37GHz systems respectively.

Inspection of the data plots shows a nonlinearity during the initial warm up period. This is particularly noticeable in the 37GHz systems wherein warm up time was on the order of one hour. So as to preclude biasing due to the nonlinearity, a secondary determination method for α_R is indicated.

Recalling Equation (8.1-5), it is seen that α_{Ri} is directly proportional to dT_{Fi}/dT_{iW} . Also recall Equation (8.1-6), which implies a plot of brightness temperatures during the radiometer system warm up should track the target temperature being observed regardless of the system physical temperature changes (i.e., slopes of two plots should be equal). The values of α_R determined in Figures 8-1, 8-2, and 8-3 are used as initial values to plot $T_{Fi} = T_{iW} - (-T_{iC} + T_{iW}) \alpha_{Ri} N_i$ versus time. Simultaneously, T_{target} and T_{iW} are plotted versus time. The value of α_R is varied around that previously determined and plots are made of T_{Fi} vs. time. A value of α_R being that value which causes the plot of T_{Fi} versus time to most closely track T_{target} versus time, (i.e., the two plots have equal slopes).

Figure 8-4 illustrates this plotting procedure for the 37GHz vertical polarization channel.

8.1.2 Leakage Coefficients Determination (L_{lm})

Leakage ratios calculated from piece part measurements were the sole means of determining values for the leakage coefficients defined in the calibration equation.

8.1.3 External Loss Coefficients

The hangar tests, in which the various components are tested by allowing their respective heaters to cycle while all other components and targets are held at constant temperatures, are used to calculate the external loss coefficients.

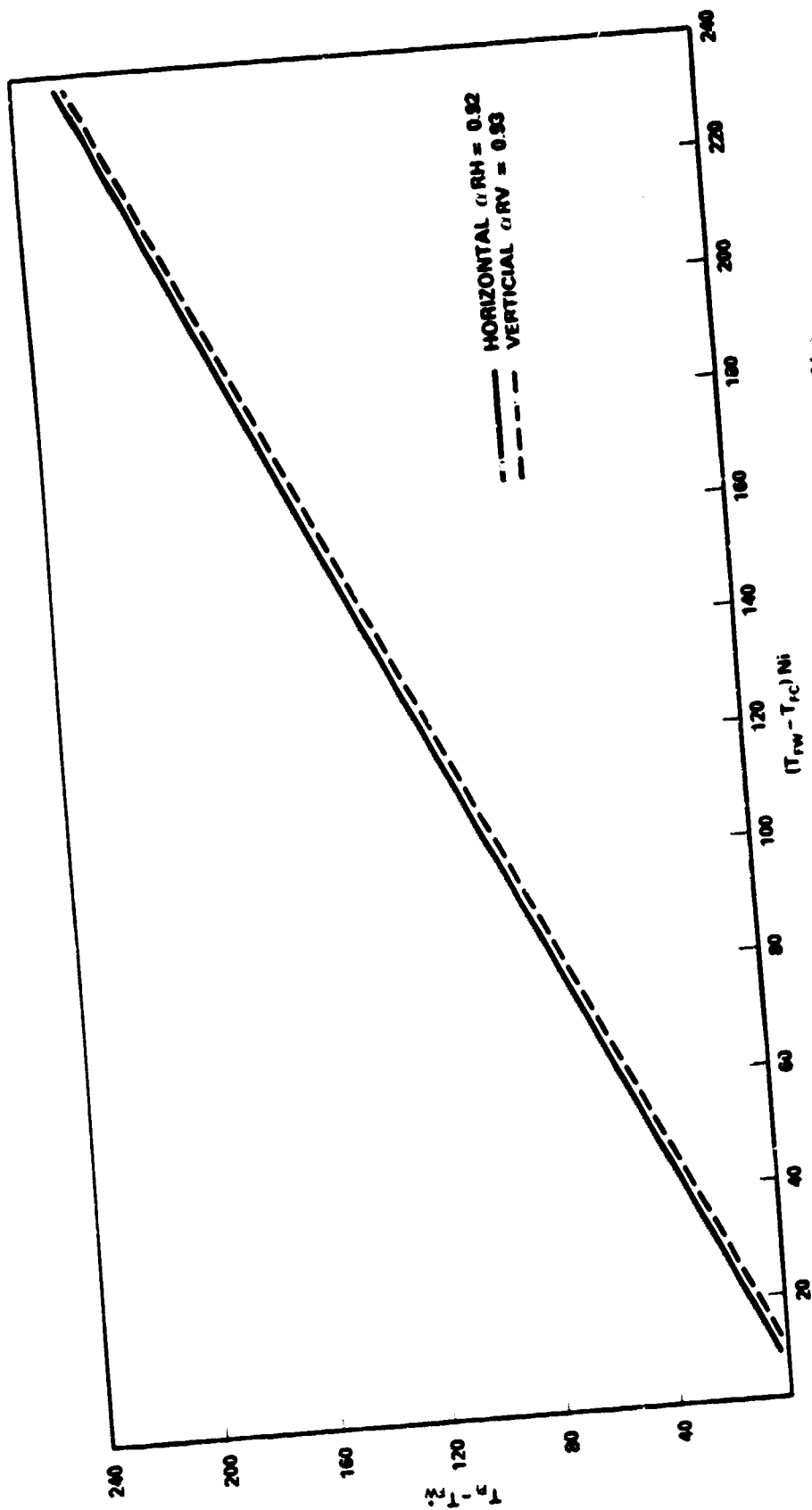


Figure 8-1. α_R : 10G11/ Radiometer System (Piece Part Test Warm Up)

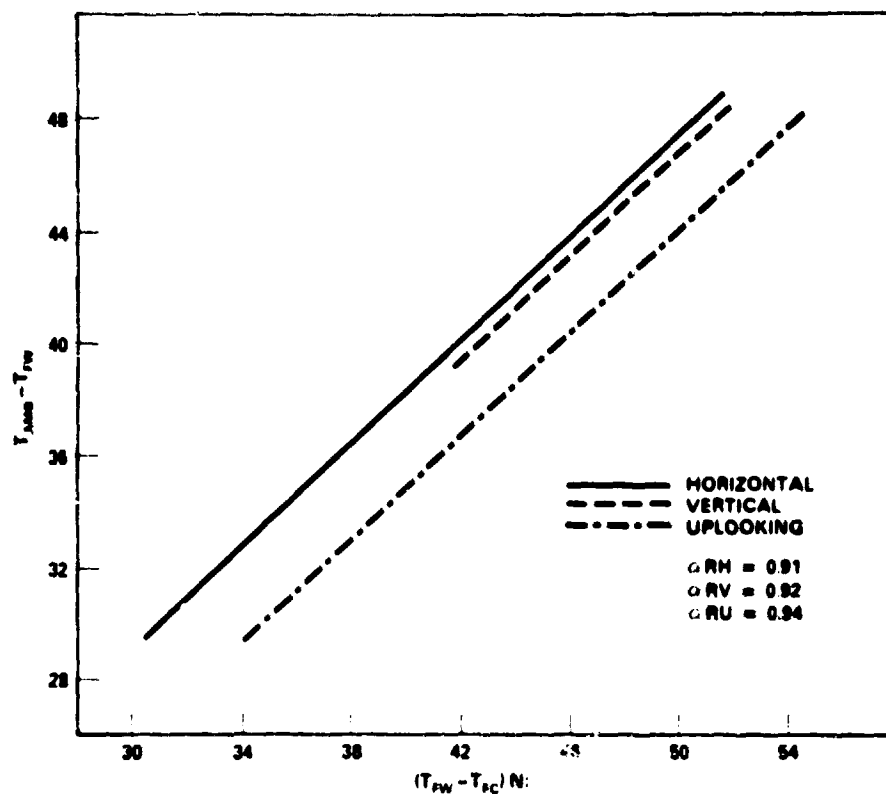


Figure 8-2. α_R : 21 GHz Radiometer Systems (Fairbanks Ambient Target, Warm Up)

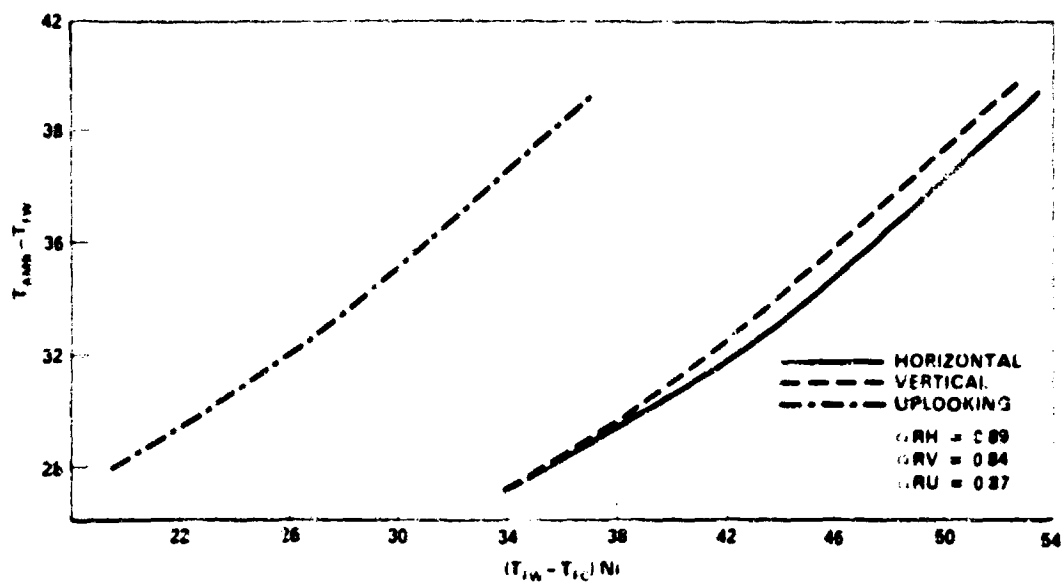


Figure 8-3. α_R : 37 GHz Radiometer Systems (Fairbanks Ambient Target, Warm Up)

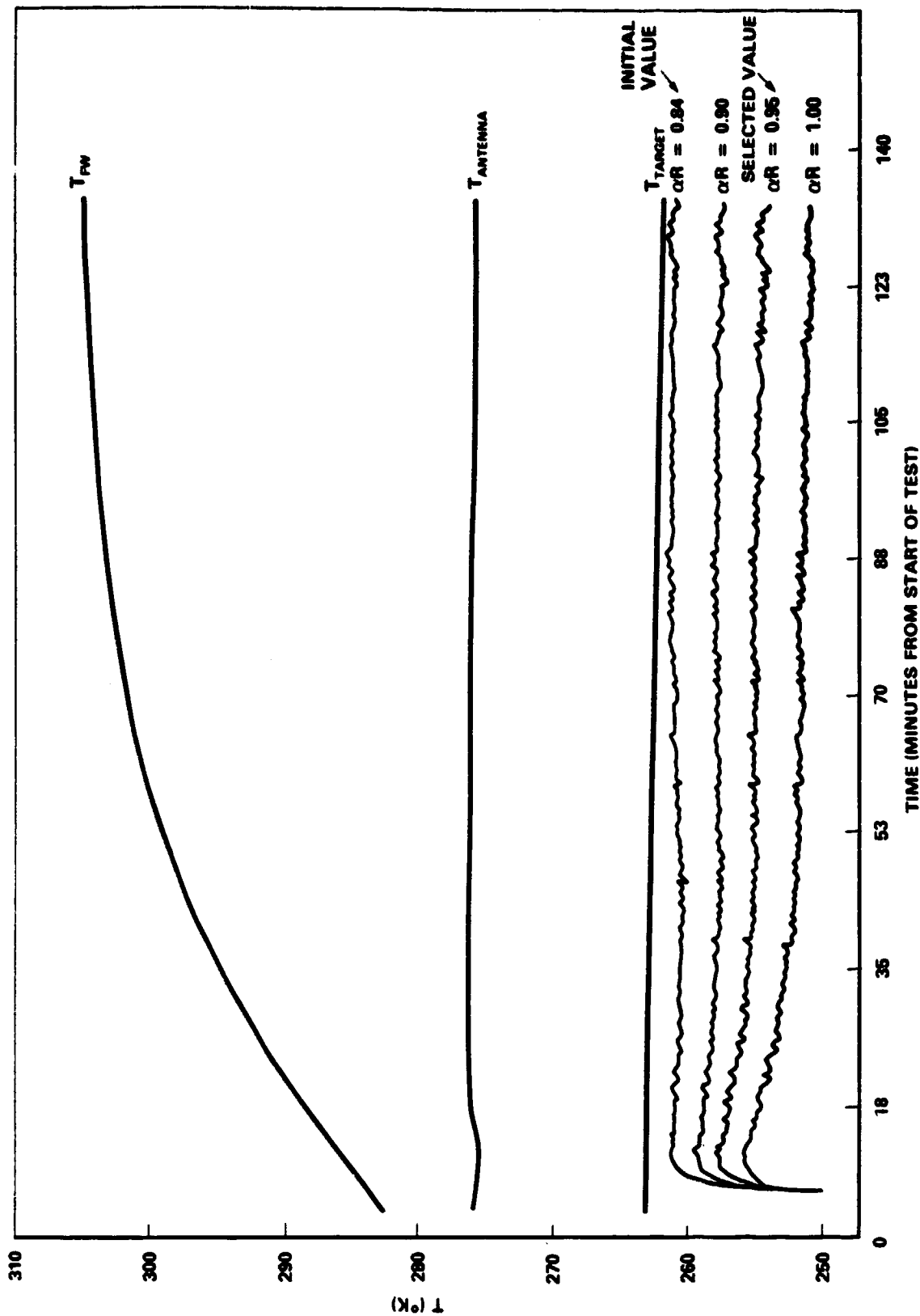


Figure 8-4. α_{RV} : 37GHz Vertical Polarization

Recall Equation (5.1-1a) which describes the effect of the external losses on the incident brightness temperature:

$$T_{FB} = \alpha_4 \alpha_3 \alpha_2 \alpha_1 T_B + (1 - \alpha_4) \alpha_3 \alpha_2 \alpha_1 t_4 + (1 - \alpha_3) \alpha_2 \alpha_1 t_3 + (1 - \alpha_2) \alpha_1 t_2 + (1 - \alpha_1) t_1 \quad (8.1-8)$$

A value for T_{FB} is calculated from the test data using the previously determined coefficient values of α_R and \mathcal{L}_{mn} . With all variables held constant except t_1 , the physical temperature associated with the waveguide loss term (α_1), the value of α_1 may be calculated.

As t_1 varies, so will T_{FB} vary. Algebraic manipulation shows that

$$\alpha_1 = 1 - \Delta T_{FB} / \Delta t_1 \quad (8.1-9)$$

Similarly by holding all variables constant with the exception of t_2 it is seen that:

$$\alpha_2 = 1 - (\Delta T_{FB} / \Delta t_2) \alpha_1 \quad (8.1-10)$$

Having previously determined a value for α_1 , α_2 is calculable. Likewise:

$$\alpha_3 = 1 - (\Delta T_{FB} / \Delta t_3) \alpha_2 \alpha_1 \quad (8.1-11)$$

and

$$\alpha_4 = 1 - (\Delta T_{FB} / \Delta t_4) \alpha_3 \alpha_2 \alpha_1 \quad (8.1-12)$$

Piece part measurements are utilized for determination of the external loss coefficients when the variations in physical component temperature during the hangar tests are insignificant and/or signal variation due to this physical temperature change is insignificant. In-as-much-as neither the antenna nor the radomes have heaters the hangar test procedures will not yield the requisite variations to determine values of α_3 and α_4 . These two loss coefficients are determined from piece part measurements (Section 7.2.1).

The calculation procedure noted in Section 7.2.1 is modified for determining radome loss in-as-much-as the radome is tested utilizing the complete radiometer system. Two equations are known, one each for the radome in place ("on") and radome removed ("off"):

$$T_{ON} = \alpha_4 \alpha T_B + (1 - \alpha_4) \alpha t_4 + L \quad (8.1-13)$$

$$T_{OFF} = \alpha T_B + L \quad (8.1-14)$$

where

$$\alpha = \alpha_3 \alpha_2 \alpha_1 \quad (8.1-15a)$$

$$L = (1 - \alpha_3) \alpha_2 \alpha_1 t_3 + (1 - \alpha_2) \alpha_1 t_2 + (1 - \alpha_1) t_1 \quad (8.1-15b)$$

t_4 = ambient temperature at time of test

The target is identical in both test conditions. The equations are thus solved for T_B and equated. Terms are rearranged and solution for α_4 is determined:

$$\alpha_4 = \frac{T_{ON} - \alpha t_4 - L}{T_{OFF} - \alpha t_4 - L} \quad (8.1-16)$$

Where T_{ON} and T_{OFF} are calculated from the test data using the previously determined coefficient values of α_R and \mathcal{L}_{mn} .

8.1.4 "Fine Tuning" the Coefficient Determination(s)

As noted in Section 7.2.2.2 wingover maneuvers are made periodically throughout the experiment flight series. The radiometers view the cosmic background radiation of 2.7°K. This establishes a good cold target for the radiometers to be calibrated against.

The wingover data is utilized as a check for the algorithm utilizing coefficients determined in prior testing. Should there be a discrepancy between calculated brightness temperature during the wingover and the predicted 2.7°K, the wingover data is used to "Fine tune" the coefficient value which is considered to have the greatest potential determination error.

Given the test data values, a known target (T_B), and all but one coefficient, the algorithm equation may be solved for the unknown loss coefficient.

Figure 8-5 illustrates the iterative process used in determining the equation coefficients for the 37GHz vertical polarization channel.

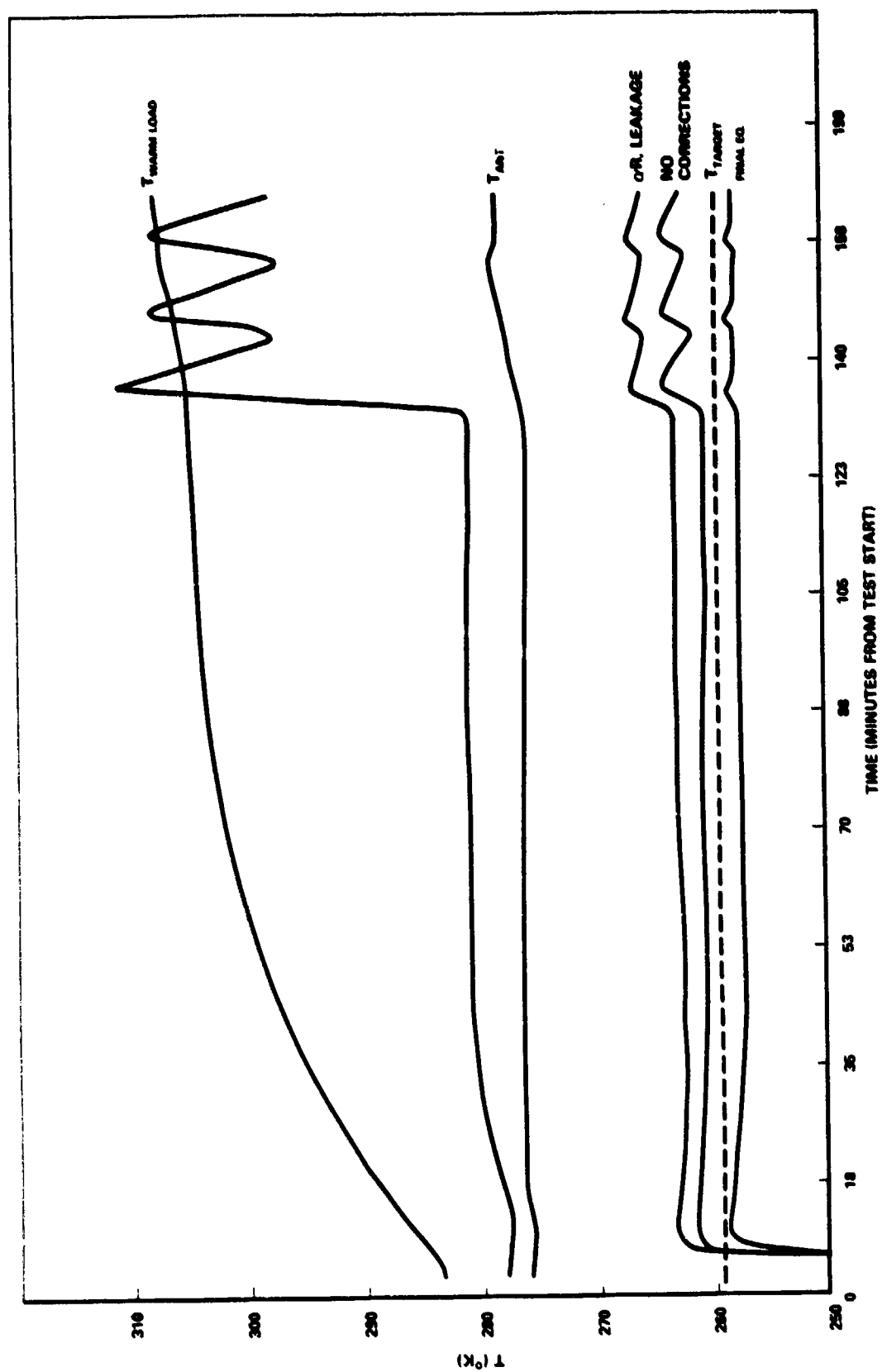


Figure 8-5. Iterative Coefficient Determination - 37GHz Vertical

8.2 System Coefficient Determination

Each radiometer system's loss coefficients were determined from different subsets of the test data. Table 8-1 summarizes the test(s) used in determining the system loss coefficients.

Table 8-1

System	Waveguide	Radome	Antenna	Ferrite
10.7	Piece Part	Wingover	Piece Part	Piece Part
21	Hangar	N/A	Piece Part	Piece Part
21 Uplook	Piece Part	N/A	High Altitudes*	Piece Part
37	Hangar	N/A	Wingover	Piece Part
37 Uplook	Hangar	N/A	Piece Part	Piece Part

[*NOTE: When at high altitude, the uplooking radiometers are seeing cosmic background at 2.7°K.]

8.2.1 10.7GHz Radiometer System

The 10.7GHz radiometer waveguide transmissivities were high enough that the hangar calibration tests were not used since changes in heater temperatures had no discernable effect on the output calculated radiances, T_{FF} . Therefore, piece-part measurements were used to obtain these values. The antenna transmissivities were also determined using piece-part measurements.

The 10.7GHz radiometer posed a special problem since there is a radome in the system. The Radome on/off tests were deemed useless when calculated loss coefficients were found to be unreasonably large (approximately two orders of magnitude). Therefore, wingover data was employed to determine the radome loss coefficient.

8.2.2 21GHz Radiometer System

The waveguides of the 21GHz system were sufficiently lossy that corresponding loss coefficients could be determined using the hangar heater measurements. Some error can be expected in the α_R term since the 21GHz warm-up is fairly quick, therefore, the data used to determine α_R is not in large supply. Wingovers were used as a cold target test to fine-tune the transmissivity

ratio, α_R . However, since the waveguide transmissivities were calculated from hangar measurement which included equations that contained the transmissivity ratio, α_R , these loss coefficients are recalculated using the new transmissivity ratio term.

8.2.3 21GHz Uplook Radiometer System

The 21GHz Uplook waveguide transmissivity used in the algorithm was taken from piece-part measurements. Piece-part measurement of antenna loss yielded a value that was questioned as possibly being too low, hence, the high-altitude portions of a randomly chosen flight was used as a calibration test with space as a cold target (2.7°K) to determine a value for the antenna transmissivity.

8.2.4 37GHz and 37GHz Uplook Radiometer Systems

The 37GHz and 37GHz Uplook radiometers have the same receiver so the two systems are treated as one. Since the 37GHz hot load has the longest, close to an hour, warm-up period sufficient data is available to determine the transmissivity ratio with some confidence. Waveguide components were so lossy that the hangar measurements were used to determine their transmissivities. Antenna losses, as seen from piece-part measurements, were large; however, changes in antenna temperature during testing were not large enough that effects of these changes were evident in plotted radiances. Therefore, the piece-part measurements of antenna transmissivities were used initially.

Again, the wingover data set was used to fine tune the antenna loss coefficient for the 37 GHz radiometer system to achieve a good set of calculated brightness temperatures. High-altitude data analysis for the 37GHz Uplook radiometer system using previously determined coefficients yielded consistent good results, therefore no further modification of the loss coefficients was necessary.

8.3 Algorithm Coefficients Summary

Table 8-2 compares the calculated (system) transmissivity coefficients with those determined during piece-part measurements.

Table 8-3 lists the leakage coefficients.

Table 8-4 lists the external loss coefficients.

Table 8-2
SMR Simulator Transmissivity Coefficients
Calculated vs. Piecepart Coefficients

Element/Channel			10.7GHz System/Piecepart		21GHz System/Piecepart		37GHz System/Piecepart	
Cabin WG	α_1	H	—	0.94	0.88	0.87	0.93	0.89
	α_1	V	—	0.97	0.92	0.85	0.89	0.83
	α_1	UP	N/A	N/A	0.87	0.87	0.82	0.78
Sled WG	α_2	H	—	0.97	N/A	N/A	N/A	N/A
	α_2	V	—	0.94	N/A	N/A	N/A	N/A
	α_2	UP	N/A	N/A	N/A	N/A	N/A	N/A
Antenna	α_3	H	—	0.84	0.88	0.86	0.58	0.59
	α_3	V	—	0.90	0.83	0.83	0.83	0.81
	α_3	UP	N/A	N/A	0.83	0.83	0.60	0.59
Radome	α_4	H	0.83	—	N/A	N/A	N/A	N/A
	α_4	V	0.93	—	N/A	N/A	N/A	N/A
	α_4	UP	N/A	N/A	N/A	N/A	N/A	N/A
	α_R	H	0.94	0.92	0.90	0.91	0.97	0.89
	α_R	V	0.94	0.93	0.90	0.92	0.95	0.84
	α_R	UP	N/A	N/A	0.96	0.94	0.95	0.87

Table 8-3
Leakage Coefficients x 100

Coefficient	10.7	21	21UP	37	37UP
L_{VH}	0.354	0.000	N/A	0.165	N/A
L_{CH}	3.100	0.588	N/A	3.554	N/A
L_{UH}	N/A	N/A	N/A	N/A	0.165
L_{HV}	0.371	0.091	N/A	0.146	N/A
L_{CV}	1.206	2.366	N/A	0.512	N/A
L_{UV}	N/A	N/A	N/A	N/A	0.146
L_{HC}	0.918	0.710	N/A	0.880	N/A
L_{VC}	0.184	0.850	N/A	1.110	N/A
L_{UC}	N/A	N/A	0.809	N/A	2.840
L_{HU}	N/A	N/A	N/A	N/A	0.091
L_{VU}	N/A	N/A	N/A	N/A	0.274
L_{CU}	N/A	N/A	2.635	N/A	0.183

Table 8-4
External Loss Coefficients

Coefficient	10.7		21			37		
	H	V	H	V	UP	H	V	UP
α_R	0.94	0.94	0.90	0.90	0.96	0.97	0.95	0.95
α_0	0.65	0.76	0.77	0.76	0.59	0.54	0.74	0.49
ℓ_1	0.03	0.03	0.12	0.08	0.13	0.07	0.11	0.18
ℓ_2	0.03	0.06	N/A	N/A	N/A	N/A	N/A	N/A
ℓ_3	0.15	0.09	0.11	0.16	0.28	0.39	0.15	0.33
ℓ_4	0.14	0.06	N/A	N/A	N/A	N/A	N/A	N/A
ℓ_c	N/A	N/A	N/A	N/A	0.88	0.82	0.82	0.82

9.0 ALGORITHM VERIFICATION

9.1 Calibration Data Anomalies

9.1.1 Cold Calibration Target

Liquid nitrogen filled targets were instrumental in the planning of the ground-based two-point calibration measurement plan (Section 7.2.2.1).

The targets to be used in the tests had originally been intended as a quick look calibration target wherein the target was flooded with liquid nitrogen and a data set taken; total test time approximately 5 minutes. The extended testing planned (3 to 5 hours) dictated modifications to the target: (1) a layer of insulating foam as closure to the system to preclude condensation and icing, (2) continual filling with LN_2 to assure the microwave absorber being immersed. Calculations showed the target would have an effective brightness temperature of approximately 100°K . A platinum sensor was placed in the target material as a temperature/ LN_2 level monitor.

Initial plotting of the receiver output radiances displayed variances in the target temperature. Additionally, identical tests performed at different times (e.g., pre-flight AMES and post-flight AMES) had widely varying radiances.

These radiance variances are attributed to frost and liquid water build up on the target surface. AMES' relative humidity was high during the testing periods (close proximity to San Francisco Bay) and the target surface was less than dew point temperature thus condensation occurred in spite of the insulation foam closure.

Calculations were performed with the finished algorithm to determine the LN_2 target brightness temperatures. The resultant variance was in a range of 110°K to 140°K .

In light of the unpredictable value of the target brightness temperature, the data taken during the hangar calibration testing with the LN_2 targets was not utilized in the algorithm coefficient determinations. Data obtained during high altitude flights and wing over maneuvers was substituted as the cold calibration target data for the coefficient determination effort.

Future two-point calibration testing using a cryogenic temperature target will require development of a target which will not be disturbed by condensation and frosting.

9.1.2 Ambient Calibration Target

The duration of a single calibration test series was usually 1 to 2 hours with several test series run in a row. The ambient temperature was manually recorded at the beginning and ending of each series and a linear temperature change assumed between the two measurements. This infrequent monitoring gives rise to uncertainty of the true target temperature at any given time during the testing period. This can be noted in the plotted brightness temperatures (values calculated from the algorithm) as compared to the linearly represented target temperature plots.

The uplooking window mounted radiometer systems present an additional uncertainty in target temperature. An ambient target was utilized for testing. It was noted in the data analysis that the radiance more closely tracked the antenna physical temperature than the ambient temperature. It has been suggested the true temperature of the target lies between the recorded ambient and antenna temperatures in as much as the target may absorb heat from the antenna due to the antenna waveguide heater system operation. Therefore, in the algorithm coefficient determinations, the calculated brightness temperatures were forced to fall between the recorded ambient and antenna temperatures.

9.1.3 Component Level ("Piece Part") Testing VSWR Effects

As seen in Section 7.2.1, the transmissivity of a given component is obtained from the ratio of a set of measurements taken with and without the test component in place in the radiometer system.

$$\alpha = \frac{V_G - V_{AMB}}{V - V_{AMB}} \quad (9-1)$$

where α = component transmissivity

V_G = cold target system output voltage with component in place

V = cold target system output voltage with component removed

V_{AMB} = warm target system output voltage

As seen in Section 6, variance in the input VSWR to the radiometer system will directly effect the system operation characteristics and therefore system output voltage. The component being tested will cause a variance in the system input VSWR. It can be seen that

$$\alpha = \frac{|\Gamma_G|}{|\Gamma|} \alpha_G \quad (9-2)$$

where α = "true" component transmissivity

α_G = measured component transmissivity per method of Section 7.2.1

Γ_G = system input VSWR with component in system

Γ = system input VSWR without component in system

Dependent upon the phase and magnitude relationships of the system input VSWRs, the true component transmissivity may vary from that measured.

9.1.4 Waveguide Heater, 21 GHz Vertical Channel

The 21 GHz radiometer system exhibited an instrument anomaly, when the vertical channel waveguide heater was operational the system output radiance rose approximately 6°K. This rise is constant throughout the cycling of the heater and is presented in all processed data. In as much as the waveguide heater is operational during all data flights, 6°K is subtracted from the algorithm derived brightness temperature for the 21 GHz vertical polarized channel.

9.2 Algorithm Verification

Figure 9-1 illustrates the SMMR Simulator system outputs after being run through the algorithm as developed in this document. The data plotted in Figure 9-1 are representative portions of the ground based ("hangar") calibration tests. It is noted that the algorithm derived brightness temperatures are in very close agreement with the measured target temperatures in all systems as the system operating conditions and physical temperatures are varied.

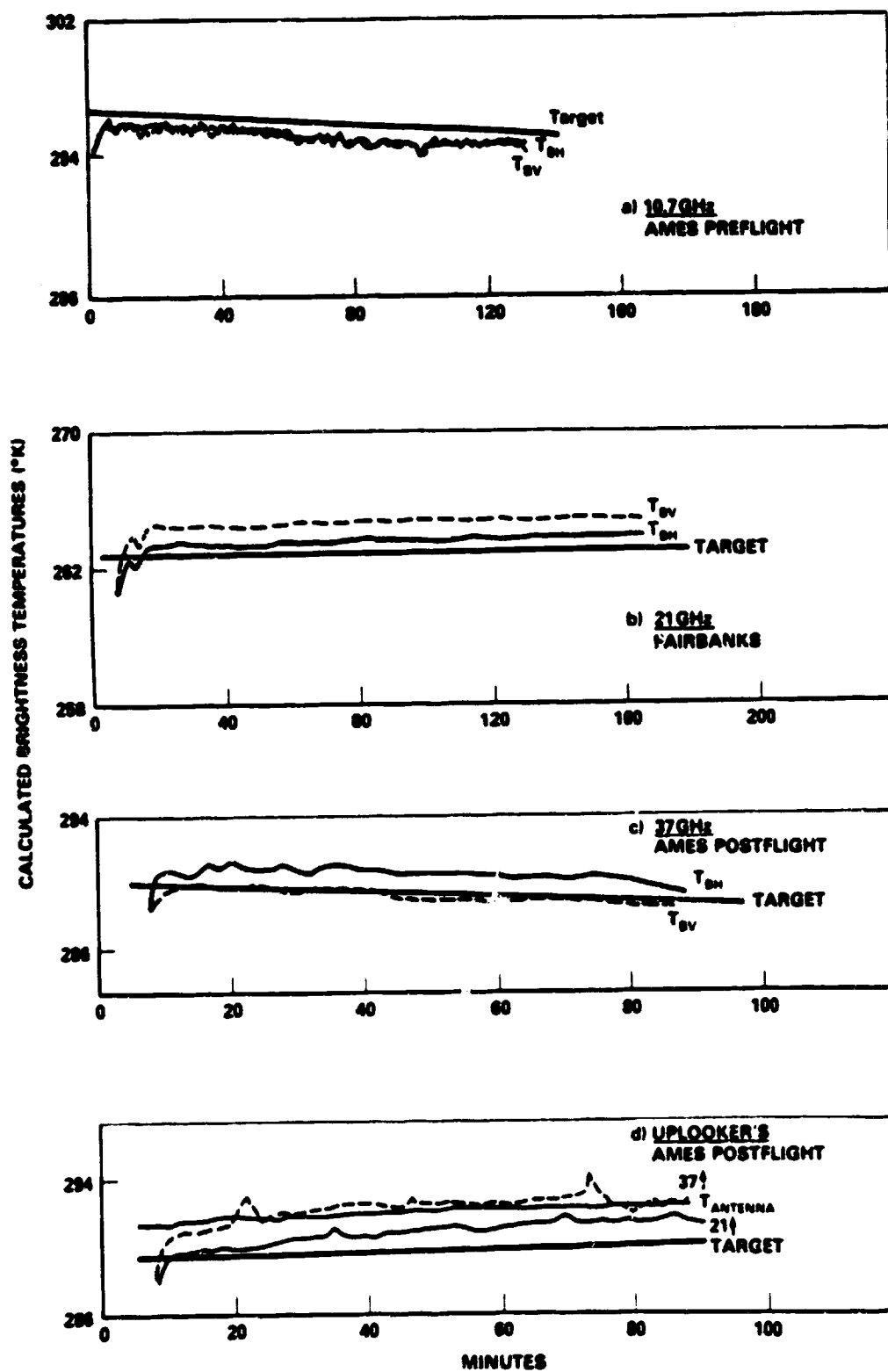


Figure 9-1. Systems Data Consistency Check

The aircraft 45° bank turns remain as the primary source of data for verification of the downlooking radiometer system's algorithms. As noted in Section 7.2.2.2, the 45° bank turns permit the downlooking radiometer systems to be nadir viewing which negates all polarization effects. Thus, the algorithms should provide equivalency between the horizontal and vertical channel calculated brightness temperatures. Table 9-1 presents calculated brightness temperatures for three series of 45° bank turns, two over open ocean and one over ice (Pond Inlet).

Dependent upon the sea/ice conditions at the time of the test run and the radiometer system's NEΔT, a difference of 2°K to 4°K between the algorithm's calculated brightness temperatures for the horizontal and vertical channels is expected. The 21GHz and 37GHz radiometer systems show good consistency/matching between the two channels, i.e., within the expected variance range of 2°K to 4°K. The 10.7GHz radiometer system falls outside the "good" range with a variance of 8°K to 10°K. It is noted that no antenna pattern perturbations have been

Table 9-1
SMR Simulator Calibration
45° Bank Turn Calculations/Fall 1978 Mission

Day #	10.7GHz				21GHz				37GHz			
	Angle	H	V	Δ	Angle	H	V	Δ	Angle	H	V	Δ
259	43.1	97.76	112.8	15.0	43.1	166.2	161.6	4.6	42.8	152.8	157.3	4.5
259	43.3	97.13	115.3	18.2	43.3	165.6	163.5	2.1	44.0	154.8	157.8	3.0
259	42.8	97.96	116.0	18.0	42.8	164.6	163.5	1.1	44.9	153.3	157.6	4.3
259	44.4	98.46	115.0	16.5	44.4	166.0	162.3	3.7				
259	44.0	99.01	115.1	16.1	44.0	166.9	162.9	4.0				
264	45.7	102.3	118.7	16.4	45.7	162.0	161.2	0.8	45.1	168.3	155.6	12.7
264	45.4	103.9	117.8	15.5	45.4	164.6	160.2	4.4	46.3	165.4	158.1	7.3
264	46.4	104.3	120.3	16.0	46.4	164.4	161.9	2.5				
Pond Inlet Ice	43.6	228.6	237.1	8.5	43.6	250.4	249.8	0.6	43.6	248.9	243.9	5.0

included in the algorithm development. It is postulated that the 10.7GHz antenna system has antenna pattern perturbations (decreased beam efficiency, channel cross polarization) which are at least an order of magnitude greater than in the 21 GHz and 37GHz antenna systems, a sufficient value to require inclusion in the algorithm. Work is being undertaken to include antenna performance in the algorithm and will be reported at a later time.

Though sets of high altitude and 90° wingover data have been utilized in determining the algorithm coefficient values, a good check of the model/algorithm is the consistency of the brightness temperatures calculated from these data. In as much as flight conditions and thereby instrument environment conditions vary, the consistent values for the calculated brightness temperatures seen in Tables 9-2 thru 9-6 illustrate the accuracy of the model and coefficients.

Table 9-2
SMMR Simulator Calibration
High-Altitude Calculations/Fall 1978 Mission

21 GHz Uplooker Channel	Day	Time	Calculated T _B
21 GHz	254	43214	3.542
21 GHz	254	43614	4.399
21 GHz	254	44014	3.299
21 GHz	254	44414	3.700
21 GHz	254	44814	2.459
21 GHz	254	45214	2.624
21 GHz	254	45614	3.892
21 GHz	254	50014	1.7511
21 GHz	254	50414	3.335
21 GHz	254	50814	2.313
21 GHz	254	51214	2.072
21 GHz	254	51614	1.959
21 GHz	254	52914	2.204

21↑	↑
Mean	2.873
Variance (Mean)	0.827
Variance (2.7)	0.8445

Table 9-3
SMMR Simulator Calibration
High-Altitude Calculations/Fall 1978 Mission

37 GHz Uplooker Channel	Day	Time	Calculated T_B
37GHz	254	43214	2.731
37GHz	254	44014	2.708
37GHz	254	44414	2.469
37GHz	254	44814	4.297
37GHz	254	45214	2.167
37GHz	254	45614	4.066
37GHz	254	50414	0.728
37GHz	254	50814	0.927
37GHz	254	51614	2.372
37GHz	254	52920	2.178

37↑	↑
Mean	2.464
Variance (Mean)	1.078
Variance (2.7)	1.103

Table 9-4
SMMR Simulator Calibration
10.7 GHz Wingover Calculations/Fall 1978 Mission

Channel	Day	Calculated T_B
10.7GHz H	181	3.157
V	181	0.568
10.7GHz H	223	5.382
V	223	2.099
10.7GHz H	254	4.208
V	254	1.591
10.7GHz H	258	3.232
V	258	4.208
10.7GHz H	259	3.580
V	259	4.581
10.7GHz H	264	2.230
V	264	3.642
10.7GHz H	303	-2.663
V	303	2.846

10.7	H	V
Mean	2.732	2.791
Variance (Mean)	2.382	1.454
Variance (2.7)	2.382	1.355

Table 9-5
SMMR Simulator Calibration
21 GHz Wingover Calculations/Fall 1978 Mission

Channel	Day	Calculated T_B
21 GHz H	223	4.323
V	223	4.367
21 GHz H	254	6.550
V	254	4.934
21 GHz H	258	5.650
V	258	5.266
21 GHz H	259	3.996
V	259	3.152
21 GHz H	264	3.134
V	264	2.152
21 GHz H	298	-0.815
V	298	-0.803
21 GHz H	299	1.493
V	299	1.025
21 GHz H	301	-0.982
V	301	0.642
21 GHz H	303	0.395
V	303	0.298
21 GHz H	313	0.327
V	313	1.513
21 GHz H	322	4.274
V	322	3.961
21 GHz H	323	6.831
V	323	6.570

21.0	H	V
Mean	2.931	2.756
Variance (Mean)	2.665	2.199
Variance (2.7)	2.675	2.197

Table 9-6
SMMR Simulator Calibration
37GHz Wingover Calculations/Fall 1978 Mission

Channel	Day	Calculated T_B
37GHz H	192	2.558
V	192	2.269
37GHz H	223	-0.991
V	223	2.783
37GHz H	258	1.963
V	258	5.153
37GHz H	259	5.652
V	259	3.088
37GHz H	264	4.901
V	264	5.188
37GHz H	298	1.609
V	298	-0.659
37GHz H	299	3.422
V	299	1.144
37GHz H	301	-0.304
V	301	1.992
37GHz H	303	5.182
V	303	4.582

37.0	H	V
Mean	2.666	2.838
Variance (Mean)	2.227	1.830
Variance (2.7)	2.227	1.835

10.0 REFERENCES

1. D. H. Staelin, "Passive Remote Sensing at Microwave Wavelengths," *Proc. IEEE*, 57, 427-439, (1969).
2. K. Tomiyasu, "Remote Sensing of the Earth by Microwaves," *Proc. IEEE*, 62, 88-92, (1974).
3. T. Wilheit, W. Nordberg, J. Blinn, W. Campbell, A. Edgerton, "Aircraft Measurement of Microwave Emissions from Arctic Sea Ice," *Remote Sensing of Environment*, 129-139 (1972).
4. P. Gloersen, W. Nordberg, T. J. Schmugge, and T. Wilheit, "Microwave Signatures of First-Year and Multiyear Sea Ice," *J. Geophys. Res.*, 78, 3564-3572 (1973).
5. W. J. Campbell, P. Gloersen, W. Nordberg, and T. T. Wilheit, "Dynamics and Morphology of Beaufort Sea Ice Determined from Satellites, Aircraft, and Drifting Stations," pp. 311-327, *Cospar Approaches to Earth Survey Problems through Use of Space Techniques*, Editor P. Bock, (Akademie-Verlag-Berlin, 1974).
6. T. Schmugge, P. Gloersen, T. Wilheit, and F. Geiger, "Remote Sensing of Soil Moisture with Microwave Radiometers," *J. Geophys. Res.*, 79, 317-232, (1974).
7. T. J. Schmugge, T. T. Wilheit, P. Gloersen, M. F. Meyer, D. Frank, and I. Dirhirm, "Microwave Signatures of Snow and Fresh Water Ice," *Proc. of the Sym. on Advanced Concepts and Techniques on the Study of Snow and Ice Resources*, pp. 551-562, N.A.S., 1974, editor Henry S. Santeford.
8. W. J. Campbell, P. Gloersen, W. J. Webster, and T. T. Wilheit, "Beaufort Sea Ice Zones as Delineated by Microwave Imagery," to be published in *J. Geophys. Res.* 1976.
9. P. Gloersen, "Passive Microwave Images of Lake Ice," *NAS SP 331*, pp. 187-189 (1972).
10. P. Gloersen, T. J. Schmugge, and T. C. Chang, "Microwave Signatures of Snow, Ice, and Soil at Several Wavelengths," pp. 101-111, *Proc. of the URSI Commission II Specialists Meeting on*

Microwave Scattering and Emission from the Earth, E. Schanda, Editor, Berne, Switzerland, 1974.

11. A. E. Basharinov, S. T. Yegorov, A. S. Gurich, and A. M. Oboukhov, "Some Results of Microwave Sounding of the Atmosphere and Ocean from the Satellite Cosmos 243," *Space Research* XI, 394-600 (1971).
12. A. E. Basharinov, A. S. Gurvitch, A. K. Gorodezky, S. T. Egorov, B. G. Kutuza, A. A. Kurskaya, D. T. Matveev, A. P. Orlov, and A. M. Shutko, "Satellite Measurements of Microwave and Infrared Radio Brightness Temperature of the Earth's Cover and Clouds," *Proc. 8th Int. Symp. Rem. Sensing Environ.*, 291-296, U. Mich. (1972).
13. T. Wilheit, "The Electrically Scanning Microwave Radiometer (ESMR) Experiment," in: *The Nimbus-5 User's Guide*, pp. 59-105, NASA Goddard Space Flight Center, Greenbelt, MD (1972).
14. D. H. Staelin, A. H. Barrett, J. W. Waters, F. T. Barath, E. J. Johnston, P. W. Rosenkranz, N. E. Gaut, and W. B. Lenor, "Microwave Spectrometer on the Nimbus-5 Satellite: Meteorological and Geophysical Data," *Science*, 182, 1339-1341, (1973).
15. "Skylab Program: Earth Resources Experiment Package, Sensor Performance Report," Vol. 6 (S-19), MSC-05528, NASA Johnson Space Center, Houston (1974).
16. T. Wilheit, "The Electrically Scanning Microwave Radiometer (ESMR) Experiment," in the *Nimbus-6 User's Guide*, pp. 87-108, NASA/Goddard Space Flight Center, Greenbelt, MD (1975).
17. D. H. Staelin, A. H. Barrett, P. W. Rosenkranz, F. T. Barath, E. J. Johnston, J. W. Waters, and A. Wouters, "The Scanning Microwave Spectrometer (SCAMS) Experiment," in the *Nimbus-6 User's Guide*, pp. 59-86, NASA Goddard Space Flight Center, Greenbelt, MD (1975).
18. P. Gloersen, "Description of a Mechanically Scanned Microwave Radiometer for Use on Nimbus-G," NASA Goddard Space Flight Center (1973).

19. P. Gloersen, "Surface and Atmosphere Parameter Maps," NASA/Goddard Space Flight Center (1976).
20. J. W. Waters, et al., "The Shuttle Imaging Microwave System Experiment."
21. K. L. S. Gunn and T. U. R. East, "The Microwave Properties of Precipitation Particles," *Quart. J. Met. Soc.*, 80, 552-545, 1954.
22. M. Meeks, II and A. E. Lilley, "The Microwave Spectrum of Oxygen in the Earth's Atmosphere," *J. Geophys. Res.* 68, 1963.
23. D. A. Staelin, "Measurements and Interpretation of the Microwave Spectrum of the Terrestrial Atmosphere Near 1 Centimeter Wavelength," *J. Geophys. Res.*, 71, 2875-2881, 1966.
24. J. A. Lane and J. A. Saxton, "Dielectric Dispersion in Pure Polar Liquids at Very High Radio Frequencies," *Proc. Roy. Soc. London A*, 214, pp. 531-545, 1952.
25. International Critical Tables of Numerical Data, Physics, Chemistry and Technology, Vol. IV, McGraw Hill, NY 1928, pp. 231-239.
26. J. D. Jackson, "Classical Electrodynamics," John Wiley & Sons, Inc., New York, 1962, p. 216ff.
27. J. P. Hollinger, "Passive Microwave Measurements of Sea Surface Roughness," *Trans. IEEE Geoscience Electronics*, GE-9, pp. 165-169 (1971).
28. W. Nordberg, J. Conaway, D. B. Ross, and T. Wilheit, "Measurements of Microwave Emission from a Foam-Covered Wind Driven Sea," *J. Atmos. Sci.*, 28, 429-435, 1971.
29. T. Schmugge, P. Gloersen, and T. Wilheit, "Remote Sensing of Soil Moisture with Microwaves," NAS X-652-72-305.

30. A. T. Edgerton, F. Ruskey, D. Williams, A. Stogryn, G. Poe, D. Meeks, and O. Russell, "Microwave Emission Characteristics of Natural Materials and the Environment," Microwave Division, Aerojet General Corpor., ONR Contract NOOD 14-70C-0315, 1971.
31. T. Wilheit, W. Nordberg, J. Blinn, W. Campbell, and A. Edgerton, "Aircraft Measurements of Microwave Emission from Arctic Sea Ice," to be published in Remote Sensing of Environment.
32. C. Calhoon, "Performance and Operational Requirements for a X-Band Radiometer System," NASA/Goddard Space Flight Center, 1974.
33. C. Calhoon, "Performance and Operations Requirements for a K-Band Radiometer System," NASA/Goddard Space Flight Center, 1974.
34. J. Kirwan, "Operations and Service Manual, SS Part No. 311-X-1-001, X-Band Microwave Radiometer," Sense Systems Company, NASA Contract NAS 5-19929, 1976.
35. J. Kirwan, "Operations and Service Manual, SS Part No. 311-K-1-001, K-Band Microwave Radiometer," Sense Systems Company, NASA Contract NAS 5-19929, 1976.
36. C. D. Calhoon, Jr., "SMMR Simulator: A Multifrequency Microwave Radiometer System," National Aeronautics and Space Administration, Goddard Space Flight Center, X-953-76-283, 1976.
37. C. D. Calhoon, Jr. and B. M. Krupp, "SMMR Simulator Systems Calibration: Requirements and Procedures," _____, TM-79608, 1978.
38. B. M. Krupp and C. D. Calhoon, "Scanning Multi-channel Microwave Radiometer (SMMR) Simulator System Calibrations I: Derivation and Comparison of Calibration Formulations," Computer Sciences Corporation, CSC/TM-78/6213, 1978.
39. J. D. Kraus, Radio Astronomy, New York: McGraw Hill, 1964.

40. S. Chandrasekhar, Radiative Transfer, New York: Dover 1960.
41. B. M. Krupp and R. A. Neiman, "The Use of the Rayleigh-Jeans Approximation at Millimeter Wavelength," Computer Sciences Corporation, CSC/TM-78/6021, 1978.
42. C. D. Calhoon, M. Doyle, and S. Link, "SMMR Simulator Radiometer Equation Derivations," NASA/Goddard Space Flight Center, X-946-79-8, 1979.
43. S. Link, "Radiative Transfer Theory Applied to a Cascade of Ferrite Switch Junctions," Memorandum to the Record, 1979.
44. S. Link, "Background Information for SMMR Simulator Calibration Model Development—Radiative Transfer in a Lossy Element," Memorandum to the Record, 1979.
45. C. D. Calhoon, S. Link, M. Doyle, B. Krupp, "SMMR Simulator Radiative Transfer Calibration Model, I: Derivation," NASA-Goddard Spaceflight Center, TM-80244, August 1979.
46. Staff, Airborne Science Office, "Supplement, NASA CV-990 Airborne Laboratory Experimenters' Handbook," NASA-AMES Research Center, 1976.
47. C. D. Calhoon, "SMMR Simulator Systems Calibrations," Memorandum to Dr. P. Gloersen, August 1978.